THE OPTIMIZATION OF THE ZSM-5 CATALYST ACTIVITY WITH RESPECT TO CRYSTALLINITY

ANGEL TUMELO MODUTWANE BSc(Chem.Eng.)(University of Cape Town)

11 JULY 2005

Acknowledgements

I would like to express my gratitude to Prof. Eric van Steen, who supervised me during the first six months of this project, to Prof. Klaus Möller my supervisor and to all the technical staff whose help insured the successful completion of my experimental work.

My sincere gratitude to Mr Veli Msimang whose dedicated help ensured the completion of the setting up of the experimental rig and the proper running of the rig, for his help in using FORTRAN and gnuplot software and for his selfless efforts in helping out in both minor and major problems which contributed to the successful completion of this research project. My thanks to Dr. Silke and Mr Lucrecio Biquiza for proof reading my thesis, to Mr Itai Mabaso for his advise and help on different topics throughout my two years of study and to Mr Jako Niewoudt for his help in using ScientificWord.

I would also like to thank the NRF for funding me for this MSc degree and also thank the department for the funding that I received. To all my colleagues who helped me maintain the spirit of perseverance in my research.

Synopsis

In the synthesis of zeolites optimization of factors such as crystallinity, which encapsulates morphology, and acidity can result in optimal activity. Optimal activity is vital in chemical industries due to the fact that it results in higher yields, better selectivities and lower operational costs. In this project the effect of crystallinity on activity is investigated to get a better understanding of performance in terms of activity of amorphous, partially crystalline and highly crystalline materials using isomerisation of para-xylene as the probe reaction.

In literature, as shown by Triantafyllidis et al. [2001] and other researchers, an increase in crystallinity leads to the formation of crystals of well defined shape, smaller in size and possessing high surface areas. These characteristics are what result in the observed higher activity. Nicolaides [2002] has however come up with an observation contradictory to the general observation. He observed, in the aromatisation reaction of propane, that some optimum region is reached in activity with regard to crystallinity within the partially crystalline range. This was due to the presence of diffusion limitations in samples of high crystallinities resulting in a lower observed activity as compared to the intrinsic activity.

Hydrogels of the same compositions were subjected to different synthesis temperatures resulting in samples ranging from amorphous, partially crystalline to highly crystalline materials being formed. Synthesis temperatures were varied from 50 °C to 190 °C. The physical and chemical properties of these samples were studied using characterization techniques such as XRD, BET and SEM to study the crystallinity, porosities and surface structures respectively. Elemental analysis was carried out to ensure that the chemical compositions of all the samples were kept the same. This was done in order to ascertain that any difference in activity could only be accounted to by the difference in crystallinity. The synthesized samples were classified under three different categories: amorphous encompassed the 20 % crystallinity sample, partially crystalline encompassed the 50 and 66 % crystallinity samples and high crystallinity included the 71, 74 and 100 % crystallinity samples. *Para*-xylene isomerisation reaction was carried out in order to determine the activity and selectivity of the samples.

XRD results showed increasing crystallinity with an increase in synthesis temperature and BET results showed an increase in microporosity with an increase in synthesis temperature so that the sample synthesised at 50 °C with 20 % crystallinity had a micropore volume of 0.0056 cm^3/g whereas those synthesized at 190 °C with 100 % crystallinity had a higher micropore volume of 0.164 cm^3/g. SEM images showed a slight increase in crystal size from amorphous to partially crystalline and then a decrease to high crystallinity. The crystal sizes ranged from 0.2 to 1 μm. The amorphous materials were found to possess very low activities as reflected in conversions as low as 3.7 % at 300 °C. Conversion increased with the partially crystalline samples to around 30 % and the high crystalline samples achieved conversions as high as 60 %. In order to study the presence of any diffusion limitations which might be present in these structures

thereby affecting activity, the reaction kinetics were modelled using a simplified reaction-diffusion kinetic model. The results obtained from the models confirmed the objective of having activity only being affected by crystallinity. The absence of diffusion limitations was further illustrated by the same yields of *meta* and *ortho* xylene obtained for all catalysts at the same conversions. The reactor model fitted the data very well. The yield of all products was found to be independent of catalyst preparation and reaction temperature signifying the absence of diffusion limitaions. These results are further supported by the reactor model parameter estimation, which was independent of the magnitude of the diffusion contribution, signifying that the reaction rate cosntant only was necessary to fit the experimental data..

It was therefore concluded from these findings that the relationship between activity and crystallinity with regard to *para*-xylene isomerisation is such that activity increases with crystallinity and that the reaction for all crystallinities was reaction control limited.

Contents

List of Figures

List of Tables

Chapter 1

LITERATURE REVIEW

1.1 Introduction

The efficiency of zeolites as catalysts is related to their physical properties such as well-defined crystal geometry, high internal surface areas, uniform pores and chemical composition such as good thermal stability [Grieken et al., 2000]. One such type of zeolite is the ZSM-5. In industrial fluid catalytic cracking reactions, using a small amount of ZSM-5 as catalyst was found to raise the FCC gasoline research and motor octane numbers and light olefin yields [Chang et al., 1989].

Due to the zeolites importance in industrial usage, the optimization of the activity and selectivity of these catalysts is vital. A growing area of research is related to how crystallinity affects activity and if optimization of crystallinity can lead to better catalyst performance in terms of higher conversions and specific selectivities [Nicolaides, 1999].

The percentage crystallinity is determined by the physical and chemical properties of the catalyst. Physical properties include the morphology which includes crystal size, shape and porosity while the chemical property includes the silicon to aluminum (Si/Al) ratio. The crystallinity of a zeolite can be altered during the synthesis stages by changing synthesis factors such as temperature, time and the chemical composition of the synthesis mixture [Triantafyllidis et al., 2001]. These factors will be discussed in the crystallization process section, resulting in catalyst ranging from amorphous, partially crystalline to high crystallinities.

Previous characterization studies have shown catalysts of high crystallinities to be smaller in size, to have a higher number of micropores, higher surface areas and better defined crystal shapes Guisnet and Magnoux [1989]. The high surface areas lead to an increase in the number of acid sites exposed to the reaction medium and defined crystal shapes decreased resistance to diffusion of reactants to active sites. These are the reasons behind the generally observed increase in activity with an increase in crystallinity.

Nicolaides [1999] has, however, come up with a contradictory observation. When studying the isomerization reaction of linear butene to iso-butene, it was found that partially crystalline samples resulted in higher activities and selectivities than the highly crystalline samples [Nicolaides, 1999].

This project further investigates the effect of crystallinity on activity. This will be done by changing only one factor, synthesis temperature, which will result in samples of ZSM-5 of different physical properties being obtained. The samples will have similar chemical properties. The physical properties will then be characterized by using techniques such as nitrogen adsorption at 77 K to analyze porosity, SEM

(Scanning Electron Microscopy) to analyze crystal shape, size and structure. XRD (X-ray diffraction) will be done to determine percentage crystallinity and *para*-xylene isomerization reactions to look at activity. A reaction-diffusion model will be used to quantify activity and diffusion properties of the prepared samples.

1.2 ZSM-5 properties

ZSM-5 catalysts possess catalytically active sites and uniformly sized and shaped micropores, which allow for their use as shape selective catalysts [Trong et al., 2000]. ZSM-5 has a high mechanical strength, chemical and thermal stability and can be used over a wide range of operating conditions [Flanders et al., 2000].

1.2.1 Physical properties

The unique catalytic performance of the ZSM-5 is attributed to the two-dimensional system of pore channels, straight and sinusoidal channels, intersecting at right angles, which makes it 3-dimensional [Triantafyllidis et al., 2001].

Figure 1.1 shows an overview of the ZSM-5 structure. Structure (b) shows the pore diameter of the straight channels which are much larger in size than those of the sinusoidal channels and structure (c) shows how the channels intersect each other at right angles.

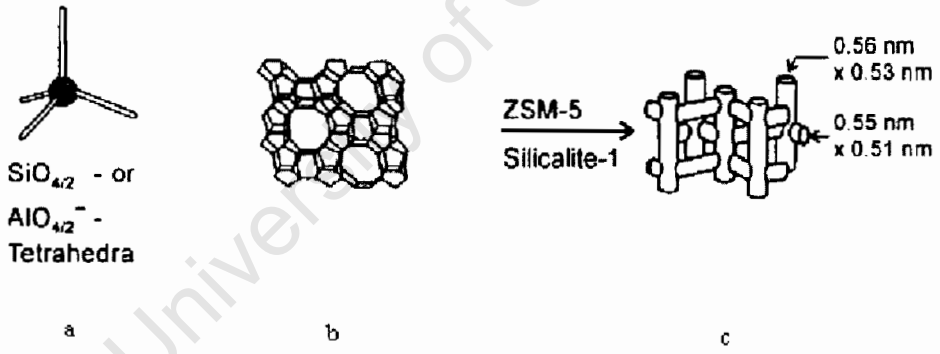

Figure 1.1: Different pore sizes found in the ZSM-5 [Triantafyllidis et al., 2001]

The straight channels are 5.3 x 5.6 Å in size while the sinusoidal channels (zig-zag) are 5.1 x 5.5 $\AA$ [Flanders et al., 2000]. These channels form three different possible adsorption sites for adsorbate molecules [Flanders et al., 2000].

Micropores are formed by intra void areas found within one crystal while meso and macropores are the intercrystal void areas formed through the agglomeration of many crystallites or due to the formation of amorphous material.

Micropores have pore diameters in the range less than 20 $\AA$. Mesopores diameters lie between 20 and 500 $\AA$. Pores of sizes above 500 $\AA$ are classified as macropores [Flanders et al., 2000]. The bigger the crystal sizes are, the larger this inter-crystal void volume will be resulting in larger crystals possessing higher meso/macropore volumes.

1.2.2 Chemical properties

1.2.2.1 Acid sites

The ZSM-5 catalyst is made up of a framework of $[SiO_{4/2}]$ and $[AlO_{4/2}]^-$. Figure 1.1(a) shows how the alumina and silica atoms are coordinated within the structure with the black atom representing the oxygen atom being used as a linkage between the Al and Si atoms [Trong et al., 2000]. The tetrahedrally coordinated aluminium is known as FAL (Framework Aluminum). The general molecular formula of ZSM-5 is $\frac{m}{y}(M^{y+})_{m/y}\,(\mathrm{Si}\,O_2)_n\,(AlO_2)^-_m \cdot H_2O$ where M^{y+} is the cation used. Due to an imbalance of charges the framework is polar, the cation is required to neutralize this polarity. Active sites sometimes referred to as acid sites, are formed through the protonation of the structure. This occurs during ion exchange where the cation is exchanged for an ammonium ion and calcined to drive off ammonia making the structure acidic. In order to keep the number of acid sites the same, the same composition in the synthesis mixture should be used during the synthesis stages. Acid sites occur either as Brϕnsted or as Lewis acid sites.

- **Brϕnsted acid sites** are the sites formed when the framework is protonated. The hydrogen ion, which is partially positively charged as shown in Figure 1.2(a), can now be used to protonate electron rich centers.
- **Lewis acid sites** are formed when the catalyst, in its Brϕnsted form, is calcined at high temperatures. The structure is dehydrated and alumina atoms are extracted from the framework to become octahedrally coordinated to the oxygen atom resulting in a net positively charged atom as shown in Figure 1.2(b). This EFAL (Extra Framework Aluminum) which acts as an electron acceptor and is known as a lewis acid. If the EFAL is not removed from within the structure it can result in pore blockage and inhibition of reactants to active sites [Triantafyllidis et al., 2001]. It is usually removed through post-synthesis treatment such as leaching which will be discussed in the post-synthesis treatment section.

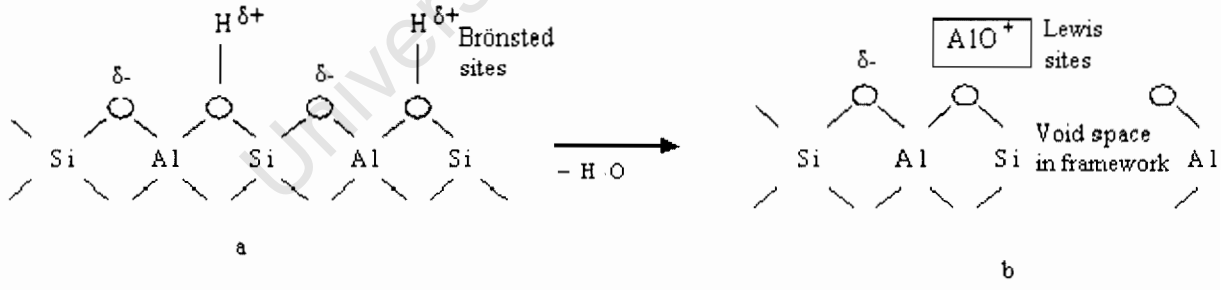

Figure 1.2: Brönsted (a) and Lewis (b) acid sites

1.2.2.2 Strong and weak acid sites

Strong acid sites as observed by Costas were those formed by the FAL (Brϕnsted) while the weak acid sites were formed by EFAL (Lewis) species [Triantafyllidis et al., 2001].

Temperature programmed desorption of ammonia is the most commonly used method to determine the acidic strength of active sites. The NH_3 vs temperature profile characterizes the acid sites of the

zeolite with respect to both quantity and strength. Low temperature desorption of NH_3 occurred at temperatures between 150 and 300 °C and this quantified the number of weak acid sites while high temperature desorption occurred at temperatures above 350 °C to 700 °C quantifying the number of strong acid sites [Triantafyllidis et al., 2001].

Nicolaides [2002] used ammonia adsorption microcalorimetry method to quantify the number of strong Brϕnsted acid sites found in structures of different crystallinities. Heat evoluted during the adsorption of NH_3 was used to classify the strength of the acid sites. Strong acid sites were those with heat of adsorption ranging from 120 to 140 kJ/mol. Heats of adsorption below this represented the weak acid sites [Nicolaides, 2002].

Figure 1.3 shows the number of strong Brϕnsted acid sites found on a ZSM-5 catalyst as a function of XRD crystallinity, with a Si:Al (silica to alumina ratio) of 35 [Nicolaides, 1999]. These results show an increase in the number of strong acid sites with an increase in crystallinity. The trend observed in this work was supported by that of Triantafyllidis et al. [2001]. This trend suggest that increasing crystallinity increases the number of aluminium atoms incorporated into the framework as compared to the non-incorporated EFAL since as explained above these are the sites which form the strong acid sites. This phenomena is better clarified in the mechanism of crystallization process section.

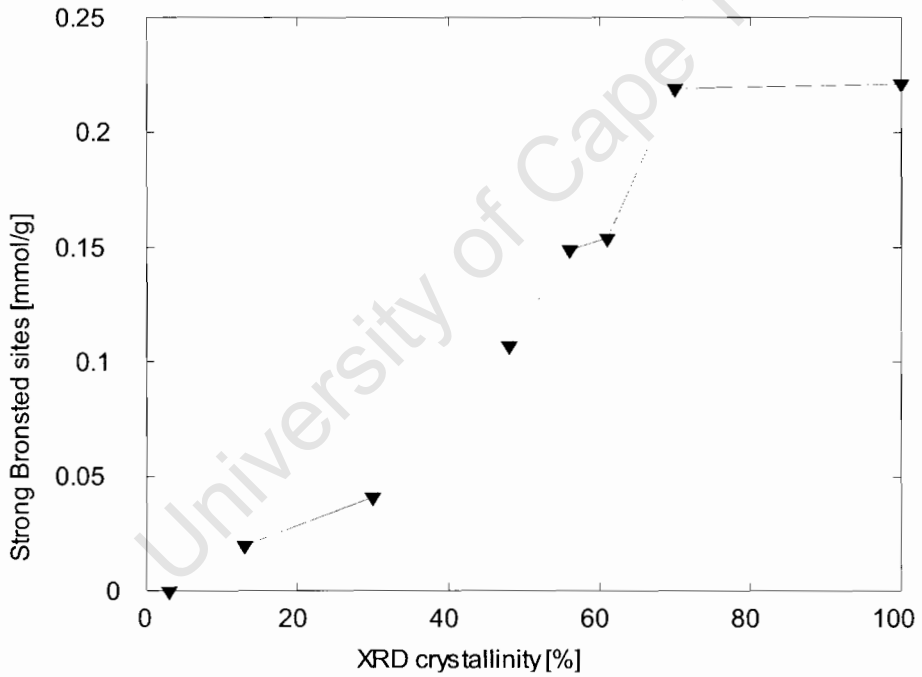

Figure 1.3: Number of strong Brönsted sites vs XRD crystallinity [Nicolaides et al., 2002]

1.3 Mechanism of crystallization

The morphology (crystal size, crystal shape and porosity) and chemical properties of a MFI-type zeolite structure can be changed during the crystallization process by altering factors such as Si/Al, aluminium content, nature of cations present in the synthesis medium, water content, alkalinity of the synthesis medium and the temperature of the crystallization process [Grieken et al., 2000]. Grieken et al. [2000]

observed that an increase in the SiO_2/Al_2O_3 and OH/SiO_2 molar ratios as well as a decrease in the H_2O/SiO_2 molar ratio in the synthesis solution lead to a decrease in the final crystal size. Bulky cationic templates were found to narrow the pore sizes of meso and macroporous zeolites [Grieken et al., 2000]. In order to study the effect of one factor on the resulting morphology, other factors should be kept constant and only that one factor varied. In this study the varied factor was the synthesis temperature.

Three major steps are found to control the mechanism of crystallization:

STEP 1: The starting supersaturated gel is converted into a particulate material, this results in the formation of amorphous primary particles with sizes around 8-10nm [Grieken et al., 2000]. This induction period varies in time depending on the synthesis temperature. These particles agglomerate and form particles large in size, non-porous and with irregular geometry.

STEP 2: The primary particulate materials then undergo an aggregation process known as nucleation and crystallization, which leads to the formation of larger units (secondary particles). It is during this step that the first signs of crystallinity starts to be detected. As the crystallization progresses, these secondary particles grow gradually by packing and linking of additional primary units [Grieken et al., 2000].

STEP 3: The transformation of the secondary particles into nanocrystalline ZSM-5 crystals through a zeolitization process occurs in this step [Grieken et al., 2000]. This process is simply a solid-solid transformation which involves the reorganization of the solid materials yielding crystalline zeolite.

1.3.1 Effect of temperature

Temperature is known to affect the crystallization process [Grieken et al., 2000]. At higher temperatures, less time is required to complete the three steps governing the crystallization process. This again results in structures synthesized at high temperatures being more crystalline than those synthesized at lower temperatures. When compared at the same synthesis period of 50 hours, Grieken et al. [2000] observed that the final product obtained at synthesis temperatures as low as 50 °C resulted in structures with the same characteristics as the product obtained from step 1 of the crystallization process [Grieken et al., 2000]. The only form of porosity observed was in the form of mesopores formed by the interparticle voids through agglomeration of these particles. At higher temperatures ranging from 100 to 120 °C smaller crystals could be observed from the resulting product material with a few lump amorphous material present. These materials had same characteristics as products from step 2 and were partially crystalline. At high synthesis temperatures the resulting crystals were very small and microporous and highly crystalline. No amorphous material was observed. These materials signified the completion of the crystallization process and possessed high crystallinities.

This concept of increasing crystallinity with increasing temperature was further illustrated by Nicolaides [1999] as shown in Figure 1.4. At very low synthesis temperatures, crystallinity is not detected by the XRD technique.

1.3.2 Acid sites formation

During the initial stages a material rich in silica is formed with an abundance of EFAL species. Aluminium is gradually incorporated into the structure as the crystallization process proceeds [Grieken et al., 2000]. This means that samples resulting from primary products of the crystallization products, which are classified as amorphous, have most of the aluminum atoms as a form of EFAL while those which have undergone the secondary and tertiary stages have most of the aluminum in the form of FAL. This

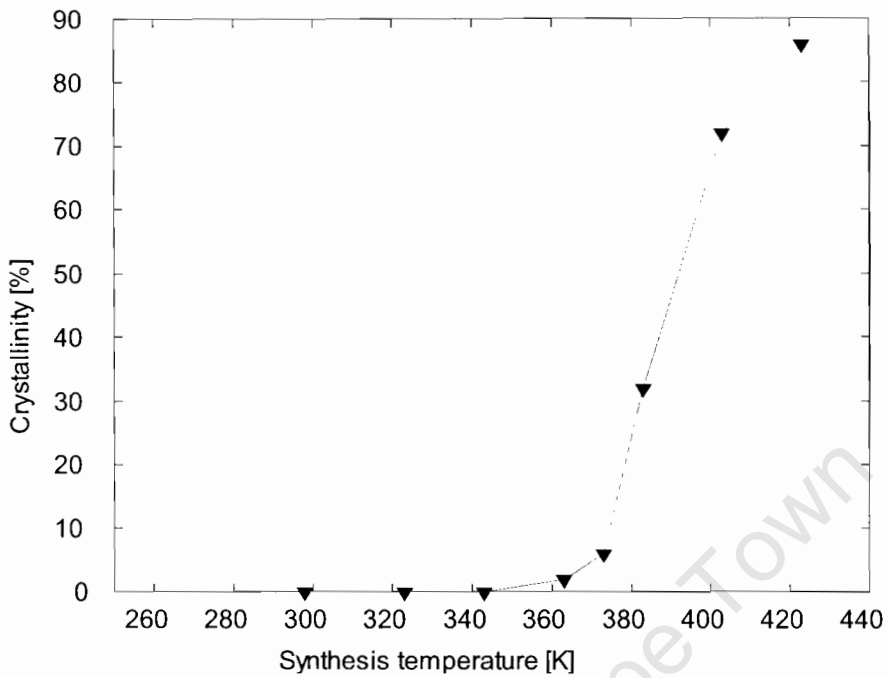

Figure 1.4: XRD vs synthesis temperature at a synthesis time of 72 hours [Nicolaides, 1999].

further illustrates why materials with high crystallinities will possess higher numbers of strong acid sites as compared to the lower crystallinities and amorphous materials.

1.4 Techniques used to characterize porous materials

1.4.1 XRD analysis

X-ray diffraction (XRD) is the most commonly used method to determine the % crystallinity of crystalline structures. This method compares the intensity of the peaks obtained by X-ray diffraction with respect to a reference crystalline structure of high crystallinity. The reference material used being a highly crystalline silicalite sample [Nicolaides, 1999]. The % crystallinity is then obtained by equation 1.1 [Nicolaides, 1999]:

$$\%\ \text{XRD crystallinity} = \frac{\text{Sum of peak intensities of sample}}{\text{Sum of peak intensities of reference}} \cdot 100 \tag{1.1}$$

Structures of very high crystallinities are usually identified by the sharp peak intensities obtained from XRD analysis and a decrease in the peak intensity represents a decrease in the % crystallinity as shown by Figure 1.5

Substantially amorphous materials have XRD crystallinities lower than 30 %, partially crystalline samples are those possessing 30-70 % crystallinity and highly crystalline materials are those with >70 % XRD crystallinity [Nicolaides, 2002]. XRD analysis has been known to fail when dealing with very small

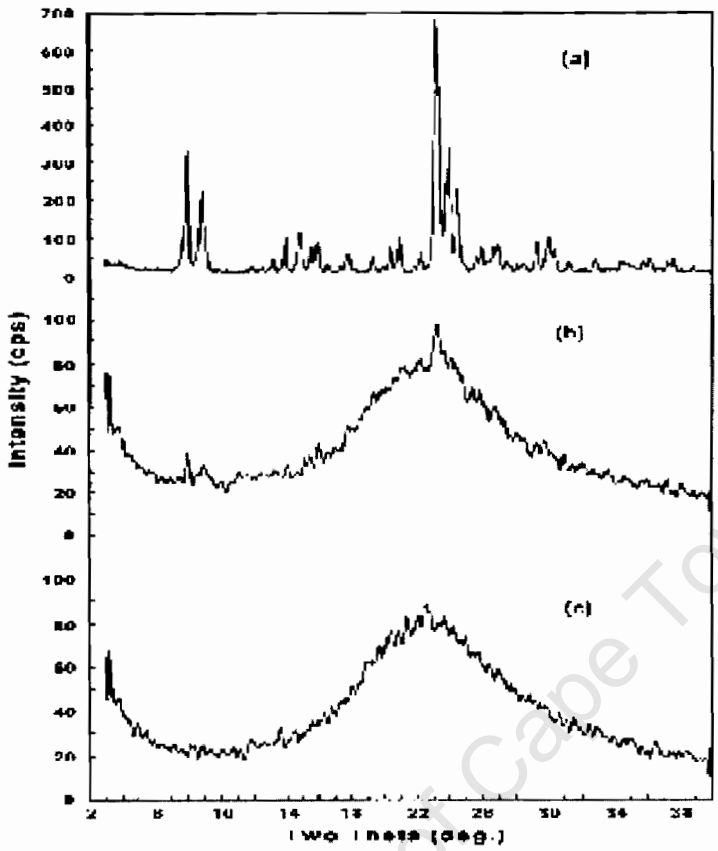

Figure 1.5: XRD spectrum for an amorphous (c), a low crystallinity material (b) and highly crystalline (a) material [Nicolaides, 1999].

crystallites if the size is below the X-ray detection limit [Dejaifve et al., 1981]. It was calculated using the Scherrer formula that in order to observe an X-ray diffraction peak, crystal sizes larger than 8 nm are needed.

1.4.2 Nitrogen adsorption at 77 K

Nitrogen adsorption is used to characterize porosities. Properties such as the total surface area (micro, meso and macropore area), the distribution of micro and mesopores, the micropore volume and total pore volume can be obtained by analyzing the adsorption isotherm.

A typical isotherm for an idealized microporous material is shown in Figure 1.6(a). This isotherm is found to occur in catalysts possessing a high degree of crystallinity and therefore an abundance of micropores. Micropores, which have a higher surface area and therefore a higher adsorption capacity for the N_2 molecules, make up most of the total surface area. At low pressures, a rapid increase is observed in the isotherm which is due to adsorption taking place inside the micropores. Once these micropores are filled most of the adsorption sites are filled and negligible adsorption occurs thereafter.

For the partially crystalline materials, which have approximately same numbers of meso and micropores, the typical observed isotherm is illustrated in Figure 1.6(b). At low pressures, where adsorption occurs

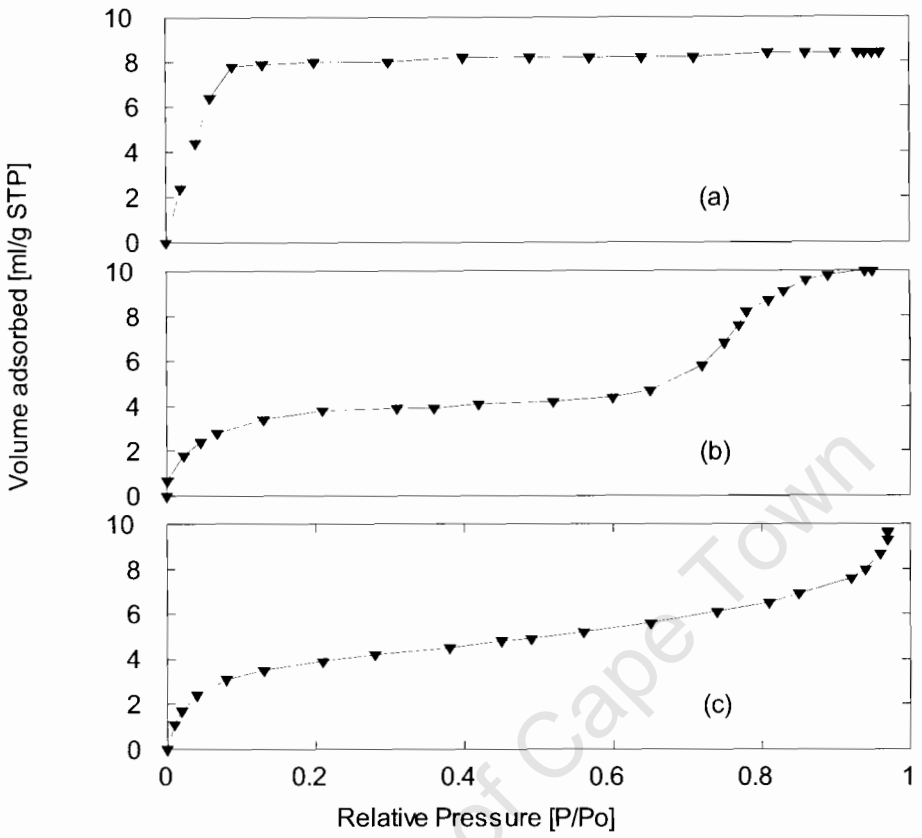

Figure 1.6: Schematic nitrogen isotherms at 77 K for (a) micro, (b) meso/macro and (c) nonporous material

predominantly in the micropores, some adsorption takes place as illustrated by the initial increase in the slope. At higher pressures , where mesopore filling occurs, the slope of the curve increase again due to adsorption taking place inside the available mesopores until the point of saturation is reached.

Triantafyllidis et al. [2001] found a reference sample of 100 % XRD crystallinity to have a micropore area as high as 347 m^2g^{-1}, mesopore area as little as 40 m^2g^{-1} and micropore volume of 0.194 cm^3g^{-1}. For a sample of 80 % XRD crystallinity, which is still highly crystalline, the micropore area decreased to 285 m^2g^{-1}, micropore volume to 0.135 cm^3g^{-1} and mesopore area increased to 89 m^2g^{-1}[Triantafyllidis et al., 2001].

For non-porous materials the amount of adsorption taking place at low pressures is insignificant as compared to that at high pressures as observed from Figure 1.6(c) from the different slope increases. Adsorption takes place inside the mesopores formed in between the agglomerated particles. The same isotherm was observed by Grieken et al. [2000] when BET (Brunauer Emmett Teller) analysis on an amorphous material was carried out. It was shown that the total pore volume at a relative pressure of 0.99 to be equal 1 cm^3/g with the micropore volume being only 0.10 cm^3/g [Grieken et al., 2000].

1.5 Preparation methods for catalysts with variable crystallinity

Samples of different crystallinities can be obtained by changing various factors during the synthesis stage or by carrying out post-synthesis treatments on the final products. Factors which can be altered during the synthesis stages are temperature, which was discussed under the mechanism of crystallization section, synthesis time and composition of synthesis mixture while post-synthesis treatment can be hydrothermal or acid/chemical treatment.

1.5.1 In-situ synthesis factors

Synthesis time also plays an important role in the crystallinity of the final structure obtained. If temperature is kept constant, increasing synthesis time allows the crystallization process to proceed further and long synthesis times result in the completion of the crystallization process. Not all synthesis mixtures lead to the formation of crystals. Depending on the temperature it can take 3 months to get crystalline material. Alternatively if left for too long the crystals collapse again and form a new phase [Nicolaides et al., 2001]. Altering the composition of the mixture, resulting in a change in the Si/Al ratio also alters the degree of crystallinity. The Löwensteins rule states that the Si/Al is always greater than unity. The structure will shift itself in such a way that such a rule is obeyed, so depending on the amount of aluminum available for bonding different bonding configurations will result. This changes the geometry of the structure which in turn affects crystallinity.

1.5.2 Post-synthesis factors

1.5.2.1 Hydrothermal treatment

Hydrothermal steaming changes the crystallinity by changing the Si/Al ratio and therefore the acidity of the structure. It is basically the extraction of Al atoms from the framework which results in vacant sites within the framework [Masuda et al., 1998]. This process is better known as dealumination. Under conditions of high temperature steaming, where this extraction occurs, aluminum atoms slip out of the zeolite framework resulting in a structure which is rich in Si atoms. The amount of extracted aluminum will increase with an increase in the severity of the steaming conditions.

The extracted aluminum can either be pushed out of the zeolite framework as an EFAL atoms or remain inside [Masuda et al., 1998]. Severe steaming can lead to the extraction of too many aluminum atoms, resulting in too many vacancies being formed leading to the collapse of the structure.

Crystallinity was found to decrease slightly but progressively upon steaming resulting in dealuminated samples being less crystalline than their corresponding parent materials [Gola et al., 2000]. The decrease was further enhanced by increasing temperature, pressure and steaming times [Montes et al., 1998]. This decrease is due to the destruction of the structure as a result of the vacancies left by the aluminium causing distortion and eventually a partial collapse.

1.5.2.2 Leaching

Leaching is a process where a mineral acid is introduced into the structure removing the alumina atoms present inside the framework but not incorporated into the framework itself. This means that after hydrothermal treatment, leaching can be carried out to remove the EFAL from inside the zeolite framework.

Commonly known leaching agents are ammonium hexafluorosilicate (AHFS), ethylenediaminetetraacetic acid (EDTA) and ammonia [Triantafyllidis et al., 2001]. This method results in samples free of EFAL which were found to be more crystalline than the untreated samples. Using a very strong acid can result in the same process as hydrothermal steaming. Aluminum atoms can be extracted from the framework. The main advantage of using AHFS is that it is a mild acid and produces samples almost free of EFAL (Extra Framework Aluminium) species, and this could be beneficial in avoiding pore blockage by the EFAL species located inside the channels [Triantafyllidis et al., 2001]. Treatment with a low concentration of AHFS was found to increase the crystallinity of the sample due to removal of amorphous EFAL species. An increase in crystallinity was observed from 83% with reference to the untreated sample to 89 % after treatment with a 0.64 M concentration of AHFS (concentration is expressed in terms of molar ratio of $(NH_4)_2SiF_5$ introduced in solution to Al atoms in the volume of zeolite treated) [Gola et al., 2000]. With an increase in concentration of up to 1 M the crystallinity decreased to 68 % [Gola et al., 2000].

1.6 Factors influencing activity and selectivity

1.6.1 Crystallinity

It was observed during ongoing studies that materials need to have a XRD crystallinity level of 30 % and higher in order to possess any significant catalytic activity [Nicolaides et al., 2001]. The catalytic behavior of zeolites for various acid catalyzed reactions depend on the degree of crystallinity [Nicolaides et al., 2001]. Nicolaides [1999] investigated the effect of crystallinity on the skeletal isomerization of linear butenes. Crystallinity was varied by using different synthesis temperatures. The resulting samples ranged from 2 % crystallinity to the reference structure, which was ZSM-5, at 86 % crystallinity. Conversion, selectivity and yield to isobutene were compared for these different crystalline structures. It was found that conversion increased with an increase in crystallinity until a maximum was reached and started decreasing again while selectivity decreased.

The yield during propane aromatization was high for partially crystalline structures and extremely low with amorphous structures as shown in Figure 1.7 [Nicolaides et al., 2001]. This observation was due to the hypothesis that diffusion constraints results in a fall in activity as crystal sizes increase in the range 0.045-4.5 μm Nicolaides et al. [2002]. From these results it was concluded that partially crystalline structures can enhance selectivity and activity for zeolite structures. The generally observed trend is that an increase in crystallinity results in an increase in conversion. This observed increase was due to the high surface areas, more numbers of strong acid sites and easy access to acid sites properties found in structures of high crystallinities.

Since porosities change with a change in crystallinity as shown in the nitrogen adsorption section, selectivity is also affected as the structure becomes more crystalline. Highly crystalline structures, rich in micropores seem to possess good shape selectivity properties and the formation of smaller molecules is preferred over that of the bulky molecules.

The activity of a catalyst is directly affected by the number of strong acid sites present in the sample. Figure 1.8 clearly illustrates the concept of how acidic properties and conversion are related. High crystallinity materials which are characterized by an abundance of strong brϕnsted sites show enhanced catalytic activity as illustrated by the increase in conversion for n-hexane cracking.

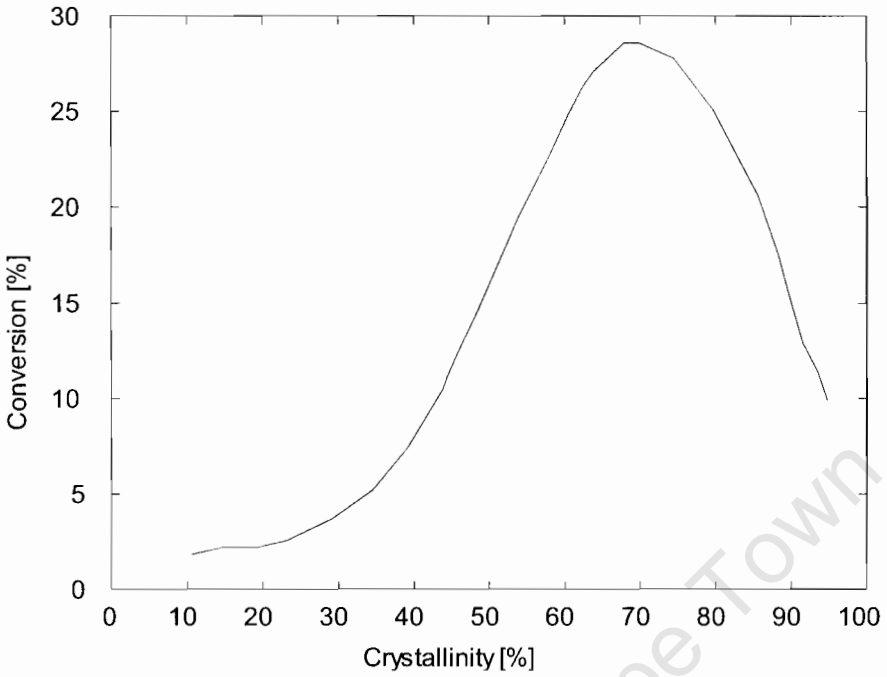

Figure 1.7: Conversion vs crystallinity for the aromatization of propane on ZSM-5 [Nicolaides et al., 2002]

1.6.2 Coking

Catalytic activity and shape selectivity is also affected by coking and deactivation. Coking leads to a progressive decrease in the activity due to the combination of site coverage and pore blocking effects. Shape selectivity will vary due to intimate changes in effective pore openings, cages dimensions, etc [Dejaifve et al., 1981]. Coking can occur in three different ways: limitation of access of reactant molecules to the reactive sites, blockage of access to the sites of the cavities and blockage of access to the sites of the pores [Guisnet and Magnoux, 1989]. The deactivating effect of coke is more pronounced when deactivation is due to pore blockage than when it is due to site coverage. Coking is a process whereby heavy by-products form a deposit on the surface and provoke deactivation. The coking tendency is an intrinsic property of the zeolite pore structure: the smaller the pore size the lower the coke yield in hydrocarbon cracking processes [Guisnet and Magnoux, 1989].

Because of the microporous nature of the ZSM-5, bulky polyalkylaromatics are not easily formed rendering this catalyst highly resistant to coking [Dejaifve et al., 1981]. Deposition can only occur on its external surface [Dejaifve et al., 1981]. Since the strongest acidic sites are situated inside the intracrystalline volume of the catalyst deactivation due to coking is less pronounced [Dejaifve et al., 1981]. The rate of coking can further be reduced by decreasing the external surface area or by decreasing external surface acidity, for instance, by decreasing drastically the aluminum content in the last stage of crystallization [Dejaifve et al., 1981].

1.6.3 Diffusion

Zeolite intracrystalline diffusivity is influenced by a number of physiochemical factors such as:

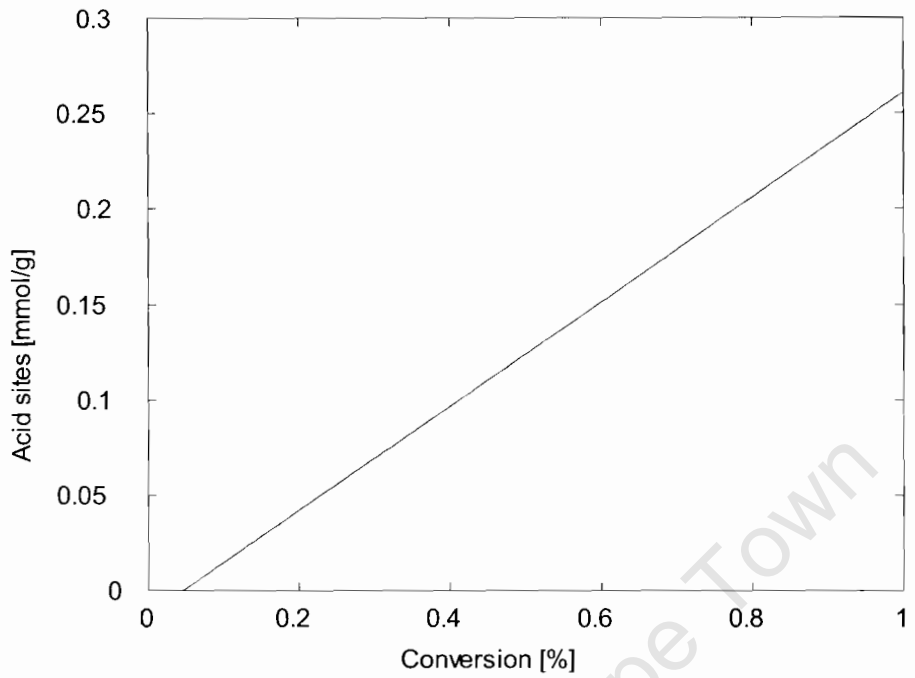

Figure 1.8: Number of brönsted acid sites vs conversion for n-hexane cracking [Nicolaides et al., 2002].

- Size, shape and polarity of the diffusing molecules
- Zeolite channel geometry, connectivity and dimensions
- Chemical composition of framework, e.g., Si/Al ratio
- Cation type, size, distribution, charge and concentration
- Lattice defects
- Zeolite morphology

The concept of how diffusion limitations take place within a porous structure was discussed by Masuda et al. [1998]. Diffusion limitations are caused by restriction of molecules within the pores and also by strongly adsorbing molecules holding onto the active sites and preventing the diffusion of other molecules. Therefore the smaller the porous system the more inhibited the freedom of movement is. As the size of the diffusing molecule approaches that of the zeolite channels, the interaction energy becomes increasingly important and the rate of diffusion is slowed down.

The diffusivity can be coupled with the catalysts activity by defining the Thiele modulus (equation 1.2):

$$\phi = \sqrt{\frac{k}{(\frac{D}{R^2})}} \tag{1.2}$$

which is a ratio of the intrinsic first order rate constant (k) to the diffusion time constant (D/R^2). As the diffusivity decreases the Thiele modulus increases. The effectiveness factor as shown by equation 1.3:

$$\eta = \frac{\text{Diffusion limited reaction rate}}{\text{Intrinsic reaction rate}} = \frac{\int r \, dV}{r_s V} \tag{1.3}$$

Table 1.1: Diffusion coefficients for MFI measured under non-reactive conditions [Karger and Ruthven, 1992]

Sorbate	Sorbent	R [μm]	D_e at 298 K [m^2s^{-1}]	E_a [kJ/mol]
p-xylene	Silicalite	1.0	$1{\cdot}10^{-15}$	15
m-xylene	Silicalite	1.0	$4{\cdot}10^{-16}$	-
o-xylene	Silicalite	1.0	$2{\cdot}10^{-16}$	-
p-xylene	H-ZSM5	0.5	$1{\cdot}10^{-20}$	66.5
o-xylene	H-ZSM5	0.5	$1{\cdot}10^{-16}$	-

depends on the Thiele modulus according to Figure 1.9. For spherical geometry diffusion limitations become magnified when $\phi > 1$. The Thiele modulus in equation 1.2 is exact only for irreversible 1st order reactions (Figure 1.9). These can be extended easily to any type of single reaction by deriving the equation from first principles (steady state mass balance) using that specific reaction order. However, for multiple reactions only equation 1.3 remains applicable. Karger and Ruthven [1992] show the applicability of the first order Thiele modulus to experimental data. Diffusional limitations were found to be favoured by large particles, a high rate constant and a low effective diffusivity while reaction control is favoured by the smaller particles, low reaction rate constant and high effective diffusivity [Karger and Ruthven, 1992]. Table 1.1 shows the diffusion constants for xylene isomers at different particle radius.

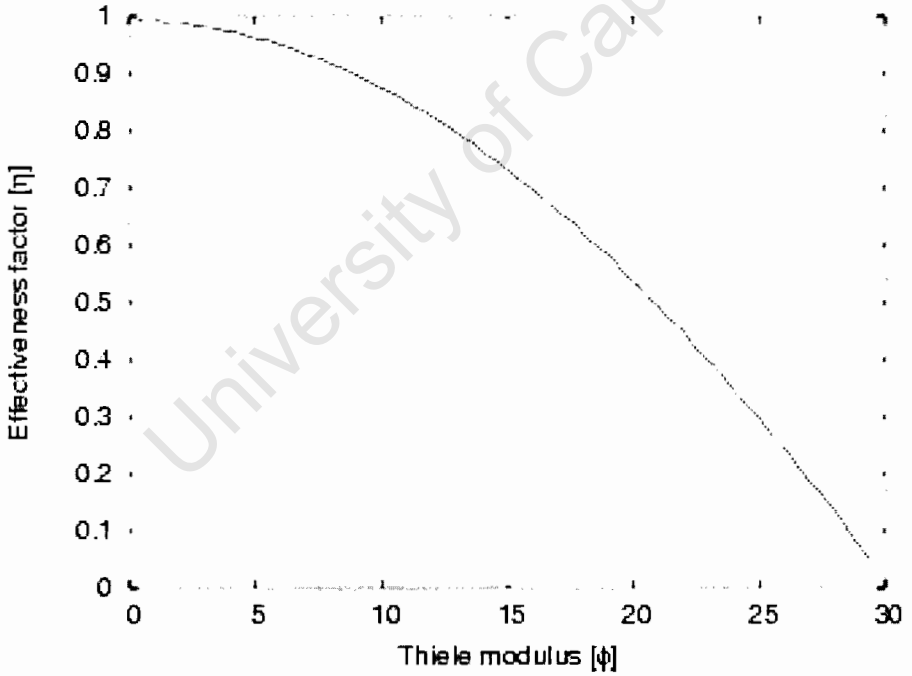

Figure 1.9: Effectivenes factor vs Thiele modulus for spherical geometry and first order irreversible reaction

1.7 Para-xylene isomerization

1.7.1 Shape selectivity in zeolite reactions

Zeolite structures make excellent catalysts in processes where selectivity of one product is vital over that of the other. This concept is known as shape selectivity. Alkyl aromatics such as the xylene isomers are a class of reactants and products that have molecular sizes similar to the dimensions of the ZSM-5. These molecules thus display unique shape selective properties. Shape selective reactions can be classified as three types:

Type 1 REACTANT SELECTIVITY: Reactant selectivity allows only those molecules to react inside the zeolite, which are small enough to diffuse into the structure. Large molecules are left unreacted because they are hindered from reaching the active sites.

Type 2 PRODUCT SELECTIVITY: Product selectivity on the other hand occurs when some of the products are too bulky to diffuse out. These bulky molecules usually undergo secondary reactions to form smaller molecules in order to exit. If they do not leave, 'fouling' of the zeolite may occur resulting in deactivation.

Type 3 TRANSITION STATE SELECTIVITY: The cavities inside the zeolite are too small thereby preventing the transformation of molecules via bulky transition states of a reaction. Whereas the reactant and product molecules are small enough to diffuse through the channels, the intermediate molecules are spatially constrained either by their size or orientation.

The determining factor in shape selective reactions is the diameter of the reacting material in relation to that of the pore mouth of the zeolite material. Isomerization of xylene is an extensively investigated shape selective catalytic process [Sponer et al., 2001]. The difference in the diameters of the xylene isomers make it possible to shift selectivity, depending on the catalyst used and the pore diameter of that particular catalyst, to whichever product distribution is desired.

1.7.2 Reaction mechanism

This reaction proceeds via two ways, intra and intermolecular mechanisms:

Type 1 INTERMOLECULAR: As shown in figure 1.10, the intermolecular pathway involves successive xylene disproportionation (A) followed by transalkylation between the trimethylbenzene and reactant xylene molecules (B), resulting in a yield of trimethylbenzenes, tetramethylbenzenes and toluene [Guisnet et al., 2000].

Type 2 INTRAMOLECULAR: The intramolecular mechanism proceeds via a unimolecular 1,2-methyl shift in benzenium-ion intermediates resulting in a yield of xylene isomers as shown by figure 1.11.

Under conditions where the reaction proceeds via the intramolecular pathway the consecutive scheme is given by:

$$para\ xylene \leftrightarrows meta\ xylene \leftrightarrows ortho\ xylene \tag{1.4}$$

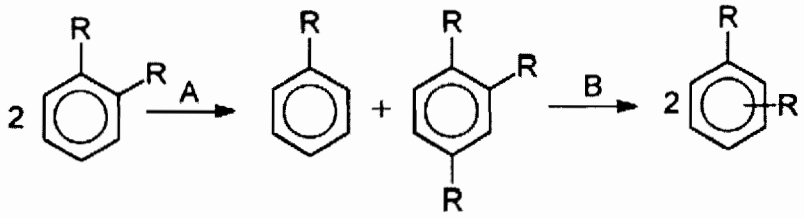

Figure 1.10: Intermolecular mechanism [Guisnet et al., 2000]

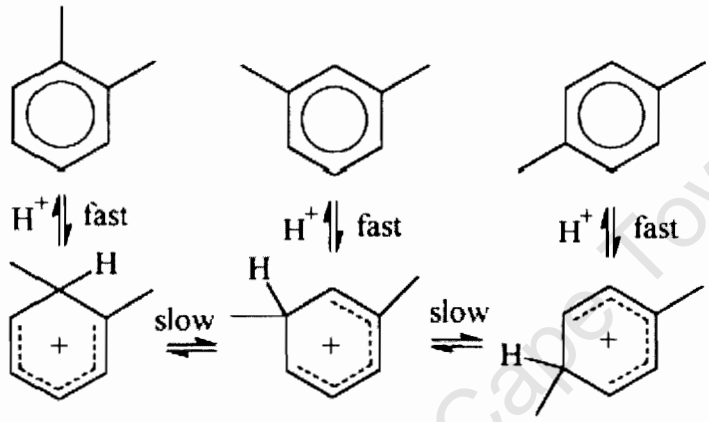

Figure 1.11: Intramolecular mechanism [Guisnet et al., 2000]

Selectivity with regard to the dominant mechanism is controlled by the zeolite architecture, void space volume, acid sites and reaction temperature [Sponer et al., 2001]. When steric constraints exerted by the pore walls in the vicinity of the acid sites inhibit (medium-pore size zeolites) or limit (large-pore zeolites) the formation of the bulky diphenylmethane intermediates of transalkylation, xylene isomerization only occurs through the intramolecular mechanism [Guisnet et al., 2000]. This is a direct result of the size of the intracrystalline zeolite cavity . The smaller the channels are, the more the reaction goes in favour of a less bulky product distribution found through intramolecular isomerization [Guisnet et al., 2000]. Previous studies have shown that the selectivity towards the disproportion reaction over zeolites with 10-membered ring apertures is very low, whereas zeolites with 12-membered rings exhibit higher selectivities towards disproportionation products. The uniqueness of ZSM-5 in the isomerization reaction of *para*-xylene lies in its ability to inhibit the formation of these undesirable by-products such as toluene and trimethylbenzenes, which are formed through the bimolecular disproportionation reaction [Chen et al., 1994]. These bulky molecules are sterically hindered by the small pore openings of the ZSM-5 and are therefore not formed as products.

The contribution of the intermolecular mechanism decreases with increasing temperature [Guisnet et al., 2000]. Studies carried out on a silica-alumina catalyst showed that above 300 °C isomerization was found to be essentially intramolecular, whereas below 200 °C the inter-molecular process predominated [Guisnet et al., 2000]. At low temperatures, diffusion limitations become more predominant resulting in the intermolecular reaction, which is much slower and therefore requires higher residence times to take place. This difference in the rate of reaction of the inter- and intramolecular paths is due to the involvement of two adjacent acid sites for transalkylation making it difficult to take this route as

compared to the one acid site required for the isomerization path. Inside the zeolite pores the intrinsic diffusivity of p-xylene was more than 1000 times faster than those of the other two isomers [Guisnet et al., 2000].

Another factor which plays a significant role in the ratio of the intra to intermolecular isomerization is the nature of the active sites. Brϕnsted sites favour intramolecular isomerization while Lewis sites favour transalkylation and hence intermolecular isomerization [Guisnet et al., 2000].

1.8 Conclusion of literature review

From the literature review, the connection between crystallinity and activity is clearly illustrated. The crystallinity of a structure is related to the morphology and the chemical properties. Morphology includes factors such as crystal size, porosity and crystal geometry. Chemical properties includes the ratio of silica to alumina present within the framework and the nature of the coordination of the acid sites. Crystallinity can be altered by altering chemical properties through changing the composition of the synthesis mixture or through dealuminating the structure after synthesis. Morphology on the other hand can be altered by changing the synthesis temperature or time. All these factors affect activity in different ways. Small crystal sizes result in large surface areas and therefore an increase in activity. Micropores have larger surface areas as compared to meso and macropores and the crystal geometry can either enhance or inhibit diffusion of molecules inside the pores. Aluminum incorporated within the structure was shown to be the cause of the zeolites acidity and activity and FAL formed the strong sites while EFAL formed the weak sites. All these results tend to suggest that increasing crystallinity should result in an increase in activity. Diffusivity is related to the porosity of the structure. Large microporous crystals will have much high diffusion resistance than small crystals containing meso/macropores. As porosity depends on crystallinity, it is expected that diffusion limitations will depend on crystallinity.

1.9 Hypothesis

1. The intrinsic activity of the catalyst increases with an increase in crystallinity.
2. The conversion goes through a maximum as a result of increased diffusion limitations of the highly crystalline material.

1.10 Objective

- To prepare partially ZSM-5 catalysts and to characterize the porosity using nitrogen adsorption at 77 K
- To investigate the activity and selectivity of the partially crystalline ZSM-5 using *para*-xylene isomerization
- To evaluate the intrinsic catalyst parameters (rate constant, diffusivity) using a reaction diffusion model
- To develop a relationship between the intrinsic parameter and the physical properties of the catalyst.

Chapter 2

EXPERIMENTAL

2.1 Preparation of the catalysts

2.1.1 Synthesis mixture

Step 1 Solution A: A sodium aluminate solution was prepared from 4.475 g of 97 % NaOH and 0.675 g of 99 % $Al(OH)_3$ and 20 ml distilled water in a 100 ml glass beaker. The mixture was heated at 80 °C and stirred at a rate of 200 r.p.m. until a clear solution was obtained.

Step 2 Solution B: A tetrapropylammonium (TPA) brömide solution was prepared by mixing 7.425 g of tetrapropylammonium brömide with 20 ml distilled water in a 100 ml glass beaker and stirring without heating until the solids dissolved.

Step 3 Solution C: A silica slurry was prepared from 80.4 g fumed silica (SiO_2) to which 170 ml of distilled water was added in a 500 ml glass beaker, the mixture was then stirred vigorously until a smooth slurry was obtained.

Step 4: Solution A and B were added to solution C under vigorous stirring followed by the addition of 110 ml of distilled water.

2.1.2 Operation

The synthesis mixture, which was approximately 320 ml, was then transferred into a 500 ml stainless steel autoclave, which was operated at temperatures ranging from 25 to 190 °C under autothermal pressure to obtain samples of different crystallinities. Temperature was controlled by a programmable PID controller which was ramped up at a rate of 10 °C/min and then left to react for 72 hours at the desired temperature. The mixture was then allowed to cool until it reached room temperature.

2.1.3 Post-synthesis treatment

Step 1 Drying: The solid material was left to settle in a 500 ml glass beaker for one hour and the supernatant liquor was decanted. The catalyst was then mixed thoroughly with 100 ml deionized water, centrifuged at a rate of 5000 r.p.m for 5 minutes and again the supernatant liquor was

decanted. The centrifugation/washing step was repeated three times. The catalyst was then dried in an oven at 80-90 °C for 16 h.

Step 2 Calcination: Calcination was done to remove the TPA template. The dried catalyst was placed in a 300 mm long, 16 mm I.D. tubular stainless steel reactor. The heating rate was set at 10 °C/min and nitrogen was passed over the catalyst at 500 °C and 60 ml/min (STP) for 8 hours, after this air was passed at the same temperature and flow rate for a further 16 hours.

Step 3 Ion exchange: Ion exchange was carried out to exchange the Na^+ ion with the NH_4^+ ion. This was done by gently boiling the Na^+ form in a 2M NH_3NO_3 solution at a temperature of 80 °C under reflux conditions for 24 hours in a glass culture vessel (1 liter for every 15 g of catalyst). After this the catalyst was washed again with deionized water, centrifuged three times and dried at 80-90 °C for 16 hours.

Step 4 Calcination/drying: The catalyst was heated using the calcination rig at 500 °C in the presence of air flowing at 60 ml/min (STP) for 3 hours.

The yield obtained from this procedure was 10 gram of catalyst.

2.2 XRD analysis

Crystallinity was measured using a Phillips X-ray diffractometer and a CuKα radiation source was used to obtain the powder X-ray diffractograms. A wavelength of 1.542Å at 40 kV and 25 mA with the ZSM-5 in its hydrogen form was used, with a scanning range of $4 < 2\theta < 47$. The sample was finely ground and placed in a glass holder measuring 2 x 2 cm and scanned using 1019 points per scan with a step size of 0.05 (2θ) and a sampling rate of 2.

2.3 Nitrogen adsorption at 77 K

A micromeritics ASAP 2000 was used to obtain adsorption isotherms. A sample of approximately 0.5 g of zeolite was dried at 350 °C for 24 hours under vacuum (0.06 kPa). The sample was then placed into a sample tube and nitrogen was adsorbed onto it at its boiling point (77 K) using 150 relative pressure points ranging from 0.0001 to 0.99. The adsorption/desorption isotherms, which are a measure of volume adsorbed as a function of relative pressure, were obtained.

2.3.1 BET analysis

BET analysis was done using multi-point plot method. This method works by taking a series of points from the nitrogen adsorption isotherm. BET is used to calculate monolayer coverage and total surface area. Monolayer adsorption takes place within the micropores while external area is obtained from adsorption in the mesopores. The chosen relative pressure range should include the shift from micropore to mesopore adsorption. The pressure range 0.06 to 0.2 P/P_o, which best approximates the micro-mesopore adsorption is used to estimate the mono-layer adsorbed volume by fitting the BET isotherm to the data. The surface area is obtained from this analysis by taking the monolayer adsorbed nitrogen and dividing it into the average molecular cross sectional area of nitrogen which is $0.162nm^2$.

2.3.2 t-plot analysis

The t-plot is used to analyze micropores by calculating micropore area and volume and external surface area. This is an extension of BET analysis because whereas BET analysis analyses the range between end of micropore filling and beginning of mesopore filling the t-plot analyses from beginning of micropore filling until the end of mesopore filling. Analysis starts at pressures below 10^{-4} since this is the beginning of micropore filling and ends at relative pressures of 0.99 which is where saturation is reached. The statistical thickness of each adsorbed layer from monolayer is obtained from the thickness equation as shown in equation 2.1. When making a plot of the volume adsorbed as a function of the statistical thickness the micropore volume is obtained from the y-intercept of a line drawn tangent to a region of relative pressure range of 0.12 to 0.27 which corresponds to 3.5<t<5 as shown in Figure 2.1 and the slope of this line gives the total surface area. The micropore area is found by deduction the external surface area from the total surface area obtained from BET analysis.

$$t = \left[\frac{13.9900}{\left(0.0340 - \log\left(\frac{P}{P_o}\right)\right)}\right]^{0.5} \tag{2.1}$$

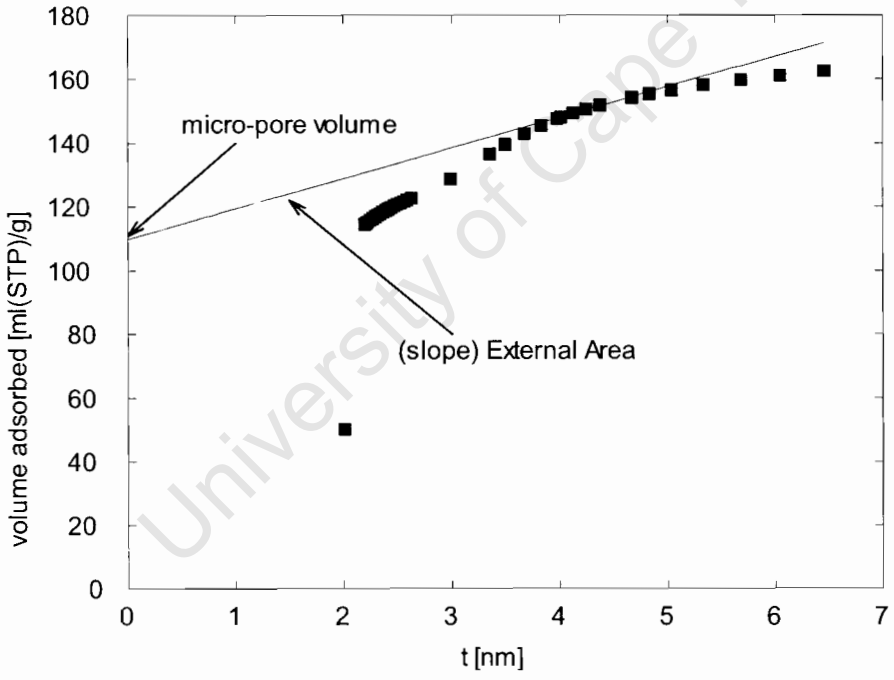

Figure 2.1: t-plot using the Harkins-Jura, Halsey Isotherm

2.4 Scanning Electron Microscopy analysis (SEM)

A Fully Analytical Scanning Electron Microscopy (LEO S440) was used for this analysis. Sample preparation involved sprinkling dry powder on a steel stub coated with glue containing graphite. Here, graphite is used to conduct electrons thereby preventing charge build up. The samples were then coated with carbon as carbon does not interfere with elemental analysis. Images were collected using a Four

Quadrant Back Scatter Detector. An Energy Dispersive X-ray Analyzer (EDX) fitted with a Fisons Kevex Detector and a voltage of 10kV was used for elemental analysis.

2.5 Bulk elemental analysis (HPLC)

Ion chromatography is a form of liquid chromatography that uses ion-exchange resins to separate atomic or molecular ions based on their interaction with the resin. The column is packed with a stationary phase which is made up of tiny polymer beads with negatively charged centers. The sample in powder form, consisting of Si, Al and Na ions, was dissolved in hydrofluoric acid (analyte). The analyte solution was then mixed with a solution (effluent) made up of 2% borate/gluconate concentrate, 2% n-butanol, 12% acetonitrile and diluted with 84% deionized water. This phase is known as the mobile phase. Separation is based on the forces of attraction between the different cations in the solution and the stationery phase. Some cations will adhere strongly to the stationery phase thereby taking longer to pass through the column while others will adhere weakly and pass through the column faster. The different speeds of the ions through the column result in separation of the analyzed sample. The end results are analyzed by an ultra violet detector. Each time analyte molecules emerge from the column the detector sends in a signal which is interpreted as a peak on the integrator output. The number of peaks corresponds to the type of cations in the analyte solution. The peak area is directly related to the concentration of that specific cation in the analyte. Different components are identified by their retention times as obtained from their pure samples. The flow rate of the mobile phase was kept at 1.0 ml/min.

2.6 Reaction analysis

2.6.1 Reactor system

The schematic diagram of the apparatus is shown in Figure 2.2. All lines after the saturator were kept at a temperature of 170 °C. The argon flow rate into the system was controlled by mass flow controller (MFC1) operating between 0 and 600 ml/min (STP). Valve (V2) was adjusted either to connect the saturator on-line or to by-pass the saturator. When the saturator was online the gas stream went into the water jacketed saturator which is shown in Figure 2.3. The glass saturator had a capacity of 110 ml and was filled with liquid p-xylene, 99+% HPLC grade to a level of 80 %. The gas was dispersed into the liquid using a frit. The temperature of the saturator was kept constant at 40 °C using a water bath. At this temperature the vapor pressure of p-xylene was 2.67 kPa. The exiting stream left through V3. V4 was used to switch between on-line and by-pass reactor operation.

The reactor shown in Figure 2.4 was made of stainless steel with graphite seals at the lid to prevent leaking. The reactor length was 250 mm with an internal diameter of 17 mm. The inlet and outlet were made of 1/4" stainless steel tubes with the inlet at the bottom and the outlet at the top. The furnace temperature was controlled by a programmable PID controller with an accuracy of ±0.5 °C. The thermocouple was inserted inside a thermowell located within the catalyst bed to record the catalyst temperature. The reactor was covered with ceramic wool at all times to prevent heat loss to the surroundings and maintain isothermal conditions.

The catalyst bed packed inside the reactor consisted of 0.5 g of the prepared catalyst in powder form which was intimately mixed with 5 g of HCl purified sand particles. The catalyst bed was 30 mm in length and was held in place with quartz wool plugs. The reaction products were sampled using a gas sampling valve with a 50 μl sample loop and analyzed with a GC. Needle valve (V7) was used to maintain a constant pressure of 140 kPa for all runs.

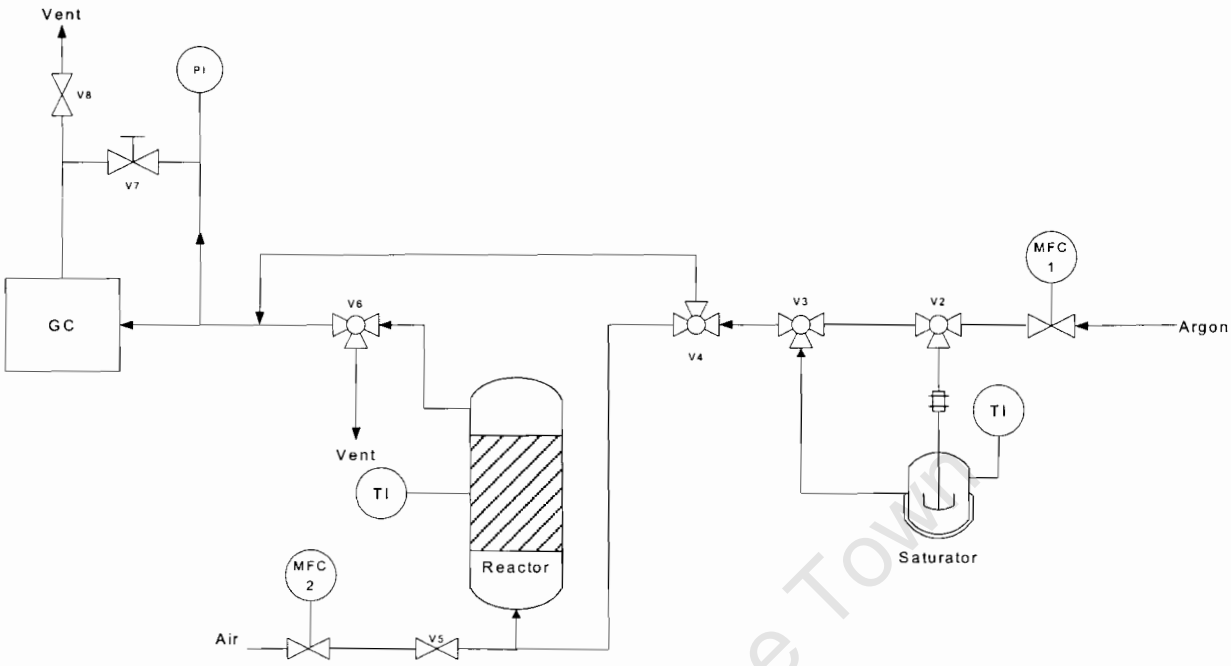

Figure 2.2: Schematic flowsheet of the reactor system

A GC (HP 5890) fitted with a Flame Ionization Detector (FID) and a column made up of fused silica with BP20 (polar) as the stationary phase, 50 m in length with an internal diameter of 0.53 mm was used. Column temperature was maintained at 90 °C, detector temperature at 280 °C and injector temperature at 240 °C.

2.6.2 Reactor system leak test

In order to test for leaks in the reactor and GC column, MFC1 was first calibrated with a bubble meter. To calibrate MFC1 the saturator, reactor and GC were by-passed and the flow rate measured by a bubble meter situated after V8. To do a leak test, the empty saturator, empty reactor and GC were put on-line and the flow rate recorded by a bubble meter situated after V8. When these two flow rates for MFC1 calibration and for leak test differed by less than 1ml/min the system was considered to be leak free.

2.6.3 Product analysis

Prior to use, the column was conditioned at a temperature of 200 °C for four hours. This conditioning ensured proper functioning of the column, as it was necessary to flush trace amounts of impurities and side products collected in the column.

In order to verify the retention times of the isomers, the saturator was filled with a pure sample for each of the isomers. The reactor was by-passed and GC analysis took place. The integrator (HP 3390A) output gave one peak at the specific retention time. In this way the retention times of all isomers were obtained.

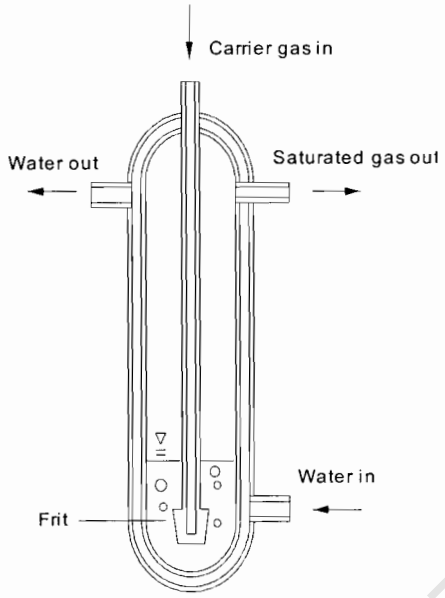

Figure 2.3: Para-xylene saturator

To find if the area counts recorded by the integrator corresponded to the concentrations of all the analyzed components, the saturator was filled an equimolar mixture of all the three isomers. The reactor was set to by-pass and the mixture analyzed by the GC. The ratio of the area counts was then compared to the ratio of the equimolar mixture. Results showed that the area count ratios were equal to those of the calibration mixture indicating that all response factors were unity.

2.6.4 Procedure

Conditions used for experiments are shown in table 2.1:

Step 1 Calcination was carried out by setting the reactor to vent through V6 and passing 80 ml/min (STP) of air over the catalyst which was maintained at 500 $^{\circ}C$ for 16 hours. The reactor was then cooled to the reaction temperature.

Step 2 The reactor was then by-passed to stabilize flow through the saturator, to check flow rate using bubble meter connected at the vent (V8) and to analyze feed on the GC.

Step 3 The reactor was put on line to analyze products on the GC until steady state was reached which took approximately 45 minutes. Two product samples were then taken.

Step 4 MFC1 was then adjusted to the four different flow rates in random order and steps 2 and 3 were repeated for each case.

Step 5 A new reaction temperature as indicated in table 2.1 was then chosen and steps 1 to 4 repeated.

Step 6 The reactor was then packed with a new catalyst and steps 1 to 5 were repeated.

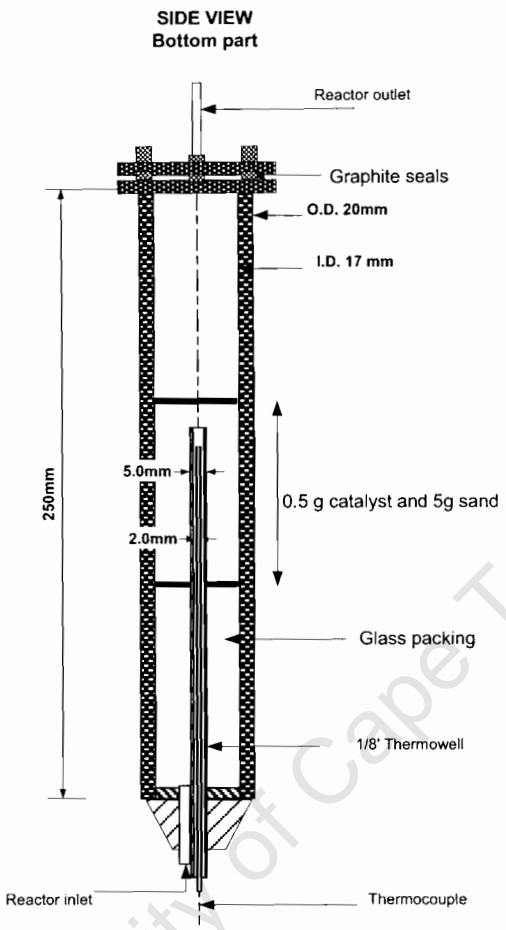

Figure 2.4: Schematic diagram of the reactor

2.6.5 Mass balance

A mass balance was done on the incoming and exiting gas streams to ensure that the mass entering was equal to the mass exiting. This was done by by-passing the reactor and comparing the flow measured from a bubble meter placed after V8 to flow measured during on-line analysis. In all cases, the error between the inlet and exit volume flow rates was less than 0.042 % indicating that there were no leaks in the reactor.

A carbon balance was carried out by comparing by-pass and on-line analysis. Figure 2.5 shows the plot of area count for by-pass and for on-line for different samples.

This carbon balance was done in order to check that no other side products, which are getting stuck inside the column and therefore not being integrated by the integrator are formed. On-line analysis area count should equal by-pass since all products formed are formed from the *para*-xylene reacted. Standard deviation for the mass balance was ± 4.1 %

These results show that the mass balance was acceptable.

Table 2.1: Experimental conditions

Temperature [°C]	**Catalyst mass** [g]	**Flow rate** [cm^3/s]	**Catalyst volume** [cm^3]	**Residence time** [s]	**WHSV**** [hr^{-1}]
250	0.5	2.05	0.29	0.14	0.70
	0.5	4.67	0.29	0.064	1.58
	0.5	7.02	0.29	0.044	2.38
	0.5	11.15	0.29	0.030	3.78
300	0.5	2.24	0.29	0.13	0.76
	0.5	5.12	0.29	0.062	1.74
	0.5	7.70	0.29	0.042	2.61
	0.5	12.22	0.29	0.024	4.14
350	0.5	2.44	0.29	0.12	0.83
	0.5	5.57	0.29	0.053	1.89
	0.5	8.37	0.29	0.031	2.84
	0.5	13.29	0.29	0.022	4.51

**Weight Hourly Space Velocity [$g_{feed}g_{cat}^{-1}hr^{-1}$]

2.6.6 Data analysis

Conversion is defined by equation 2.2:

$$X = 1 - \frac{F_{para\text{-xylene,out}}}{F_{para\text{-xylene,in}}} \tag{2.2}$$

while the yield is given by equation 2.3:

$$Y = \frac{F_{\text{species i,out}}}{F_{para\text{-xylene,in}}} \tag{2.3}$$

Because the standard deviation in carbon balances were less than 4.1 %, the approximation that $F_{xylenes,in}$=$F_{xylenes,out}$ is acceptable Also, as these are all aromatic molecules of similar structure, all response factors are unity. Thus the area count in the product analysis is proportional to the molar flowrate of the xylenes. Thus equations for conversion and yield may now be replaced by equations 2.4 and 2.5 respectively:

$$X = 1 - \frac{A_{para\text{-xylene}}}{\sum_{\text{xylenes}} A_i} \tag{2.4}$$

$$Y_i = \frac{A_{\text{i}}}{\sum_{\text{xylenes}} A_i} \tag{2.5}$$

2.6.7 Confirmation that sand packing is inert

To confirm that the sand packing was inert a run was carried out using a bed made up of sand particles only. The resulting product stream consisting of only one peak from the *para*-xylene showed that the sand was inert.

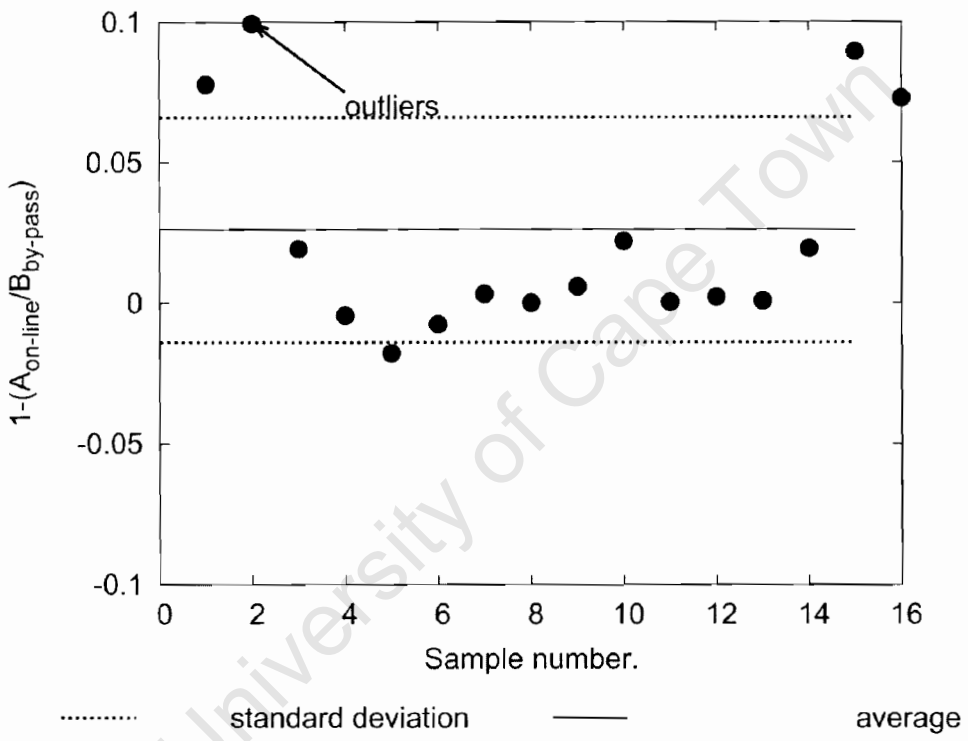

Figure 2.5: Carbon mass balance over the reactor system.

Chapter 3

REACTOR MODEL

3.1 Assumptions

The assumptions made in modelling this system were:

i the flow regime is that of a plug flow system;

ii Fickian diffusion holds, and diffusion coefficients are independent of position and concentration;

iii adsorption kinetics follow linear isotherms;

iv acid sites are distributed homogeneously through the catalyst volume

v that the system reaches and maintains steady state.

Spherical geometry and flat plate geometry can be related through the Thiele modulus by the following similarity:

$$L_{plate} = 3R_{sphere} \tag{3.1}$$

therefore for ease of calculations derivations to analyse experimental data are based on a flat plate geometry.

3.2 Reaction kinetics

$$pX \overset{k_{px}}{\rightleftarrows} mX$$

$$mX \overset{k_{mx}}{\leftrightarrows} oX \tag{3.2}$$

Equation 3.2 represents the first order reversible reaction expression for the isomerization of *para*-xylene where k_{mx} and k_{px} are the reaction rate constants for *para*-xylene and *meta*-xylene respectively. Since the reaction was carried out at high temperature and low xylene vapor pressure, there is a linear relation between the *para*-xylene concentration in the bulk gas and on the adsorbate surface. The first order rate expression is therefore employed by lumping together the adsorption equilibrium constants with the rate constants.

Assuming ideal gas behavior, the equilibrium constants K_{e1}:K_{e2} for this reaction have been found, from thermodynamic equilibrium, to be 2.25:0.37, 2.21:0.38 and 2.19:0.395 at 250, 300 and 350 °C respectively. Equations 3.3, 3.4 and 3.5 represents the rate equations for this reaction.

$$r_{pX} = -k_{pX}\left(c_{pX} - \frac{c_{mX}}{K_{e1}}\right) \tag{3.3}$$

$$r_{mX} = k_{pX}\left(c_{pX} - \frac{c_{mX}}{K_{e1}}\right) - k_{mX}\left(c_{mX} - \frac{c_{oX}}{K_{e2}}\right) \tag{3.4}$$

$$r_{oX} = k_{mX}\left(c_{mX} - \frac{c_{oX}}{K_{e2}}\right) \tag{3.5}$$

where c_{mX} is the concentration of *meta*-xylene in the gas phase

c_{pX} is the concentration of *para*-xylene in the gas phase

where c_{oX} is the concentration of *ortho*-xylene in the gas phase

3.3 Model equations

3.3.1 Reactor mass balance

A reactor mass balance yields:

$$\frac{dF_i}{dV_{zeolite}} = r_{i,ave} \tag{3.6}$$

where dF_i is the flow of species i across a differential area

$dV_{zeolite}$ is the volume of the zeolite across a differential area

$r_{i,ave}$ is the average reaction rate for the catalyst pellet

Assuming a constant density system at constant pressure and no change in the number of moles implies $Fi=QC_i$, which, after manipulation and substitution into equation 3.6 yields equation 3.7

$$\frac{dC_{zi}(\tau)}{d\tau} = r_{i,ave} \tag{3.7}$$

$$\tau = \frac{V_{zeolite}}{Q} \tag{3.8}$$

where Q is the volumetric flow

$C_{zi}(\tau)$ is the concentration for component i in the reactor i.e. the z domain

τ is the residence time of the reactant species in the reactor i.e. the z domain

$r_{i,ave}$ can be obtained from a mass balance across the zeolite film.

3.3.2 Zeolite pore mass balance

Considering the molar flux:

$$W_i = -D_i \frac{\partial c_i(\tau, x)}{\partial x} \tag{3.9}$$

where D_i is the diffusion coefficient for species i

Species i and x are the spatial coordinate for the zeolite pellet.

equation 3.10 represents a material balance of species i diffusing through an area Az across the defferential element at any residence time (i.e., position) τ in the bed and thus the concentration is both a function of x and τ

$$W_i.A_z \mid_x - W_i.A_z \mid_x + \Delta x + ri.A_z.\Delta x = 0 \tag{3.10}$$

where r_i is a volume-based reaction rate. Division by $A_z \Delta x$, substitution of W_i and defining dimensionless variables $y_i = \frac{c_i(z,\tau)}{c_o}$ and $U = \frac{x}{L}$ yields the dimensionless 2^{nd} order partial differential equation 3.11 for the zeolite at any position z in the reactor as Δx tends to 0.

$$\frac{\partial^2 y_i(\tau, U)}{\partial U^2} + \frac{L^2}{D_i c_o} r_i(\tau, U) = 0 \tag{3.11}$$

where c_o is the total initial xylene feed concentration

y_i is the gas phase mole fraction on the external surface, based on xylene concentration, for species i

L is the length of the zeolite pore

The solution to equation 3.11 requires 2 boundary conditions.

At the center where x=0, $(U = 0)$, therefore the first boundary condition is given by equation 3.12.

$$\frac{\partial y_i}{\partial U} \mid_{\tau,0} = 0 \tag{3.12}$$

At the gas solid interface, where x=L ($U = 1$), assuming film resistance is negligible, the concentration in the bulk gas and at the surface must be equal, thus equation 3.13.

$$y_i(\tau, 1)\, c_o = C_{zi}(\tau) \tag{3.13}$$

The average reaction rate across the zeolite ($r_{i,ave}$) at any τ can now be evaluated (equation 3.14).

$$r_{i,ave} = \frac{\int_0^V r_i dV}{\int_0^V dV} = \int_0^L r_i A_z dx = \frac{\int_0^1 r_i dU A_z L}{A_z L} \tag{3.14}$$

To obtain the second boundary condition requires the manipulation of the reactor and zeolite mass balances.

3.3.3 Combining the reactor and zeolite mass balance

Equation 3.14 can be evaluated by using equation 3.11 to yield equation 3.15

$$r_{i,ave} = \frac{D_i c_o}{L^2} \cdot \frac{\partial y_i}{\partial U} \mid_{\tau,1} \tag{3.15}$$

The effectiveness factor (η_i) is thus given by equation 3.16.

$$\eta_i = \frac{\int_0^V r_i dV}{r_{is} A_z L} = \frac{D_i c_o}{L^2 r_i s} \frac{\partial y_i}{\partial U} \mid_{\tau,1} \tag{3.16}$$

Substitution of equation 3.8 and using equation 3.13 yields the second boundary equation (3.17)

$$\frac{\partial y_i(\tau, 1)}{\partial \tau} = \frac{D_i}{L^2} \frac{\partial y_i}{\partial U} \mid_{\tau,1} \tag{3.17}$$

The equations 3.11, 3.12 and 3.17 represent the final model equations.

3.3.4 Solution of model equations

An orthogonal collocation technique is employed to discretize equation 3.11 into a set of algebraic equations (equation 3.18),

$$\sum_{j=1}^{N+1} B_{ij} y_{kj} + \frac{r_k(\tau, U)}{c_o} \frac{L^2}{D_k} = 0 \qquad k = 1, 2, 3 \qquad i = 1...N \tag{3.18}$$

where U_i is the coordinate node defined by the collocation procedure, B_{ij} is the collocation coefficient matrix representing the 2^{nd} derivative, N the number of internal collocation points, and k=1,2,3 represents the *para*-xylene, *meta*-xylene and *ortho*-xylene species, respectively.

Using a symmetry transform, the support boundary condition (equation 3.12) is automatically satisfied. The 2^{nd} boundary condition (equation 3.17) is also discretized to yield an ordinary differential equation (equation 3.19),

$$\frac{dy_{ki}}{d\tau} = \frac{D_k}{L^2} \cdot \sum_{j=1}^{N+1} A_{N+1,j}\, y_{kj} \tag{3.19}$$

where A_{ij} is the collocation coefficient matrix representing the 1^{st} derivative.

Equations 3.18 and 3.19 are repeated for each species k=1...3. They represent a set of differential-algebraic equations (DAE) which are solved using the implicit integrator DDASAC. Sufficient accuracy of the steep gradients was obtained with N=30.

3.3.5 Estimation of model parameters from experimental data

To enable the extraction of the model parameters, further assumptions had to be made. It was assumed that D_{pX}:D_{oX}:D_{mX}=1:100:1000 and k_{pX}=2k_{mX} [Chen et al., 1994]. The result was a 2-parameter model. A Levenberg-Marquardt routine was then employed to evaluate these parameters, with the least squares criterion defined by equation 3.20

$$Error = \sum_{j}^{Nspecies} \sum_{i=1}^{N\exp} \left[y_{\exp(i,j)} - y_{\mathrm{mod\,el}(i,j)} \right]^2 \tag{3.20}$$

3.3.6 Typical response curves as a function of diffusion resistance

The effects of diffusion resistance on the catalysts properties of the catalyst's were simulated by taking k_{pX}=6.7 and varying the diffusion time constant by six orders of magnitude and plotting the corresponding response curves. Figure 3.1 shows that increasing the diffusion time constant (larger diffusion limitations) decreases the conversion and makes the catalyst less active, as expected. More interestingly, Figure 3.2 shows that the *meta*-xylene yield decreases and the *ortho*-xylene yield increases with an increasing diffusion time constant. Under strong diffusion limitations both *meta*-xylene and *ortho*-xylene appear as primary products with *ortho*-xylene being preferentially produced. This signifies an apparent change of mechanism from the series reaction *para*-xylene⇌ *meta*-xylene⇌ *ortho*-xylene to a parallel reaction *para*-xylene⇌mX, *para*-xylene⇌ *ortho*-xylene. This discrepancy is a result of the diffusion resistance imposed by the zeolite on *meta*-xylene and *ortho*-xylene.

Furthermore, the response for $D/L^2=10^3$ shows a small decrease in the conversion but a large shift in the yield curves as shown in Figure 3.2, indicating that the yield data is considerably more sensitive to diffusion limitations than the conversion plots for the typical model parameters used for xylene isomerization. The conversion, or catalyst activity continues to decrease with increasing diffusion limitations. This is in contrast to the yield response which varies between two boundaries. Typically, for all $D/L^2>10^4$ the yield of *meta*-xylene and *ortho*-xylene remains unchanged, and represents the intrinsic selectivity of the

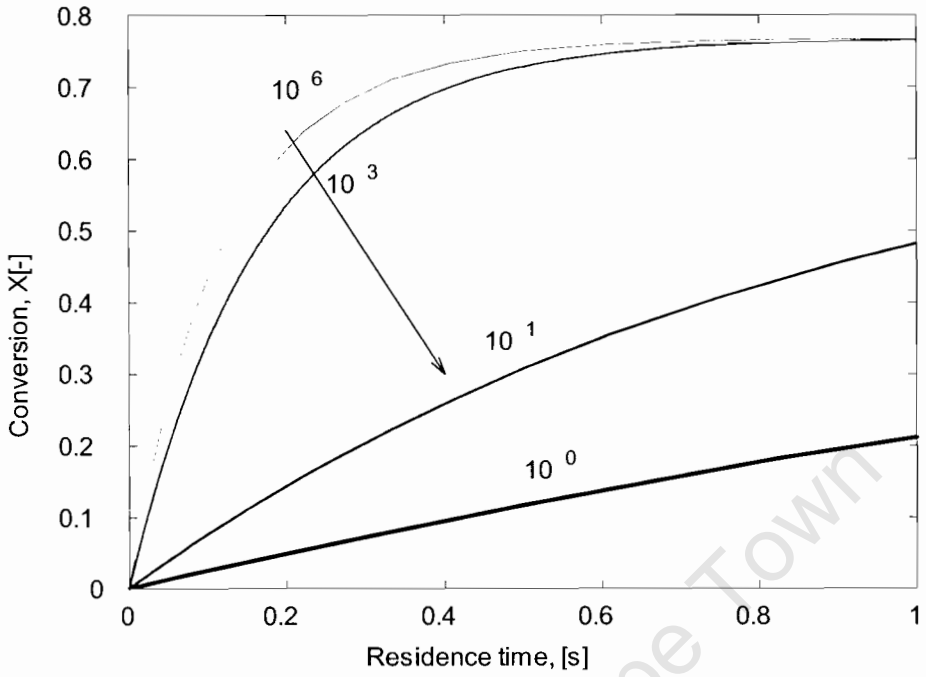

Figure 3.1: Typical para-xylene conversion variation with residence time. Thickness of lines represents severity of diffusion resistance, which increases in the direction of the arrow. Above/below each curve is the diffusion time constants (D/L^2,[s^{-1}]). k_{pX}=6.7s^{-1}.

catalyst. On the other hand, at $D/L^2>10^2$ the yield of *meta*-xylene reaches a minimum while that of *ortho*-xylene reaches a maximum.

Further decreasing D/L^2 will not change the observed yield (or selectivity), although the conversion (or activity) of the catalyst continues to decrease. This is very important information for parameter estimation. It indicates that for this particular value of k_{pX}, diffusion limitations strongly impact on the yield of *meta*-xylene and *ortho*-xylene for diffusion time constants in the range $10^2<D/L^2<10^4$, or about 2 orders of magnitude, in which diffusivity estimation would be most sensitive. Outside the bounds of these limitations it becomes increasingly difficult to estimate accurate diffusion coefficients. Outside the range $10^2<D/L^2<10^4$ it is no longer possible to estimate diffusion coefficients from the experimental data.

Figure 3.3 shows that the yield of *meta*-xylene is highest at low conversion when there are no diffusion limitations. Interestingly, under very strong diffusion limitations (small D/L^2) it is possible for the *meta*-xylene:*ortho*-xylene ratio to exceed that predicted by equilibrium over a wide range of conversions, of course at the expense of very low reactivities. These results may be explained by the following physical reasoning. As resistance to diffusion increases, the slow diffusing *meta*-xylene isomer accumulates in the ZSM-5 pore matrix, thus driving further isomerisation into the faster diffusing *ortho*-xylene. Thus the decreasing *meta*-xylene:*ortho*-xylene ratio with increasing diffusion resistance. These simulations show that to maximize the effect of diffusion on the yield, operating at low conversions would be ideal. At higher conversions, the curves converge towards the chemical equilibrium line, thereby masking the effects of diffusion resistance.

Figure 3.4 shows that the effectiveness factor for *ortho*-xylene (equation 3.21) is much greater than 1, and increasing with increasing diffusion resistance. The effectiveness factor approaches unity at negligible

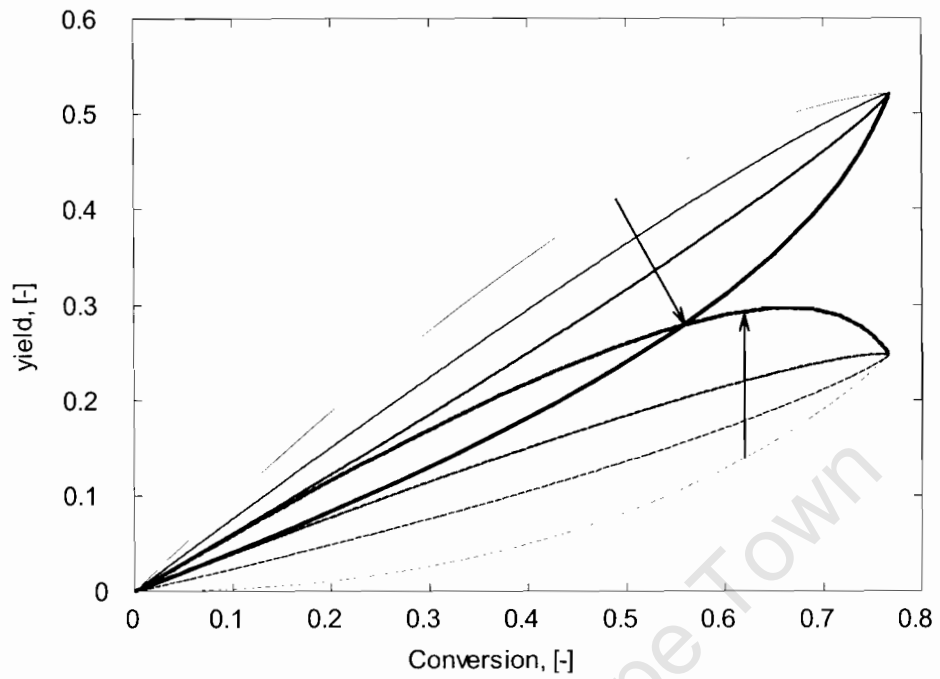

Figure 3.2: Typical meta-xylene and ortho-xylene variation with para-xylene conversion. The broken lines represent ortho-xylene yields, and the solid ones meta-xylene yields. Thickness of lines represents severity of diffusion resistance. In increasing order of the thickness of the lines as indicated by the arrows, the diffusion time constants (D/L^2,[s^{-1}]) are 10^4, $3x10^3$, $1x10^3$ and 10^2. k_{pX}=6.7s^{-1}.

diffusion limitations and near equilibrium as expected. These observations can be explained with the following arguments.

At low conversions, the reaction rate is highest, thus *meta*-xylene is formed at a high rate. Since it cannot escape with as much ease as the other isomers, its concentration rises within the particle, being highest at the centre. It must therefore convert to *ortho*-xylene. Because on the outside surface the *meta*-xylene concentration is much lower than in the zeolite pores, the rate of formation of *ortho*-xylene is also very low, thus

$$\eta_{oX} = \frac{r_{oX(average)}}{r_{oX(on\ the\ surface)}} >> 1 \tag{3.21}$$

η_{oX} should be highest at low *para*-xylene conversion, where the rate of formation of *meta*-xylene is the greatest, as observed. At higher conversions, some *meta*-xylene will escape to the surface and the reaction to *ortho*-xylene on the surface will slow down. Hence η_{oX} decreases with increasing *para*-xylene conversion.

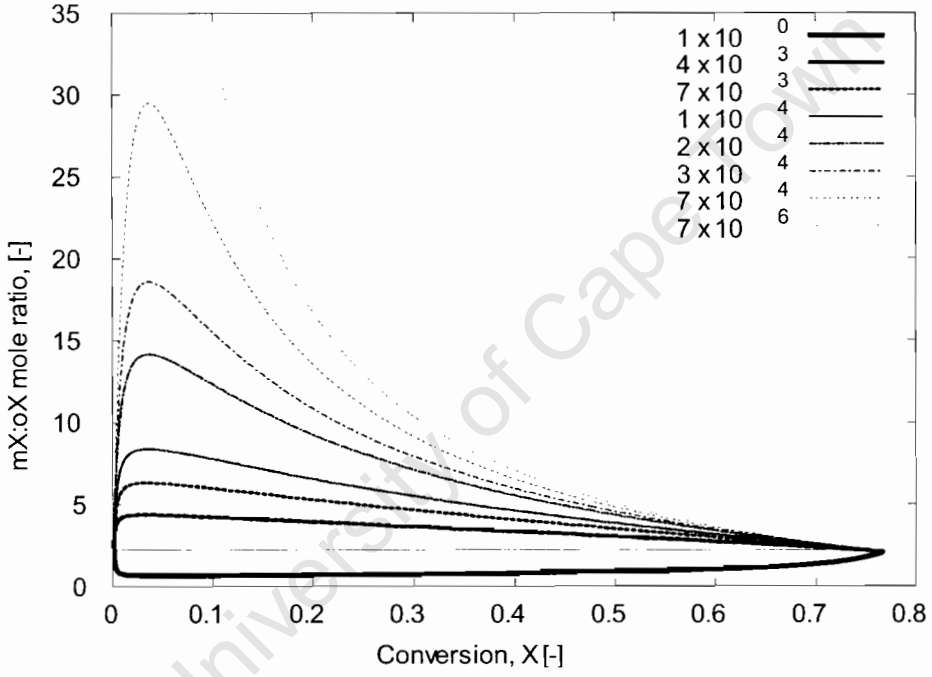

Figure 3.3: Typical meta-xylene:ortho-xylene dependencies on para-xylene conversion. Legend shows diffusion time constants (D/L^2,[s^{-1}]). k_{pX}=6.7s^{-1}. The thin solid line represents equilibrium

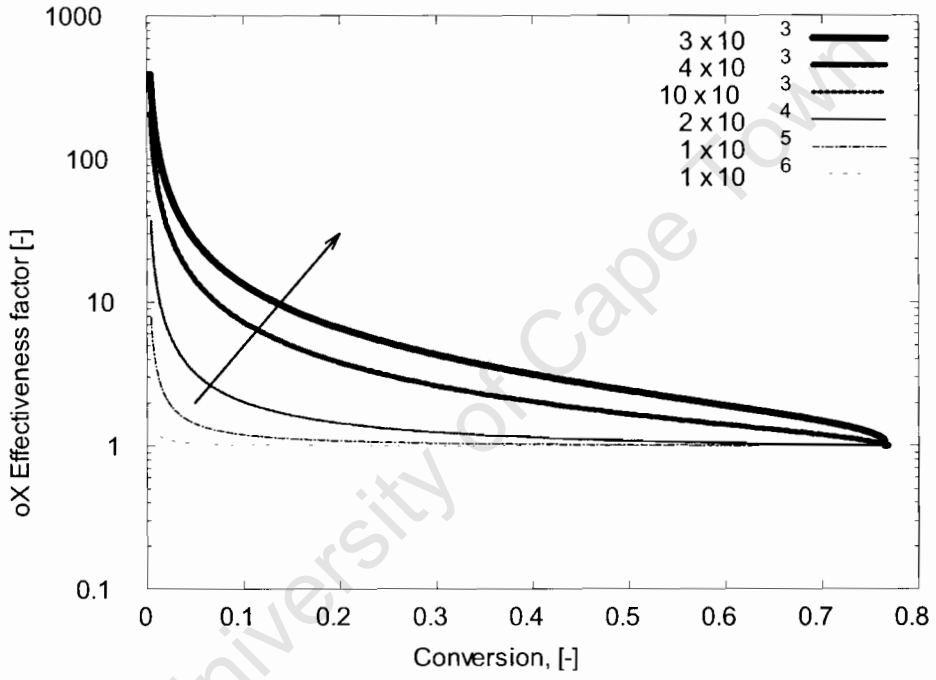

Figure 3.4: Typical ortho-xylene effectiveness factor as a function of para-xylene conversion. Thickness of lines represents severity of diffusion resistance. Arrow shows movement of η_{ox} as diffusion resistance increases. Legend shows diffusion time constants (D/L^2,[s^{-1}]). k_{pX}=6.7s^{-1}.

Chapter 4

RESULTS

4.1 Catalyst characterisation

All catalyst will use the nomenclature given in Table 4.1. Thus the catalyst synthesized at 125 °C will be named ZS125.

4.1.1 XRD

Figure 4.1 shows that the intensity of the major peaks increases with an increase in synthesis temperature. The crystallinity for each sample, as estimated using equation 1.1, shows that the crystallinity increases with increasing synthesis temperature (Table 4.1). These results correspond to those observed in literature [Nicolaides, 1999] and shown in Figure 1.5 in section 1.4.

4.1.2 Crystal morphology

Figure 4.2(a) shows that ZSM-5 prepared at 50 °C produces large ($\gg 10$ μm), irregular and amorphous particles similar to the products of the first step of the mechanism of crystallization which cannot be classified as ZSM-5 (see section 1.3). Such particles are similar to grains of sand and are essentially non-porous. The smaller particles ($\ll 1$ μm) which are visible in Figure 4.2 might be precursors to ZSM-5 crystals and could account for the low crystallinity, micropore volume and micropore surface area measured from an analysis of the N_2 adsorption isotherm (see Table 4.2). The crystal size for the zeolite fraction in ZS50 could not be estimated. Figures 4.2(b) and (c) show that zeolites prepared at 100 and 125 °C have well defined crystals with sizes between 0.2 - 1 μm. Particularly in ZS100, amorphous material is visible in these SEM images corresponding to the background noise in the XRD spectrum. The crystallinities are estimated to be of the order of 50-66%. The highly crystalline (>70%) materials are shown in Figures 4.2(d), (e) and (f). The crystal size decreases as the synthesis temperature increases. These materials might well be agglomerates of much smaller crystals. Although ZS190 has the highest crystallinity of these samples, its crystals are not as well defined as suggested by the XRD. The SEM image is a local measurement, while the XRD is a bulk analysis, and thus this image might well be of a highly amorphous region of the sample.

Assuming that the SEM images, at least to a first estimate, represent the crystal sizes, then the size progression with increasing synthesis temperature goes through a maximum at approximately 150 °C.

Table 4.1: Physical characterisation of the prepared ZSM-5

Catalyst	$T_{Synthesis}$	Si/Al molar ratio	Crystallinity	Crystal diameter (SEM)	Morphology
	$°C$		%	μm	
ZS50	50	24.5	20.0	-	amorphous
ZS100	100	26.7	50.0	0.2-1	Crystalline amorphous
ZS125	125	25.1	66.0	0.2-1	Crystalline
ZS150	150	21.7	71.0	0.5-2	Crystalline intergrowth
ZS175	175	28.0	74.0	0.2-1	Crystalline
ZS190	190	18.5	100.0	<0.5	Crystalline small
	Average value	24.0			
	Standard deviation	±3.2			

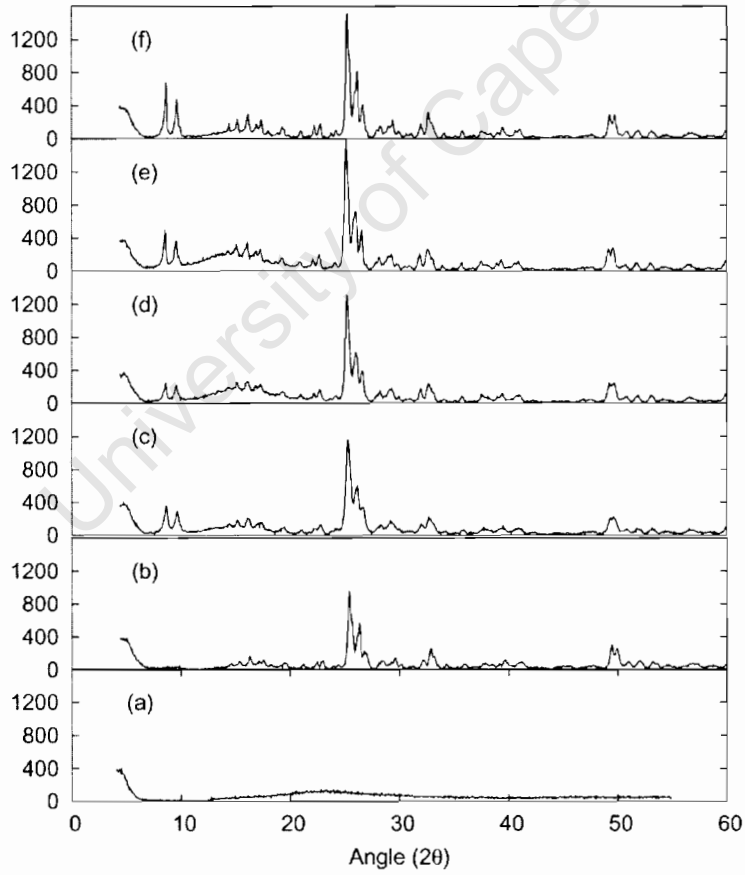

Figure 4.1: XRD spectrum of (a) ZS50, (b) ZS100, (c) ZS125, (d) ZS150, (e) ZS175 and (f) ZS190

This is related to the kinetics of the crystallization process. At low temperature, the rate of crystallization is not fast enough to produce the crystals in a synthesis time of 3 days and only amorphous particles form. As the temperature increases, the rate of crystallization increases and more crystals start forming. The large crystals are a result of kinetic controlled growth, in which sufficient nutrients are supplied and super-saturation occurs at few well defined locations which act as crystal growth centers. As the temperature increases further, super-saturation increases, leading to rapid crystallization uniformly through the whole solution, possibly nutrient mass transfer limited. Thus there are many more growth centers leading to smaller overall crystal size. It should also be borne in mind that temperature (and thus also pressure) changes the liquid solution composition due to nutrients and templates evaporating into the vapor phase, an effect which is difficult to quantify. This could also give rise to a variation in the growth patterns in the zeolites.

4.1.3 Chemical composition

The bulk Si/Al mole ratio (see Table 4.1) plotted in Figure 4.3 was approximately 24 with a standard deviation of 13%. These results are within experimental error of the synthesis procedure and ion chromatography analysis and to all intensive purposes the Si/Al mole ratio can be assumed to be constant for all catalysts. This result was expected since the synthesis composition was constant in all cases. These results suggest that no measurable preferential bulk incorporation of Si or Al was taking place as a function of temperature. This, however, does not mean that there are no Al concentration gradients in these catalysts. It also does not indicate that all the acid sites in the sample are accessible for reaction.

4.1.4 Surface areas and pore volumes

Adsorption within zeolitic materials (micro-,meso- and macropore systems) has the following characteristics. At very low N_2 pressures adsorption occurs almost exclusively within the micropores. The strong zeolite-N_2 interaction within the pores due to the small pore size, leads to rapid condensation of the N_2 molecules into a liquid like adsorbed phase at very low N_2 pressures, before there is significant monolayer coverage of the meso- and macropores. Thus the micropore "monolayer coverage" needs to be viewed as pore filling. At higher N_2 partial pressures all the remaining surface area is essentially covered with a monolayer of molecules. It is this quantity that the BET equation attempts to quantify. Increasing the N_2 pressure even further (typically $\frac{P}{Po}$>0.3) causes multiple layer adsorption to occur within the meso and macropores. A hysteresis loop occurs at these pressures in the adsorption/desorption isotherms due to different rates of condensation and evaporation which occurs within the meso- and macropores. Since the evaporation occurs at a different curvature from the desorption, the desorption occurs at a lower $\frac{P}{Po}$ than the adsorption (i.e. the desorption curve must always lie above the adsorption curve when there is hysteresis).

Figure 4.4 shows typical N_2 isotherms at 77K for the prepared catalysts. At low temperatures (Figure 4.4(c), ZS50) the N_2 loading at low relative pressure is about 5 times lower than for the samples synthesized at higher temperatures (Figures 4.4(a) and (b)). The significant hysteresis loop observed at a relative pressure of approximately 0.9, indicates that ZS50 contains a significant amount of macropores, possibly contained between the large sand-like particles observed in the SEM (Figure 4.2(a)). The hysteresis loop decreases in partially crystalline material. For the highly crystalline material the adsorption curve overlaps the desorption curve as shown in Figures 4.4(b), ZS125 and (c) ZS190 respectively. This indicates the absence of any meso- and macropores. Such isotherms are typical of well formed zeolite crystals normally larger than 1 μm. Since ZS190 is the most crystalline sample and has the smallest crystals, the isotherm clearly indicates that essentially only micropores are present in this catalyst

Table 4.2 shows that the BET surface area increases with an increase in synthesis temperature, the

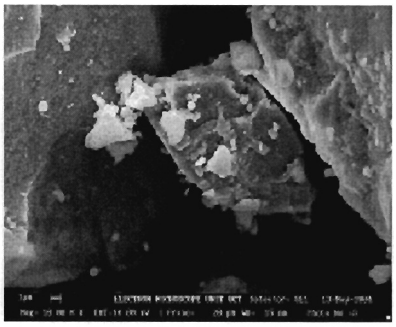

(a) ZS50

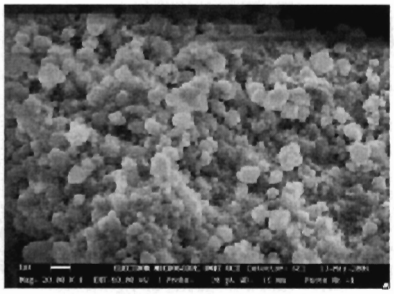

(b) ZS100

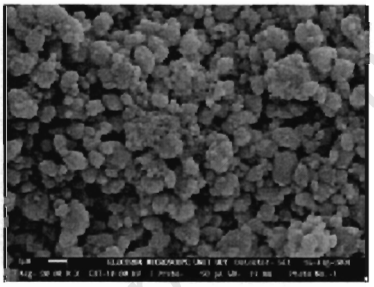

(c) ZS125

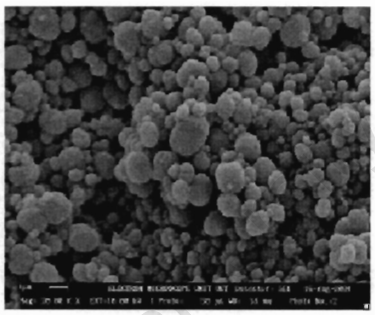

(d) ZS150

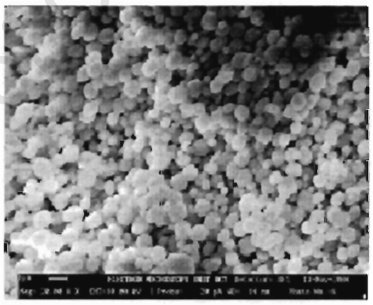

(e) ZS175

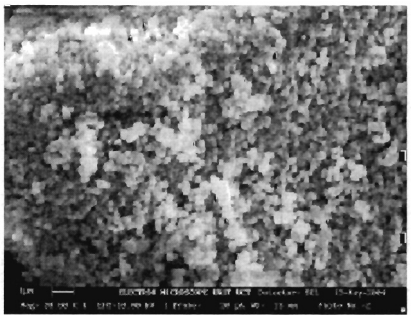

(f) ZS190

Figure 4.2: SEM images of prepared zeolites (see appendix A for enlarged photos)

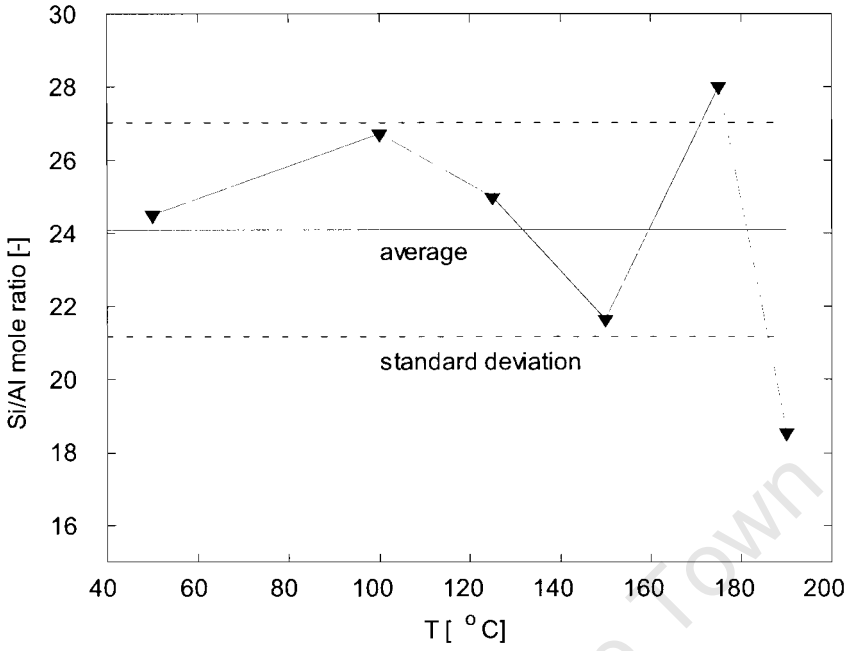

Figure 4.3: Si/Al mole ratio vs synthesis temperature

largest increase occurring between ZS50 and ZS100. These results are supported by the SEM images in Figure 4.2. The BET surface areas obtained for ZS190 exceeds that typical of ZSM5 type zeolites. The BET surface area is representative of the total surface area of the sample, viz. micro-, meso- and macropores, in which typically the micropores[1] make the largest contribution. The BET method cannot distinguish between these different pores.

The Harkins-Jura t-plot method as implemented by the micromeretics ASAP2000 (see section 2.3.2) can be used to make a first order approximation of the micropore volume (V_{micro}) and external surface area ($A_{external}$). Typical t-plots are shown in Figure 4.5. Consistent with SEM images and crystallinity estimates, the micropore volume increases with increasing synthesis temperature (see Table 4.2). The external surface area goes through a maximum at the intermediate synthesis temperatures. Analysis of zeolite data with the t-plot method depends on the choice of t values, which in this case are between 3.5 and 5.0. Clearly, if the later part of the t-plot (t >5) had been used the results obtained for micropore volume and external surface area would have been very different and possibly conform better to the above SEM and XRD observations. For example using the later part of the t-plot (see Figure 4.5), V_{micro} is estimated to be $\approx$ 120-150 ml(STP)/g giving $V_{micro} \approx 0.2$ ml/g. This exceeds the pore volume of a 100 % crystalline ZSM-5 which is 0.18 ml/g.

[1] The BET surface area in the case of micro-pores is a fictitious quantity calculated by approximating micro-pore filling via a mono-layer coverage as a surface area.

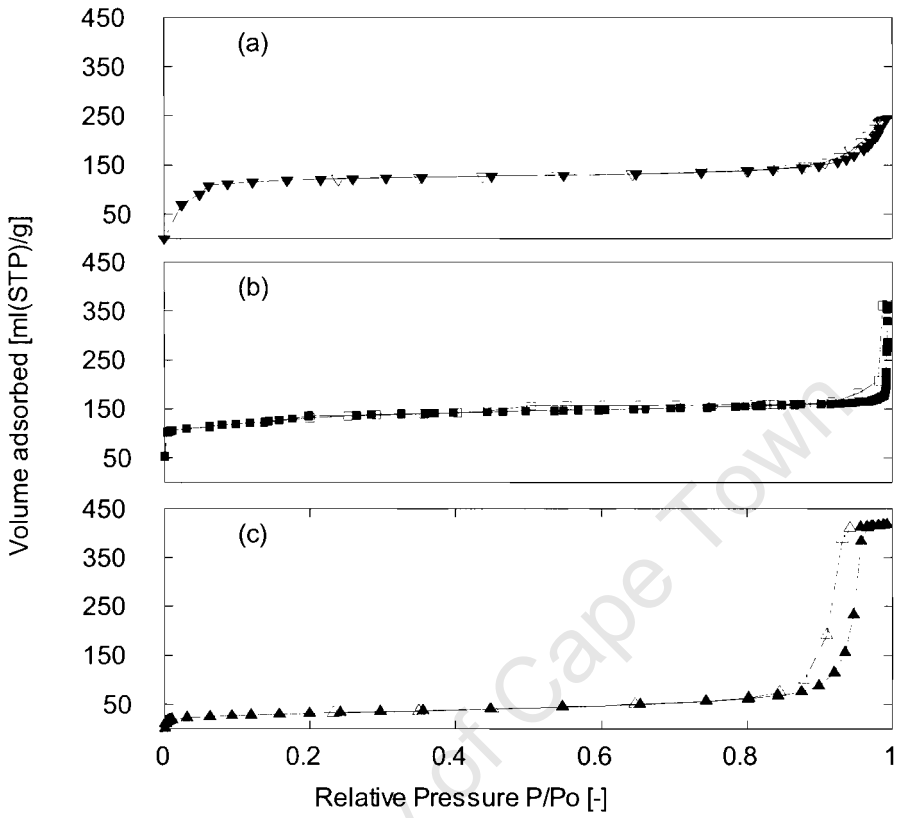

Figure 4.4: Nitrogen adsorption/desorption isotherms at 77 K for (a) ZS190, (b) ZS125 and (c) ZS50. Adsorption : filled; desorption : open symbols

Table 4.2: Analysis of nitrogen adsorption isotherms at 77 K

Sample	A_{BET} m^2/g	V_{micro} m^3/g	$A_{external}$ m^2/g	A_{micro} m^2/g
ZS50	122	0.0056	106	15
ZS100	439	0.048	343	95
ZS125	452	0.088	253	199
ZS150	475	0.128	190	285
ZS175	440	0.134	144	296
ZS190	521	0.164	160	361

A_{micro} is estimated as A_{BET} - $A_{external}$ by the Micromeretics ASAP2000
A_{BET} for typical ZSM5 is between 350-450 m^2/g

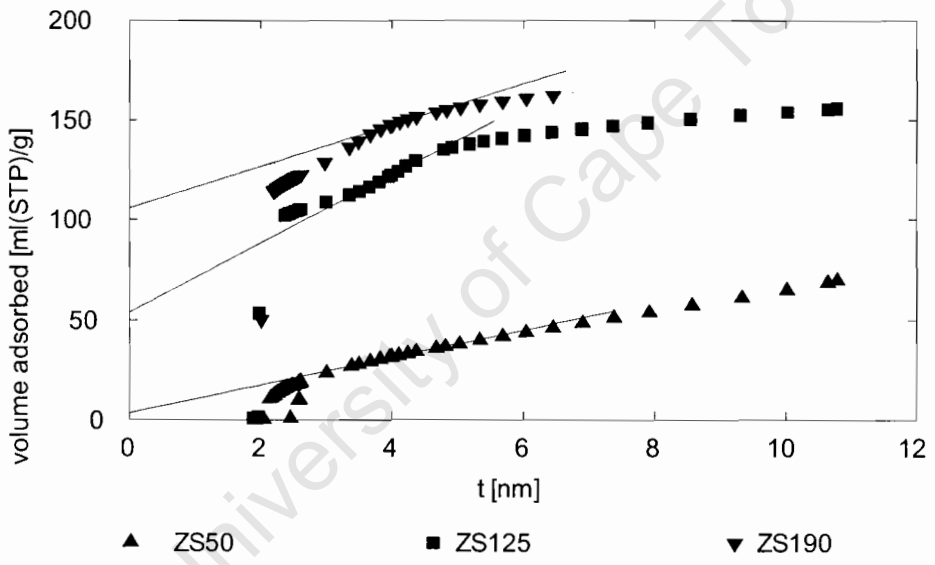

Figure 4.5: Harkins and Jura t-plot analysis of ZS50, ZS125 and ZS190. Solid lines:3.5<t<5, Dotted lines: t>5.0

4.2 Analysis of reaction data

4.2.1 Activity of the prepared catalysts

The conversion as a function of residence time inside the reactor is shown in Figures 4.6, 4.7 and 4.8. for different reaction temperatures for each sample synthesized at different temperatures. In all cases conversion increases with increasing synthesis temperature for all reaction temperatures. At a reaction temperature of 250 °C no conversion was observed for the amorphous material, ZS50. These results also indicate that the activity (as measured by the conversion at constant residence time) of the catalyst can be grouped into 3 broad classes according to synthesis temperature: (i) Low activity, $T_{synthesis} = 50$ °C, (ii) Medium activity, $T_{synthesis} = 100$ - 125 °C, (iii) High activity, $T_{synthesis} = 150$ - 190 °C. These three classes are consistent across all reaction temperatures, with the grouping becoming more defined as the reaction temperature increases. Figure 4.9 shows that as expected the activity (or conversion) increases with increasing temperature indicating consistency across all experiments with respect to flow rate and temperature. These results thus provide an indication of the reactivity of the prepared samples.

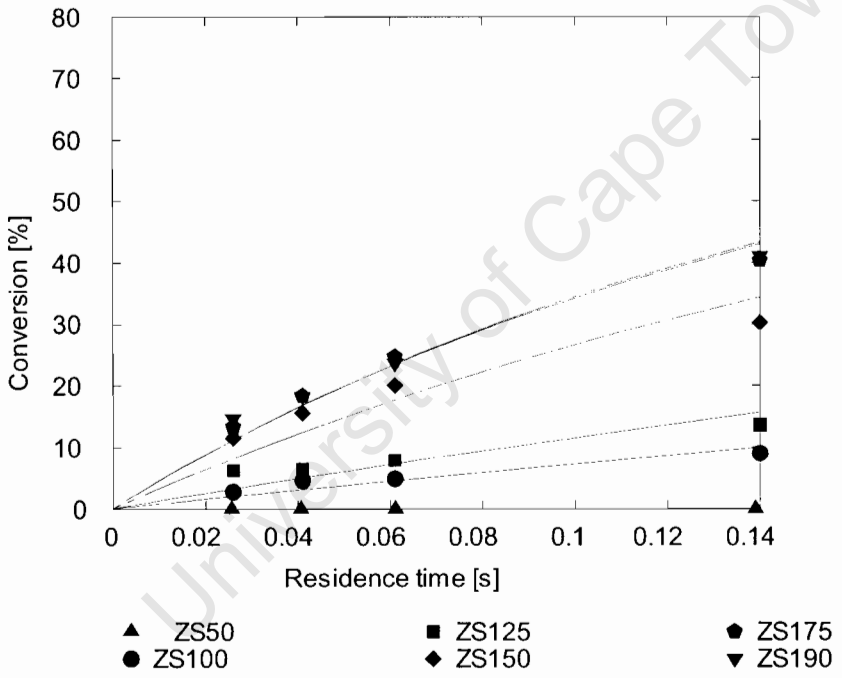

Figure 4.6: Conversion vs residence time at 250 °C. Lines represent the model fit.

4.2.2 Selectivity of the prepared catalysts

The plots of yield vs conversion as shown in Figures 4.10, 4.11 and 4.12 are a good indication of whether selectivity depends on synthesis temperature. Results show that the selectivity is independent of catalyst preparation temperature at all reaction temperatures studied in this work. In order to investigate subleties not observable in a yield-conversion plot, the mole ratio of *meta*-xylene:*ortho*-xylene as a function of conversion is shown in Figure 4.13. The results show that there is no trend with catalyst preparation temperature, in particular at high reaction temperatures, where the *meta*-xylene:*ortho*-xylene mole ratio was approximately constant with conversion for all catalysts. Figure 4.13(a) shows

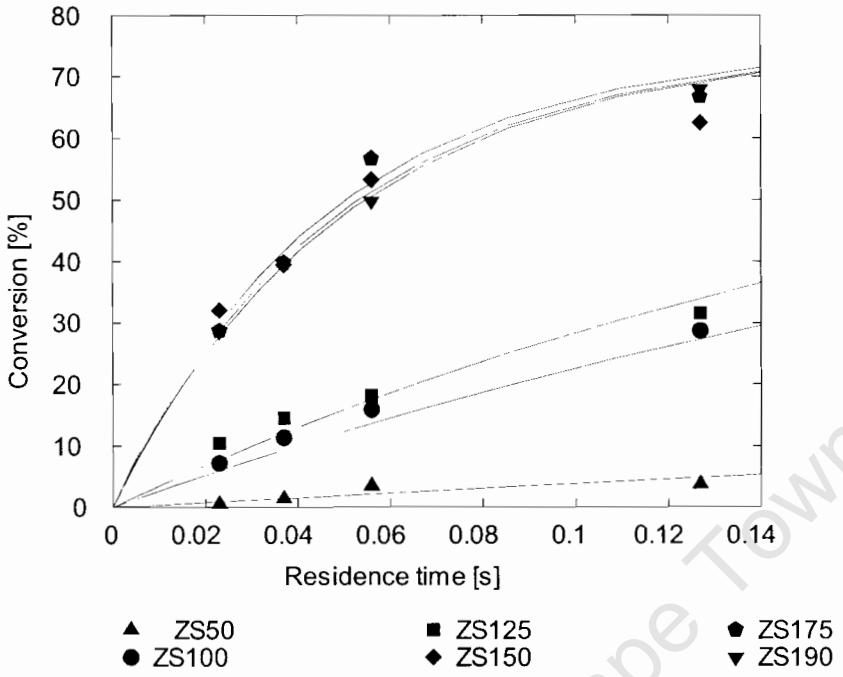

Figure 4.7: Conversion vs residence time at $300°C$. Lines represent model fits

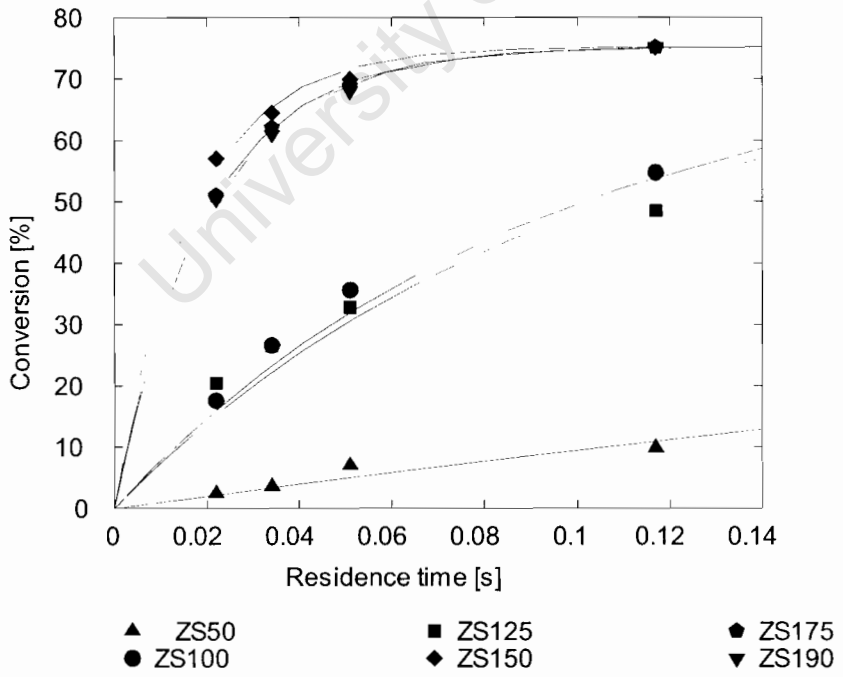

Figure 4.8: Conversion vs residence time at $350°C$. Lines represent model fits

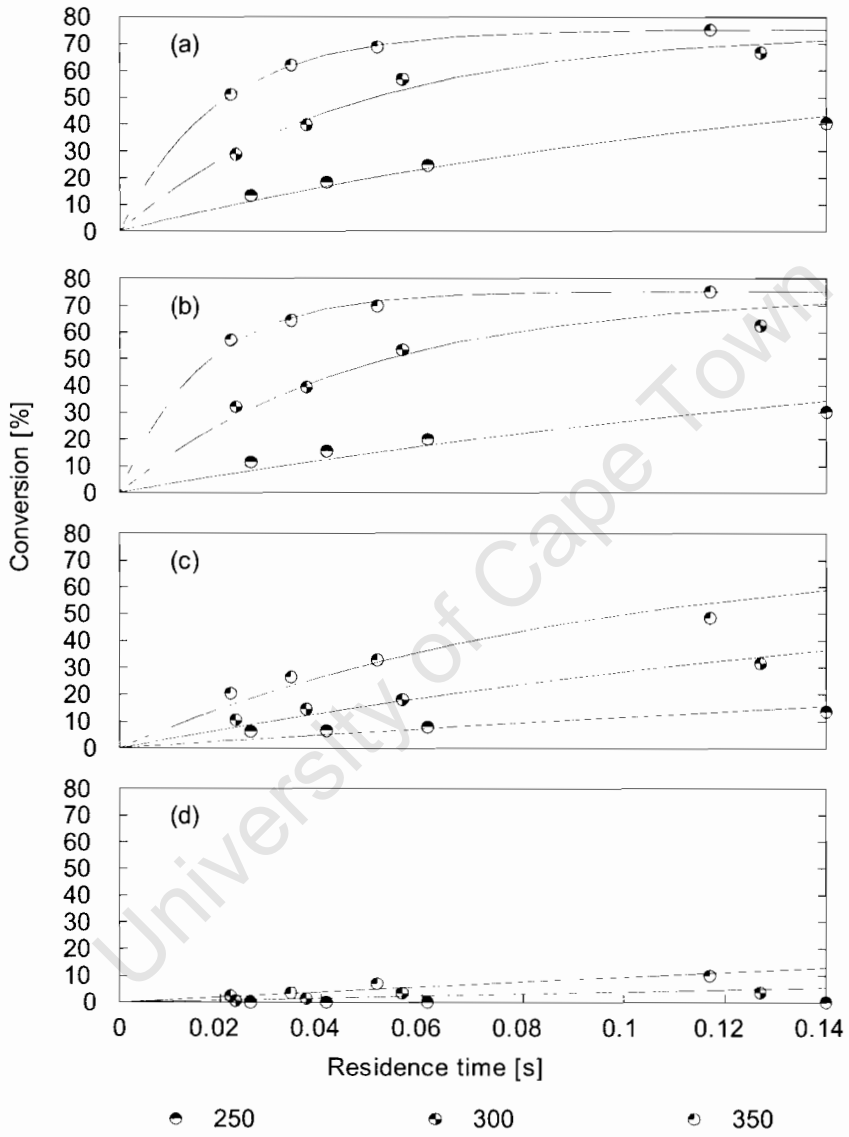

Figure 4.9: Conversion vs residence time at different temperatures for sample (a) ZS175, (b) ZS150 and (c) ZS125 and (d) ZS50. Lines represent model fits

considerable scatter, and this is a result of the magnification of experimental error when ratios of the yields are taken. The reduction in the scatter with increasing temperature is a result of the higher yields, which make the GC analysis more accurate. Notwithstanding the scatter, there is a statistically significant decrease in the *meta*-xylene:*ortho*-xylene ratio with increasing reaction temperature. This is not as a result of the changing equilibrium constant with temperature which yields a *meta*-xylene:*ortho*-xylene ratio of approximately 2.2 over the entire reaction temperature range. Thus for all these catalysts it would be expected that the *meta*-xylene:*ortho*-xylene ratio should be independent of temperature, if there are no diffusion limitations.

From Figure 3.3, decreasing *meta*-xylene:*ortho*-xylene mole ratio indicates that selectivity is influenced by diffusion limitations. This effect is particularly prevalent at low conversions, as observed in the results. These results show that this behavior is a global phenomena when averaged across all samples at a particular reaction temperature. Figure 4.14 investigates the influence of reaction temperature on the *meta*-xylene:*ortho*-xylene mole ratio with respect to catalysts prepared at different synthesis temperatures. When the model is used for extrapolation, results seem to suggest that the catalysts prepared at low synthesis temperatures have higher *meta*-xylene:*ortho*-xylene mole ratios i.e. less diffusion limitations, than those prepared at high synthesis temperatures. However, the model seems to have a large deviation from the experimental data at low conversions, and this conclusion must remain speculative.

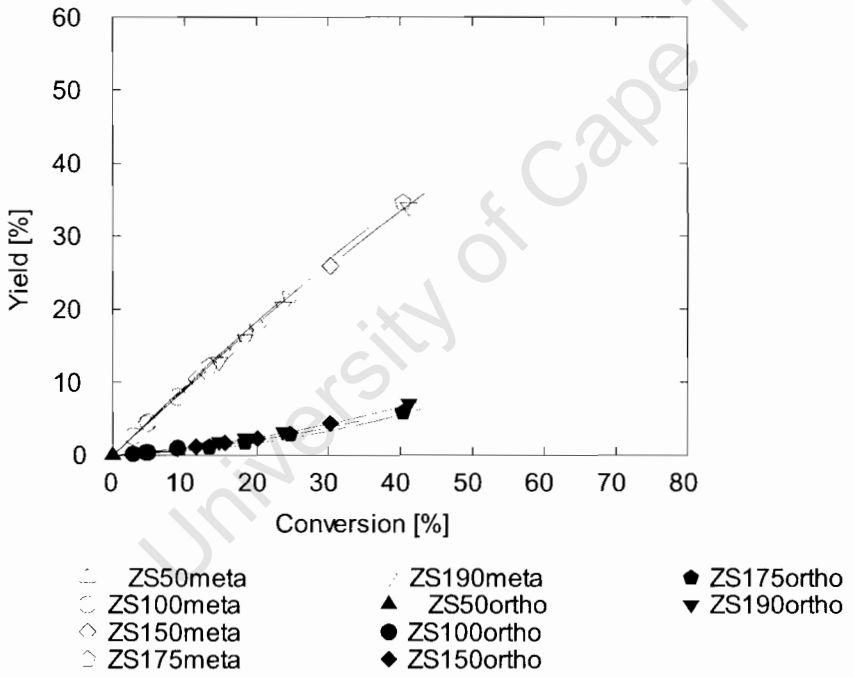

Figure 4.10: Yield of meta and ortho xylene vs conversion at 250 $^{\circ}C$. Lines represent model fits

4.2.3 Model parameter estimation

Figure 4.15 and 4.16 show that the model is able to predict the raw experimental data satisfactorily. Such data fitting was carried out on all experimental data to yield the intrinsic reaction rate constant, $k_p x$, and the diffusion time constant $\frac{D_{px}}{R^2}$ shown in Table 4.3. The intrinsic rate constant increases both

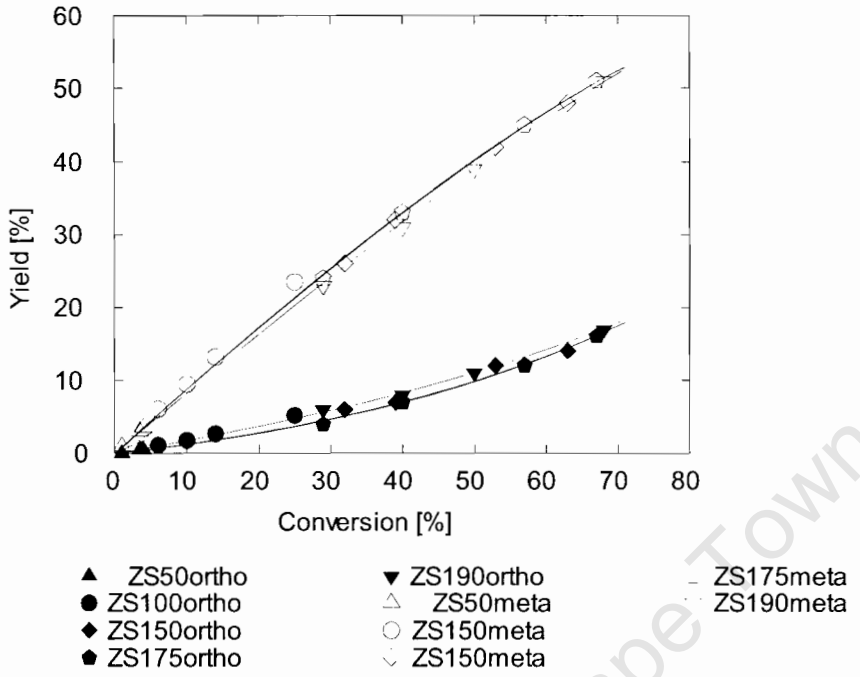

Figure 4.11: Yield of meta and ortho xylene vs conversion at 300 $^{\circ}C$. Lines represent model fits

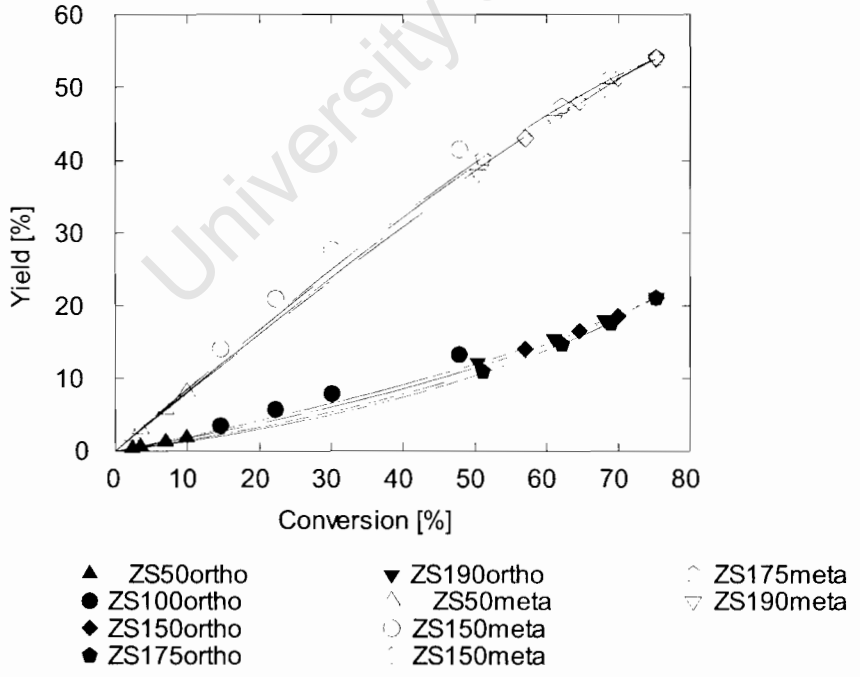

Figure 4.12: Yield of meta and ortho xylene vs conversion at 350 $^{\circ}C$. Lines represent model fits

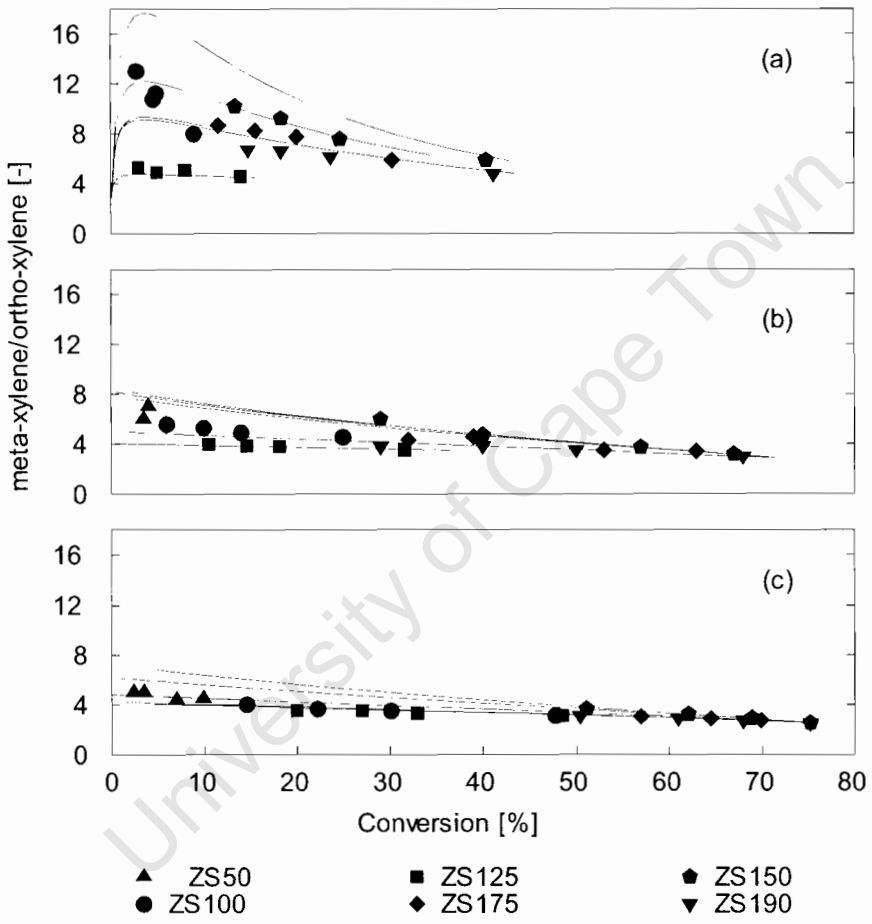

Figure 4.13: Meta to ortho xylene mole ratio vs conversion at temperatures of a) 250, b) 300 and c) 350 $^{\circ}C$. Lines represent model fits

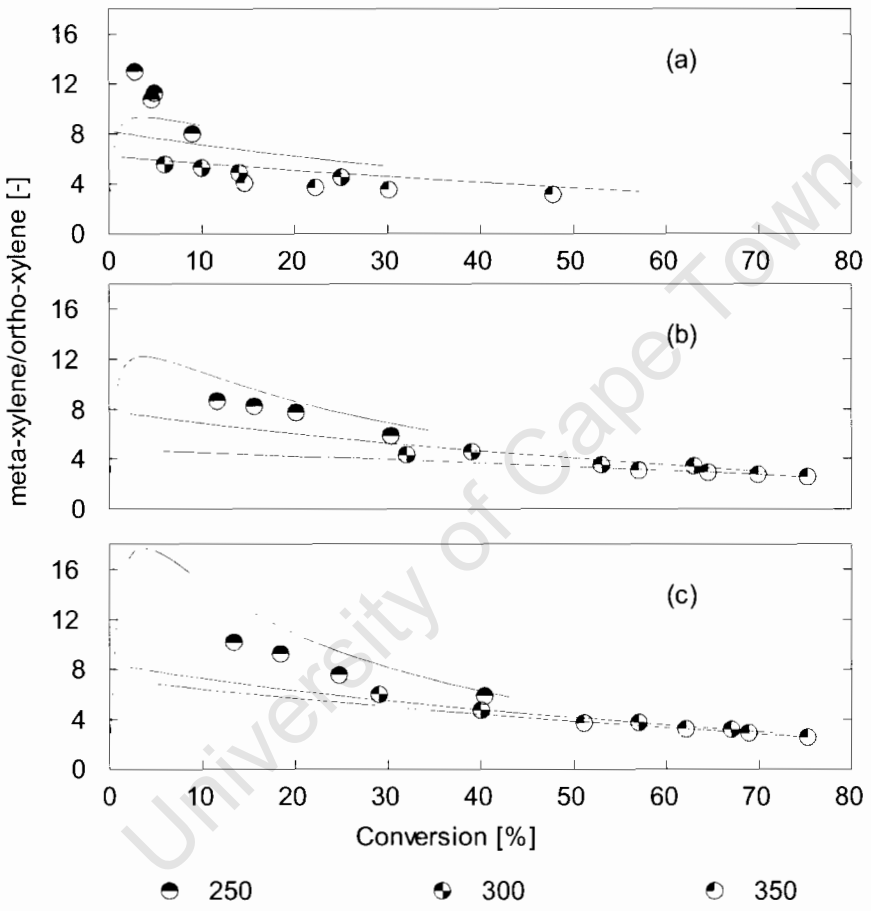

Figure 4.14: Meta to ortho ratio vs conversion at different temperatures for a) ZS100, b) ZS150 and c) ZS175. Lines represent model fits

with increasing reaction temperature and increasing synthesis temperature, as observed from Figures 4.6, 4.7 and 4.8. The variance in the rate constant in all cases was less than 17 %, which was acceptable given the scatter in the experimental data. However, the diffusion time constant $D_p x/R^2$ has a variance between 10 - 100 % making these data unreliable. Furthermore the values of $\frac{D_{px}}{R^2}$ are in all cases some 2 orders of magnitude greater than $k_p x$ indicating diffusion is much faster than reaction and hence cannot be limiting. This is confirmed by the first order Thiele modulus ϕ_{px} which in all cases was less than 0.05.

Although ϕ_{px} only provides an approximation to the Thiele modulus, first order reaction theory indicates that diffusion limitations are negligible for ϕ_{px} <1.0. Nevertheless it should be borne in mind that the pseudo Thiele modulus of *meta*-xylene, ϕ_{mx}, and *ortho*-xylene ϕ_{ox}, will be 33 and 10 times larger than ϕ_{px} (i.e. by a factor $\sqrt{D_{mx}}$ and $\sqrt{D_{ox}}$). Even for this case the Thiele modulus remains less than approximately 1.0, indicating that diffusion limitations in these samples can be neglected. A consequence of this is that the diffusion time constant $\frac{D_{px}}{R^2}$ presented in Table 4.3 is thus meaningless. Further manipulation to obtain D_{px} using an inaccurate radius R, although presented, is not justified. These results thus indicate that to all intensive purposes, none of the samples are diffusion limited and that the speculative hypothesis in this work is not justified.

The activation energy can be evaluated from an Arrhenius plot as show in Figure 4.17 by using equation 4.1. Results indicate that there are again 3 groups of data, as observed previously from the yield conversion plots (Figures 4.10, 4.11 and 4.12).

$$k_{px} = A \cdot \exp\left(\frac{-E}{RT}\right) \tag{4.1}$$

However, Table 4.4 shows that other than for sample ZS50, there does not seem to be a trend in the pre-exponential factor (entropy term) or the activation energy (reaction barrier). Considering that the low temperature data for ZS50 might be in error, would reduce the activation energy for ZS50 to approximately 60 kJ/mol with a corresponding pre-exponential factor with an order of magnitude of 10^5. Thus all activation energies lie between 50 and 70 kJ/mol, a rather large variation, but without any discernible trend with catalyst synthesis temperature. The activation energy might be considered rather low for intrinsic kinetics. However, it should be borne in mind that the rate constant actually represents a combination of linear adsorption and intrinsic kinetics (equation 4.2).

$$k_{px} = k_{int} K_{ads} \tag{4.2}$$

The heat of adsorption, ΔH_{ads}, is exothermic, and thus K_{ads} decreases with an increase in temperature, in contrast to k_{int}. Thus the true activation energy for the reaction excluding the adsorption correction would be given by equation 4.3.

$$E_{true} = E + \Delta H_{ads} \tag{4.3}$$

Table 4.3: Kinetic constants

Temperature $^{\circ}C$	**Catalyst**	$\mathbf{k_{px}} = \mathbf{2k}_{mx}$ $[s^{-1}]$	$\mathbf{D_{px}/R^2}$ $[s^{-1}]$	**2R** μm	$\mathbf{D_{px}}$ $[m^2s^{-1}]$ 10^{-08}	ϕ^{**}	$\sum Error^2$ 10^{-03}
250	ZS50	0.06 ± 0.00		-	-		
	ZS100	0.8 ± 0.08	1381 ± 1117	0.2-1	0.002	0.024±0.42	0.81
	ZS125	1.4 ± 0.20	1038 ± 576	0.2-1	0.002	0.037±0.17	2.80
	ZS150	3.5 ± 0.40	8647 ± 1077	0.1-0.5	0.053	0.020±0.34	7.8
	ZS175	4.8 ± 0.20	19890 ± 1924	0.2-1	0.008	0.014±0.75	2.61
	ZS190	5.0 ± 0.20	8306 ± 4099	<0.5	0.002	0.025±1.70	3.31
300	ZS50	0.2 ± 0.01	452 ± 436		-	0.030±0.15	0.46
	ZS100	3.0 ± 0.16	3739 ± 1328	0.2-1	0.011	0.028±0.59	1.37
	ZS125	4.3 ± 0.30	2394 ± 687	0.2-1	0.007	0.042±0.12	3.35
	ZS150	17.0 ± 1.4	20900 ± 1307	0.1-0.5	0.128	0.029±0.30	9.98
	ZS175	18.4 ± 1.0	23600 ± 1158	0.2-1	0.036	0.028±0.97	5.51
	ZS190	17.7 ± 0.3	12690 ± 1184	<0.5	0.016	0.037±0.04	4.60
350	ZS50	1.2 ± 0.1	821 ± 330		-	0.038±0.29	8.80
	ZS100	8.8 ± 0.55	8117 ± 3104	0.2-1	0.001	0.033±1.67	5.09
	ZS125	9.4 ± 0.88	5796 ± 2287	0.2-1	0.012	0.041±1.64	1.04
	ZS150	53.7 ± 1.88	37080 ±8074	0.1-0.5	0.036	0.038±0.19	1.10
	ZS175	43.7 ± 0.39	47890 ± 3658	0.2-1	0.014	0.030±0.06	9.33
	ZS190	44.3 ± 0.67	25580 ± 1828	<0.5	0.012	0.042±0.92	2.48

$^{**}\phi_{px}$ Thiele modulus (dimensionless)
±Absolute error

Table 4.4: Pre-exponential factors and activation energy for the intrinsic rate constant

Catalyst	Pre-exponential factor (A) $[s^{-1}]$	Activation energy (E) [kJ/mol]
ZS50	$5.9 \cdot 10^8 (10^5)$	100(61)
ZS100	$2.2 \cdot 10^6$	64
ZS125	$1.5 \cdot 10^5$	50
ZS150	$3.0 \cdot 10^7$	68
ZS175	$1.6 \cdot 10^6$	54
ZS190	$2.2 \cdot 10^6$	56

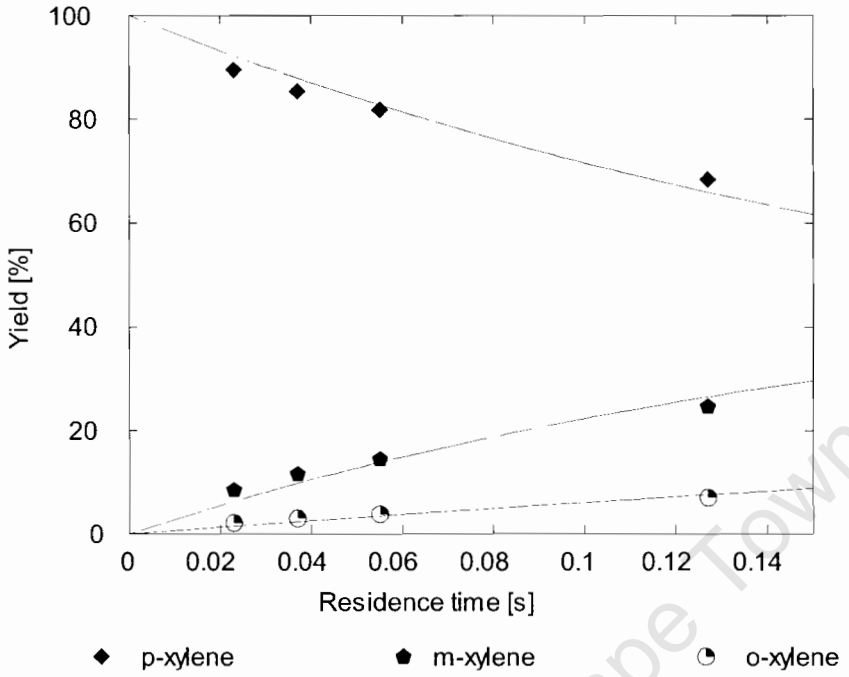

Figure 4.15: Yield vs residence time for ZS125 at 300 °C.Lines represent model fits

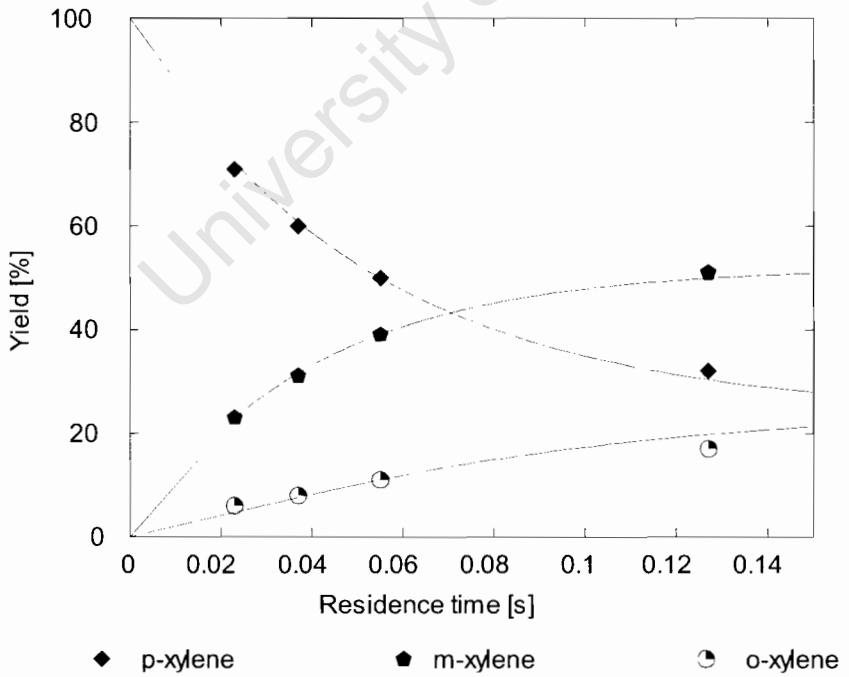

Figure 4.16: Yield vs residence time fit for ZS190 at 300 °C.Lines represent model fits

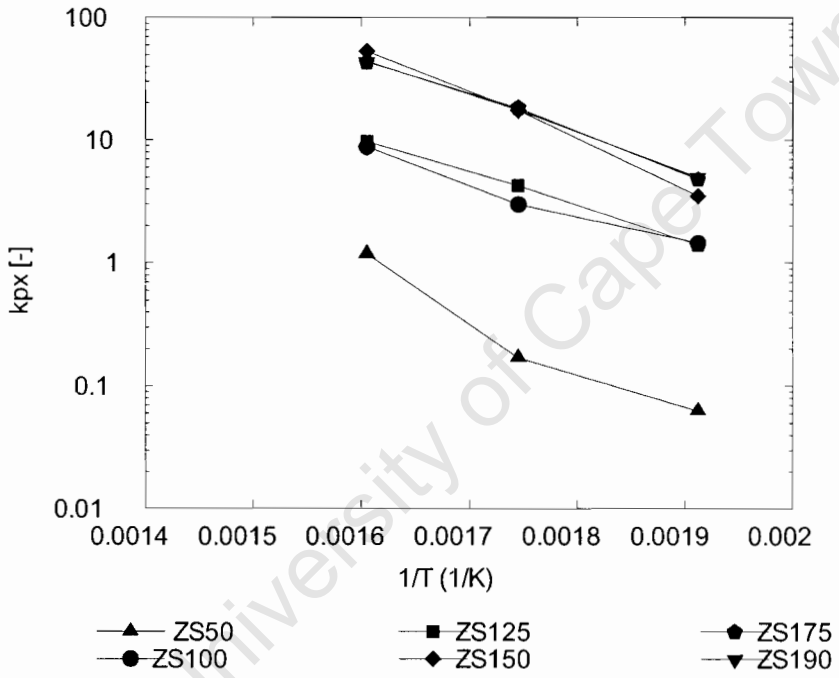

Figure 4.17: Arrhenius plot

Chapter 5

DISCUSSION

5.1 Catalyst characterisation

As observed by Nicolaides [1999] and others, the surface area of a catalyst plays a significant role in the observed activity of the catalyst. Increasing surface area leads to an increase in activity [Costas et al., 2001]. In order to identify the factors with regard to morphology which might be leading to the observed increase in activity with increasing crystallinity, suitable characterisation techniques were used to measure properties such as total surface area and micropore volume.

Figure 5.1 shows that the total surface area (A_{BET}) and micropore surface area (A_{micro}) increase with increasing crystallinity. In contrast the external surface area ($A_{external}$) goes through a maximum at a crystallinity of ca. 50 (i.e. sample ZS100). External surface area comprises of the macro- and mesopores. These are formed within amorphous material and by agglomeration of small zeolite crystals. Except for ZS50 and ZS190 which show a larger deviation in crystal size from the other samples, the SEM (Figures 4.2(a)-(f)) characterisation does not support these observations. The trend observed in the surface areas can be related to the observed changes in crystal morphology with crystal growth [Grieken et al., 2000] see [section 1.3]. Ignoring ZS50 and ZS190, external surface area shows a steady decrease with increasing crystallinity without a change in the total surface area. This indicates that the amorphous material is being converted into zeolitic material without a change in crystal size. The ZS50 outlier, is a result of the large amorphous agglomerate particles which have significantly reduced macropore volume (thus area) in comparison to small crystals. The Z190 outlier is a result of the agglomeration of very small zeolite crystals which have very high external surface areas notwithstanding their high crystallinity.

Figure 5.2 shows that the relative contribution of the micropore area to the total area increases from ca. 10 to 70 % with increasing crystallinity. Previous work [Röeger et al., 2001], Manstein et al, 2002] has shown that for typical ZSM-5, the external surface area can contribute between 20-30 % towards the total surface area. In contrast, carefully prepared ZSM-5 crystals have external surface areas which contribute less than 5 % to the total suface area [Zhiqiang at al., 2004]. The kinetic reaction analysis carried out on these results estimates the first order rate constant per volume of catalyst (section 3.3):

- The first order rate constant used here, is a global rate constant and not distinguished between internal and external acid sites.

Figure 5.3 shows that the micropore volume increases with increasing crystallinity. Generally, the micropores contain the strong acid sites which are responsible for most of the reaction activity [Nicolaides et

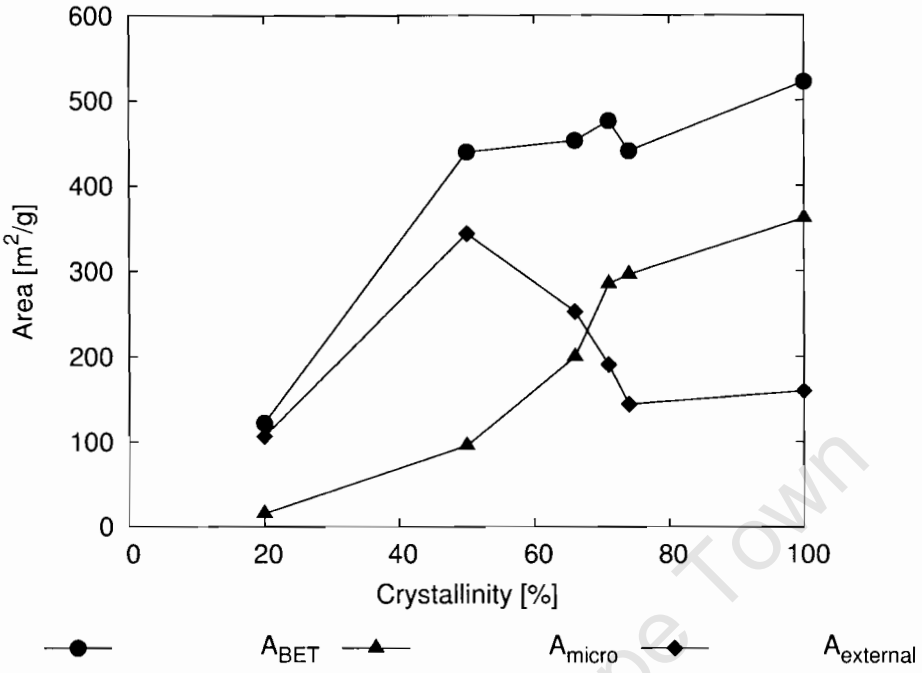

Figure 5.1: Micro, BET and external areas vs crystallinity

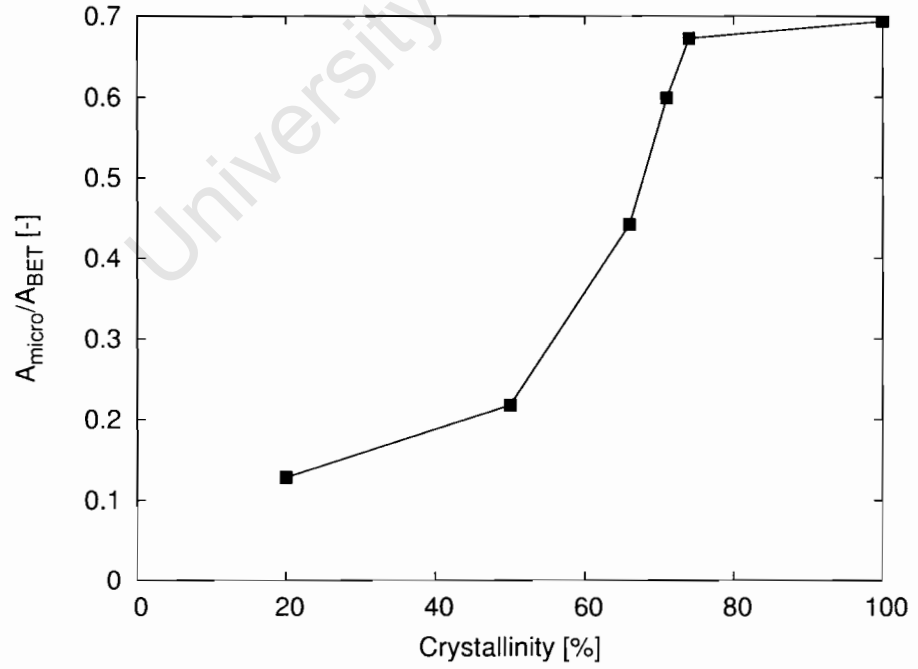

Figure 5.2: Micro area/BET area vs crystallinity

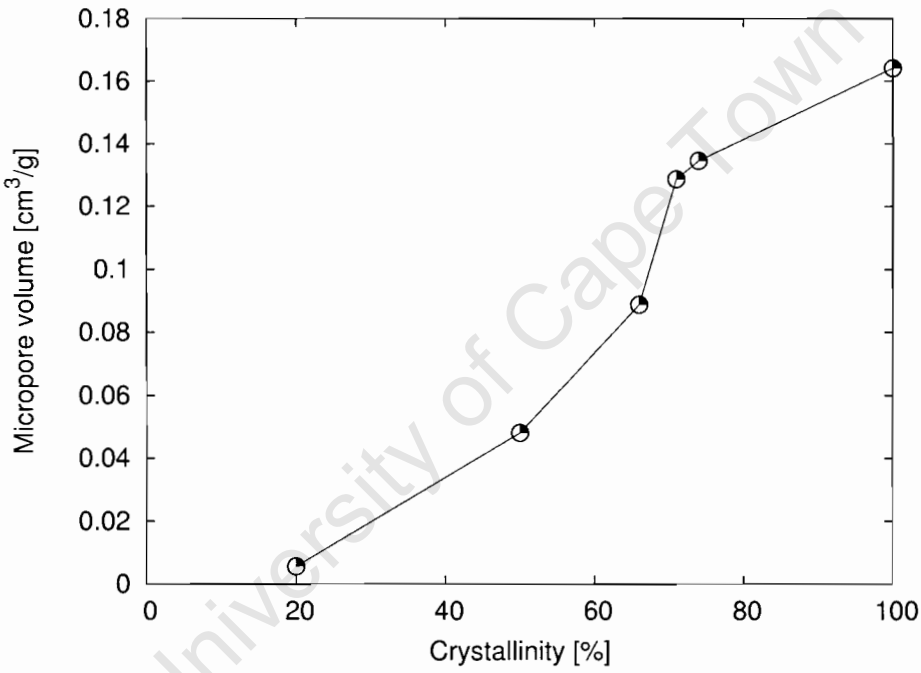

Figure 5.3: Micropore volume vs crystallinity

al., 2002], thus it is natural to expect an increase in activity with an increase in micropore volume, and hence also an increase with crystallinity. However, some of the strong acid sites will also be present on the external surface of the zeolite crystals. *Para*-xylene isomerisation is a fast reversible reaction which forms bulky products which might be subject to diffusion limitations within the zeolite pores. Thus, under zeolite diffusion limited conditions the contribution of the external surface to the total reaction rate can be significant and non-*para*-selective [Roeger et al., 2001], [Manstein et al., 2002]. The diffusion limitations are also strongly related to the zeolite crystal size and to the temperature at which the reaction is carried out. Thus the change of activity with micropore volume (and/or crystallinity) could be distorted due to the influence of the external activity.

5.2 Analysis of reaction data

The catalytic reaction data were analysed using a reaction-diffusion model to rigorously account for the effect of diffusion on the activity and selectivity [Figure 3.2]. The influence of the external surface activity was not explicitly taken into account in the reaction-diffusion model and any effects of the external surface will reflect on both the activity and selectivity. However, the external surface is not selective and any influence of diffusion limitations on the reaction behaviour must be as a result of the diffusion limitations within the micropores. If the results are not influenced by diffusion limitations, then there is no way of separating the external activity from the micropore activity and the rate constant represents a lumped coefficient. In the previous chapter it was shown that it was not possible to obtain reliable estimates of the diffusion coefficients and that to all intensive purposes the reaction was not limited by diffusion at all the temperatures and catalysts studied [see Table 4.3]. Thus the rate constant used in the following analysis does not distinguish between contributions from both the external and micropore active sites.

Figure 5.4 shows clearly that the conversion increases as the crystallinity increases for all catalyst samples. This trend is consistent with increasing temperature and residence time. However, these results do not provide any clue as to the part of the catalyst that may be responsible for the activity. Based on the model analysis, there are two obvious choices in which to look for a correlation of activity.

1. It can be assumed that the zeolite micro-pores are responsible for the total activity. Then a plot of conversion vs micropore volume (X vs V_{micro}) should yield a consistent trend.

2. Alternatively it can be assumed that all the available surface area is active and has equal activity. Then a plot of conversion vs BET surface area (X vs A_{BET}) should yield a simple trend.

However, these trends are distorted by two phenomena. Firstly, the conversion is only proportional to the activity at low conversion (typically below 10 %) and irreversible reactions. The conversion in most instances exceeded 10 %. Secondly, the conversion in some cases was very close to equilibrium. Under these conditions an increase in activity can no longer be observed experimentally as the conversion can no longer increase.

Thus for these data it is necessary to resort to a reaction-diffusion model such that the intrinsic first order rate constants can be evaluated. The first order rate constants (k_{pX}), a characteristic property of the catalyst, depends only on reaction temperature and is independent of the operating conditions of the reaction system. However, a decision needs to be made to whether this rate constant is proportional to the % crystallinity, A_{BET} or V_{micro}. Figure 5.5 shows that the first order rate constant (k_{pX}) increases with increasing % crystallinity. All the rate constants appear to have a rapid increase between 60 - 80 % crystallinity, before and after which there seems to be very little change. The dashed trend line can be represented by equation 5.1

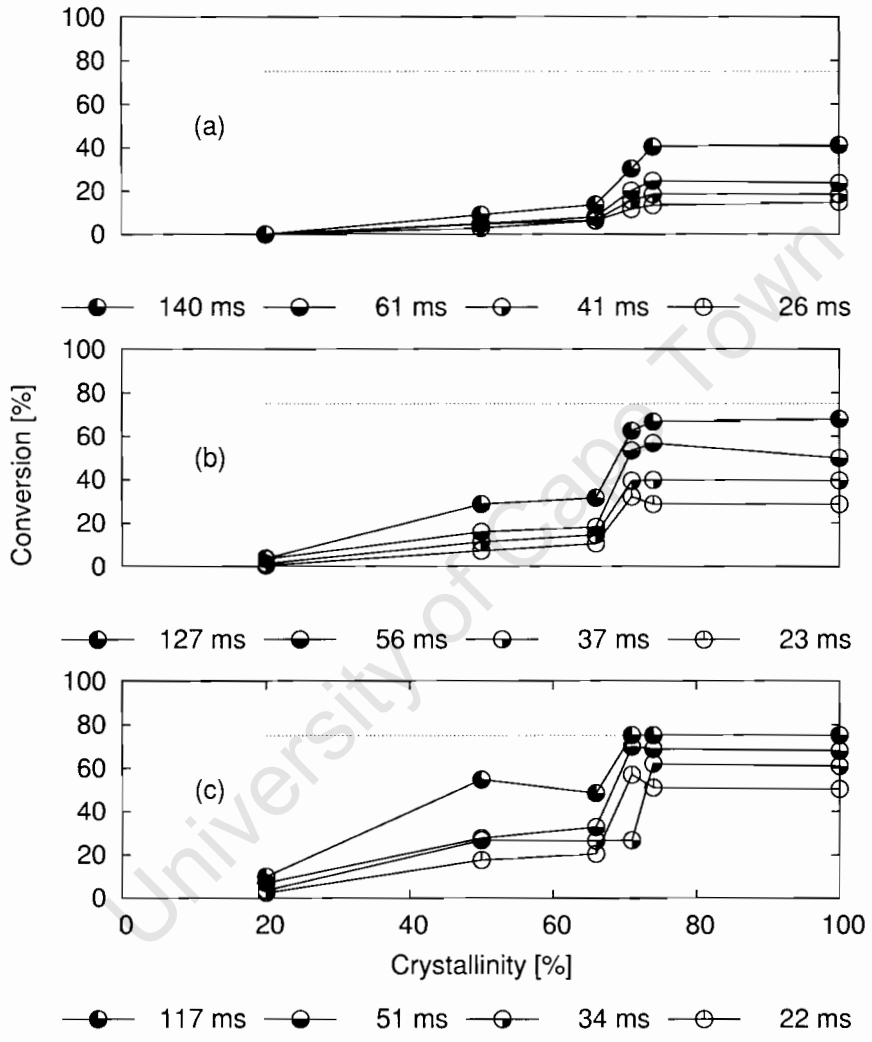

Figure 5.4: Conversion vs crystallinity at (a) 250 $^{\circ}C$, (b) 300 $^{\circ}C$ and (c) 350 $^{\circ}C$. Dotted line represents equilibrium conversion. The legend represents the residence time based on catalyst volume in milliseconds.

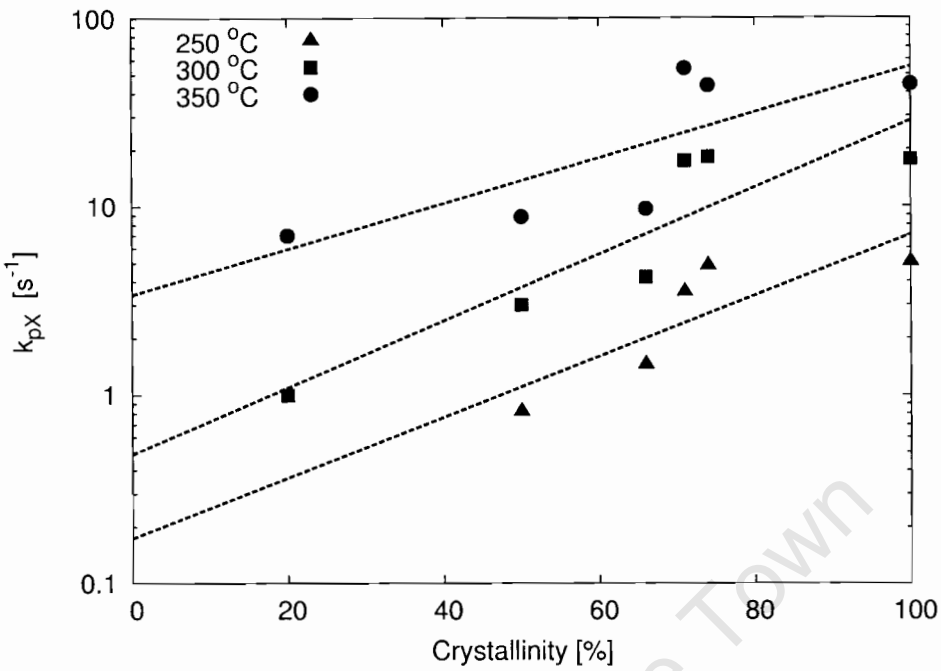

Figure 5.5: Kinetic constants vs crystallinity at different temperatures

$$k_{pX} = \alpha \exp(\beta\omega) \tag{5.1}$$

where ω represents either % crystallinity, A_{BET} or V_{micro} and α, β are regression constants. It is clear from Figure 5.5 that the correlation of the activities with crystallinity is not as good as might be expected. Figure 5.6 shows that the correlation with the BET surface area (A_{BET}) is considerably poorer than in the case of crystallinity, with ZS50 activity deviating significantly from the trend. Furthermore, zero surface area would imply zero activity, a behaviour that is not predicted by equation 5.1. However, in support of the trend line, the activity at zero surface area appears to be negligibly small. Lastly, Figure 5.7 shows that the correlation with micro-pore volume (V_{micro}) appears better than the above two correlations. However, the ZS50 data seems consistently to deviate strongly from the trend predicted by equation 5.1 in all cases. The constants used in equation 5.1 for the trend line given in Figure 5.7 are given in Table 5.1. It thus seems that the micropore volume provides the best correlation of catalyst activity. However, the rate constant k_{pX} represents the overall activity of the catalyst, as there are no diffusion limitations. The activity of the catalyst can be separated into two contributions (i) activity of the external surface and (ii) activity from the micropores. The intercept of the trend line, α, can be viewed as the amorphous catalyst activity of the external surface, and this has an activation energy of approximately 60 kJ/mol. The slope of the trend line can be viewed as the contribution of the micropore volume to the total activity of the catalyst. The slope of all the trend lines are approximately the same, indicating that the contribution of the micropore volume to the total activity is independent of temperature. This is also the reason that the activation energy of 60 kJ/mol between the α 's represents the average activation energy of the individual rate constants for each catalyst.

Table 5.1: Activity correlation constants for equation 1 with ω=V_{micro}

temperature [$°C$]	α	β
250	0.344	17.6
300	1.19	18.4
350	3.29	17.8

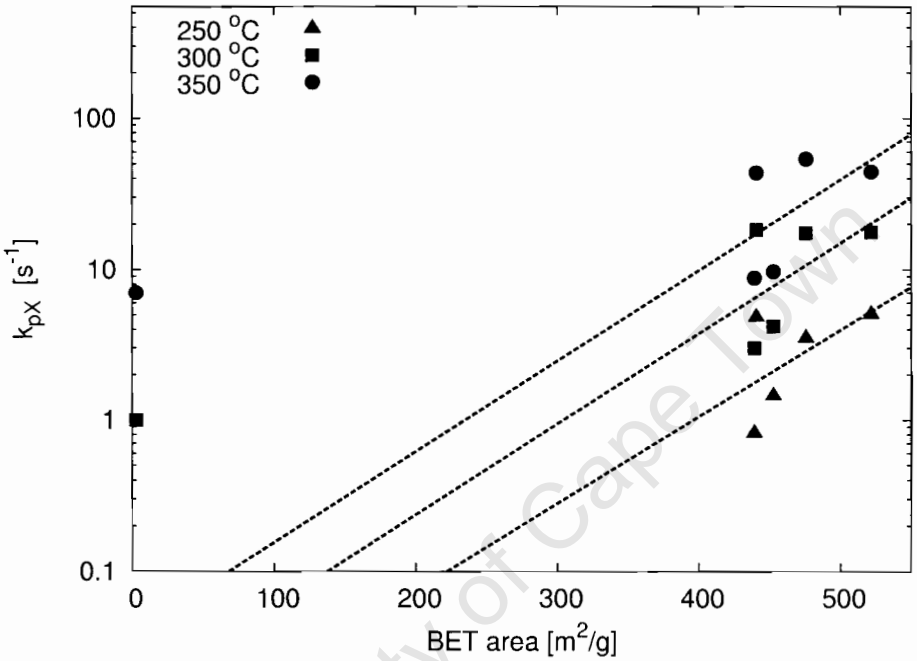

Figure 5.6: Kinetic constants vs BET area at different temperatures

Although the correlation seems to work, there is some concern that the activity increases exponentially with increasing micropore volume. A seeming more logical behaviour would have been to increase linearly with increasing micropore volume, similar to making a physical mixture of purely amorphous and purely microporous material. Figure 5.1 shows that the external surface area goes through a maximum with increasing micropore volume. This has not been accounted for in the above correlation (equation 5.1). If the amorphous catalyst activity is attributed to the external surface, this activity would vary with micropore volume and thus the intercept of the above correlation would depend on the external surface area. However, if it was assumed that the rate constants of ZS50 are representative of the amorphous catalyst activity, then except at 250 $°C$, their contribution to the overall rate constant is negligible.

Although the analysis of the results in chapter 4 has indicated that diffusion has no influence on the results, this conclusion is based in the premise that the model is an accurate representation of the reaction system. It still seems of interest to quantify the behaviour of the experimental selectivity with respect to catalyst properties and to relate these observations to the behaviour predicted by the theoretical reaction-diffusion model (Figure 3.2 and 3.3 in theory section). Figure 5.8 shows that the *meta:ortho* xylene ratio goes through a maximum at intermediate crystallinities at constant conversion. The constant conversion analysis was achieved by using the model to extrapolate to the 20 and 30 % conversion where neccessary. A high *meta:ortho* xylene ratio indicates low diffusion limitations. This does not seem to be consistent with the physical characterisation, which shows that these catalysts (ZS150) appears to have the largest zeolite crystal size and hence should have the largest diffusion limitations. On the other

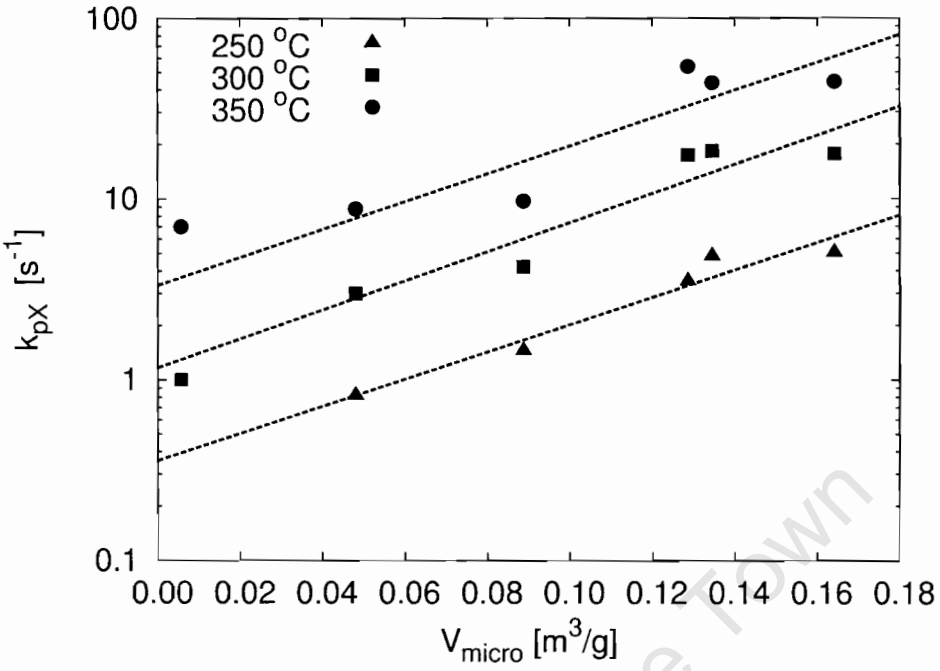

Figure 5.7: Kinetic constants vs micro-volume at different temperatures

hand, ZS190 has the smallest crystals and thus should have the smallest diffusion limitations and thus the highest *meta*:*ortho* xylene ratio, again inconsistent with the expected trend. The behaviour with increasing micropore volume as shown in Figure 5.9 shows a similar trend to that of the crystallinity, as expected. These results support the observations made in the results [Table 4.3] that diffusion limitations do not influence the *para*-xylene isomerisation reaction.

Thus is summary, these results have shown that the reaction rate increased with increasing crystallinity in contrast to the results observed by Nicolaides, and consistent with observations in other literature [Costas et al., 2001]. Furthermore, these results confirm the absence of any diffusion induced selectivity changes as a result of changing crystallinity. The differences between this work and that of Nicolaides may be explained as follows: Firstly, the reactions considered are different, and would have different behaviours making the work not immeditely comparable. The propane aromatization reaction is a much more complex reaction than the simple 1,2 methyl shift xylene reaction considered in this work. Secondly it is extremely difficult to reproducibly manufacture identical partially crystalline material and thus the samples used in both works could have sufficient difference to cause these deviations.

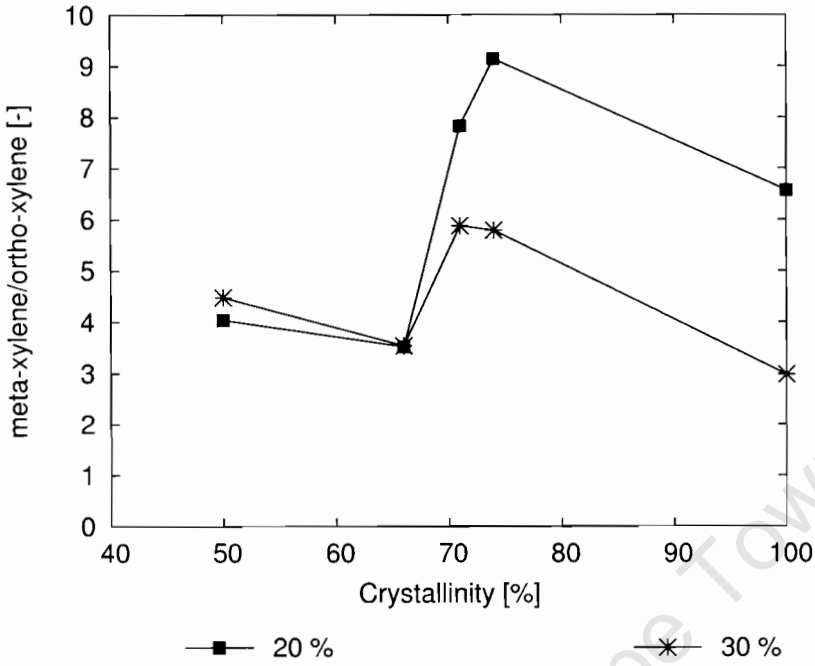

Figure 5.8: *Meta* to *ortho* ratio vs crystallinity at 20 and 30 % conversion

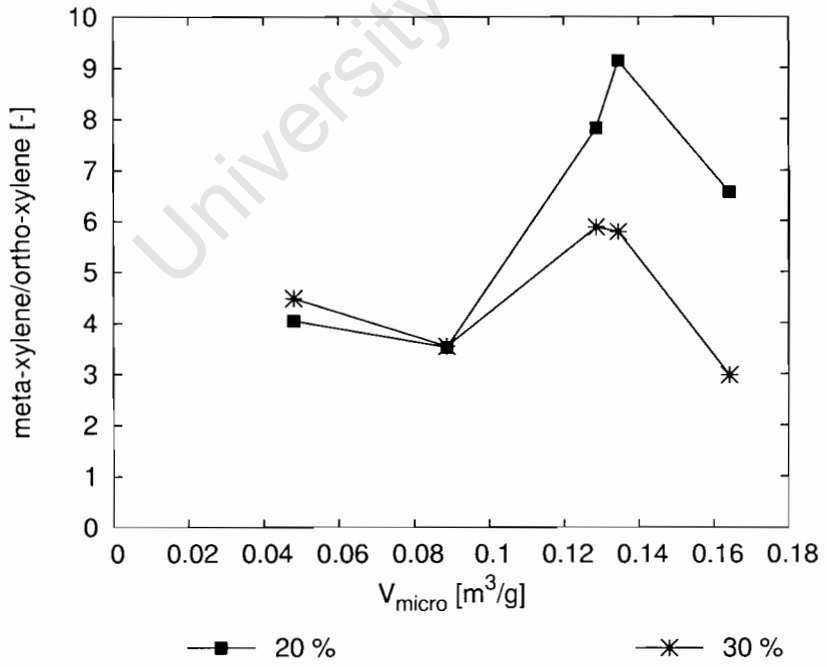

Figure 5.9: *Meta* to *ortho* ratio vs micro-volume at 20 and 30 % conversion

Chapter 6

CONCLUSIONS

1. Variation of synthesis temperature at constant synthesis times produced ZSM-5 of different morphologies.

2. Increasing synthesis temperature resulted in an increase in the % crystallinity, micropore volume and BET surface area, while the external surface area went through a maximum.

3. No diffusion limitations were observed under all reaction conditions for all catalyst samples. Both the model results and experimental data confirmed this observation.

4. The activity as represented by the first order rate constant and micropore volume increases with an increase in crystallinity.

5. The first order rate constant increased exponentially with the micropore volume of the catalysts. The micropore volume provided the most reasonable correlation for the first order rate constant.

Bibliography

Chang, N., Chen, C., Chu, S., Chen, P., and Chuang, T. (1989). Acidity effect of ZSM-5 zeolites on phenol methylation reaction. *Zeolites as catalysts*, 25:50–65.

Chen, N., Degnan, T., and Smith, C. (1994). *Molecular Transport and reaction in zeolites.* VCH Publishers.

Dejaifve, P., Auroux, A., Gravelle, P. C., and Vedrine, J. C. (1981). Methanol conversion on acidic ZSM-5, Offetite, and Mordenite Zeolites: A Comparative Study of the Formation and Stability of Coke Deposits. *Journal of catalysis*, 70:123–136.

Flanders, C., Tuan, V., Noble, R., and Falconer, J. (2000). Separation of C6 isomers by vapor permeation and pervaporation through ZSM-5 membranes. *Journal of Membrane Science*, 176:43–53.

Gola, A., Rebours, B., amd K. Lynch, E. M., Benazzi, E., Lacombe, S., Delevoye, L., and Fernandez, C. (2000). Effect of leaching agent in the dealumination of stabilized Y zeolites. *Microporous and Mesoporous Materials*, 40:73–83.

Grieken, R. V., Lotelo, J., Menendez, J., and Melero, J. (2000). Anomalous crystallization mechanism in the synthesis of nanocrystalline ZSM-5. *Microporous and Mesoporous Materials*, 39:135–147.

Guisnet, M., Gnep, N., and Morin, S. (2000). Mechanisms of xylene isomerization over acidic solid catalysts. *Microporous and Mesoporous Materials*, 35-36:47–59.

Guisnet, M. and Magnoux, P. (1989). Coking and Deactivation of Zeolites. *Applied Catalysis*, 54:1–27.

Karger, J. and Ruthven, D. (1992). *Diffusion in zeolites and other microporous solids.* John Wiley Sons, Inc., New York.

Manstein, H. (2001). The chemical vapour deposition of tetraethoxysilane on zeolite ZSM-5. *University of Cape Town.*

Masuda, T., Fufikata, Y., Mukai, S., and Hashimoto, K. (1998). Changes in catalytic activity of MFI-type zeolites caused by dealumination in a steam atmosphere. *Applied Catalysis*, 172:73–83.

Montes, A., Gabelica, Z., Rodriguez, A., and Giannetto, G. (1998). A new way to obtain acid or bifunctional catalysts. IV. Effect of calcination conditions on the catalytic properties of TPA, MeNH3-[Ga, Al]-ZSM-5 zeolites synthesized in the absence of inorganic cations. *Applied Catalysis*, 169:87–94.

Nicolaides, C. (1999). A novel family of solid acid catalysts: substantially amorphous or partially crystalline zeolitic materials. *Applied catalysis*, 185:211–217.

Nicolaides, C., Kung, H., Makgoba, N., Sincadu, N., and Scurrell, M. (2001). Characterization by ammonia adsorption microcalorimetry of substantially amorphous or partially crystalline ZSM-5 materials and correlation with catalytic activity. *Applied Catalysis.*

Nicolaides, C., Sincadu, N., and Scurrell, M. (2002). NAS (novel aluminolilicates) as catalysts for the aromatisation of propane. Studies of zinc and gallium modified zeolite-based systems having various extents of XRD crystallinity. *Applied Catalysis*, 223(429-435).

Roeger, H., Moller, K., and O'Connor, C. (1997). The transformation of 124-trimethylbenzene: a test reaction to monitor the external surface modifications of H-ZSM-5. *Microporous Materials*, 8(151).

Schumacher, R. and Karge, H. (1999). Adsorption kinetics study of the diethylbenzene isomers in MFI-type zeolites. *Microporous and Mesoporous Materials*, 30:307–314.

Sponer, J., Sponer, J., and Cejka, J. (2001). Ab initio quantum chemical study on the zeolite catalyzed transformations of para-xylene. *Molecular Structure*, 540:145–152.

Triantafyllidis, C., Vlessidis, A. G., Nalbandian, L., and Evmiridis, N. P. (2001). Effect of the degree and type of the dealumination method on the structural, compositional and acidic characteristics of H-ZSM-5 zeolites. *Microporous and Mesoporous Materials*, 47:369–388.

Trong, D., Lutic, D., and Kaliaguine, S. (2000). An example of mesostructured zeolitic material: UL-TS-1. *Microporous and Mesoporous Materials*, 44-45:435–444.

Zhiqiang, L., Ottaviani, M., Abrams, L., Lei, X., and Turro, N. (2004). Characterization of the external surface of silicalites employing electron paramagnetic resonance. *Physical Chemistry*, 108:8040–8047.

Appendix A

List of symbols

Si	Silicon
Al	Aluminium
FCC	Fluid Catalytic Craker
HPLC	High Pressure Liquid Chromatography
XRD	X-Ray Diffraction
SEM	Scanning Electron Microscopy
NH_3	Ammonia
EFAL	Extra Framework Aluminium
FAL	Framework Aluminium
N_2	Nitrogen
K	Kelvin
AHFS	Ammonium hexafluorosilicate
EDTA	Ethylenediaminetetraacetic acid
ϕ	Thiele Modulus
η	Effectiveness factor
TPA	Tetrapropylammonium
SiO_2	Fumed Silica
NaOH	Sodium Hydroxide

$AL(OH)_3$	Aluminium Hydroxide
BET	Branneur Emmet Teller
MFC	Mass Flow Controller
L	Length
R	Radius
c_i	Concentration of component $_i$
pX	Para-xylene
mX	Meta-xylene
oX	Ortho-xylene
k	Reaction constant
K	Equilibrium constant
F_i	Flow of species $_i$
$V_{zeolite}$	Volume of zeolite
Q	Volumetric flow
τ	Residence time of reactant species inside the zeolite pores
W_i	Molar flux of species $_i$
D_i	Diffusion coefficient for species $_i$
A	Area
x	Liqiud phase molar fraction
y	Gas phase molar fraction
r	Volume based reaction rate
X	Conversion

Appendix B

SEM images

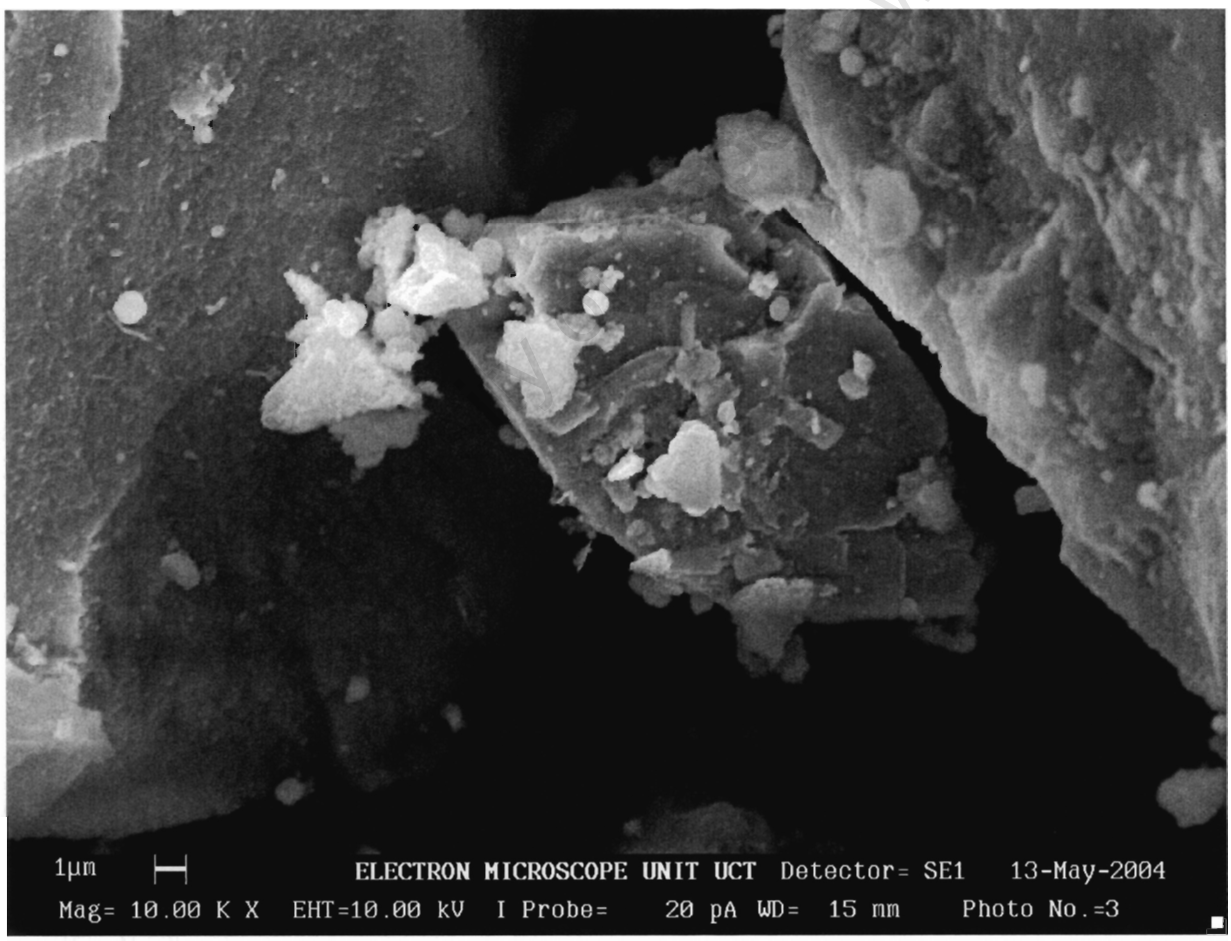

Figure B.1: Image for ZS50

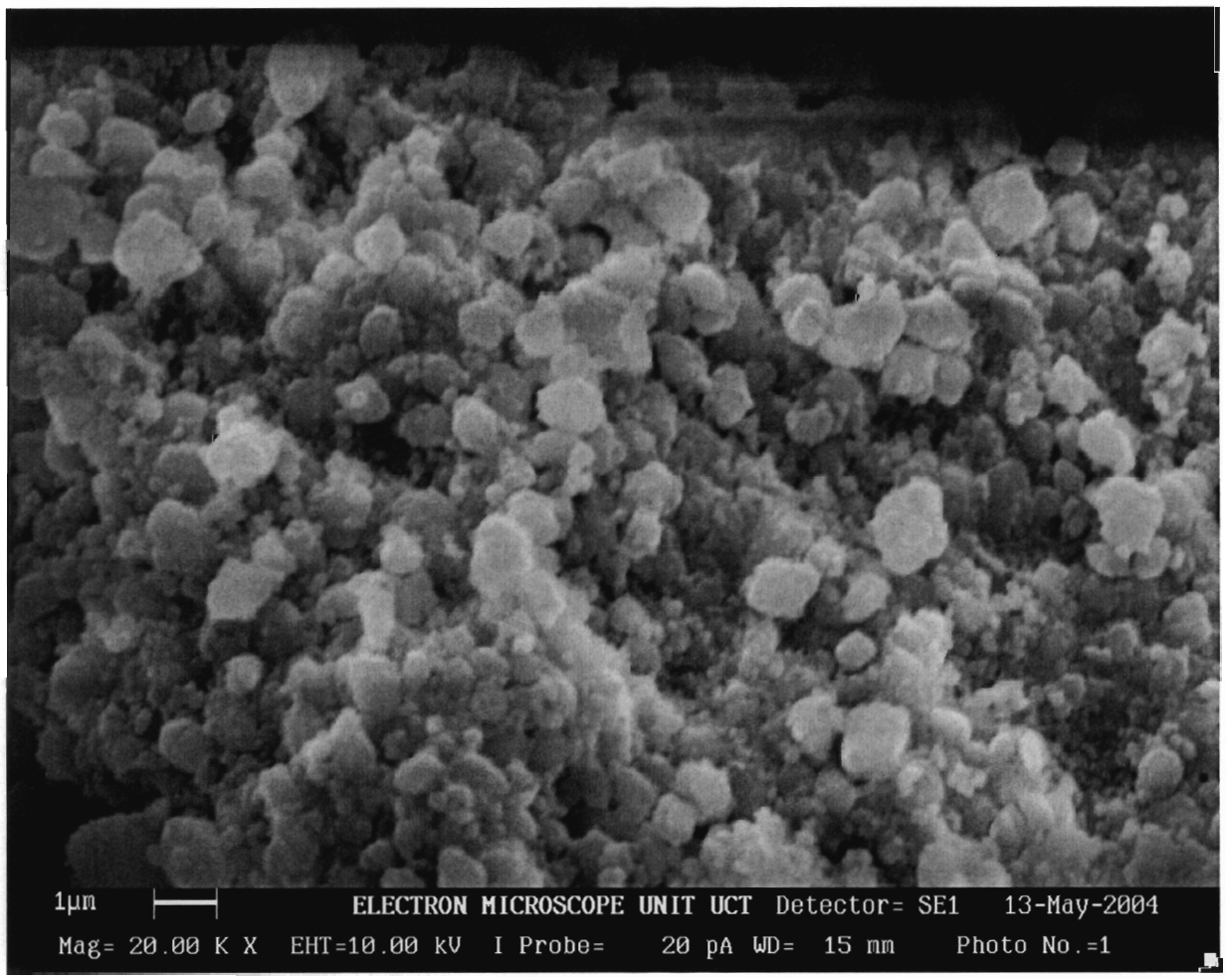

Figure B.2: Image for ZS100 with crystal size 0.5-1μm

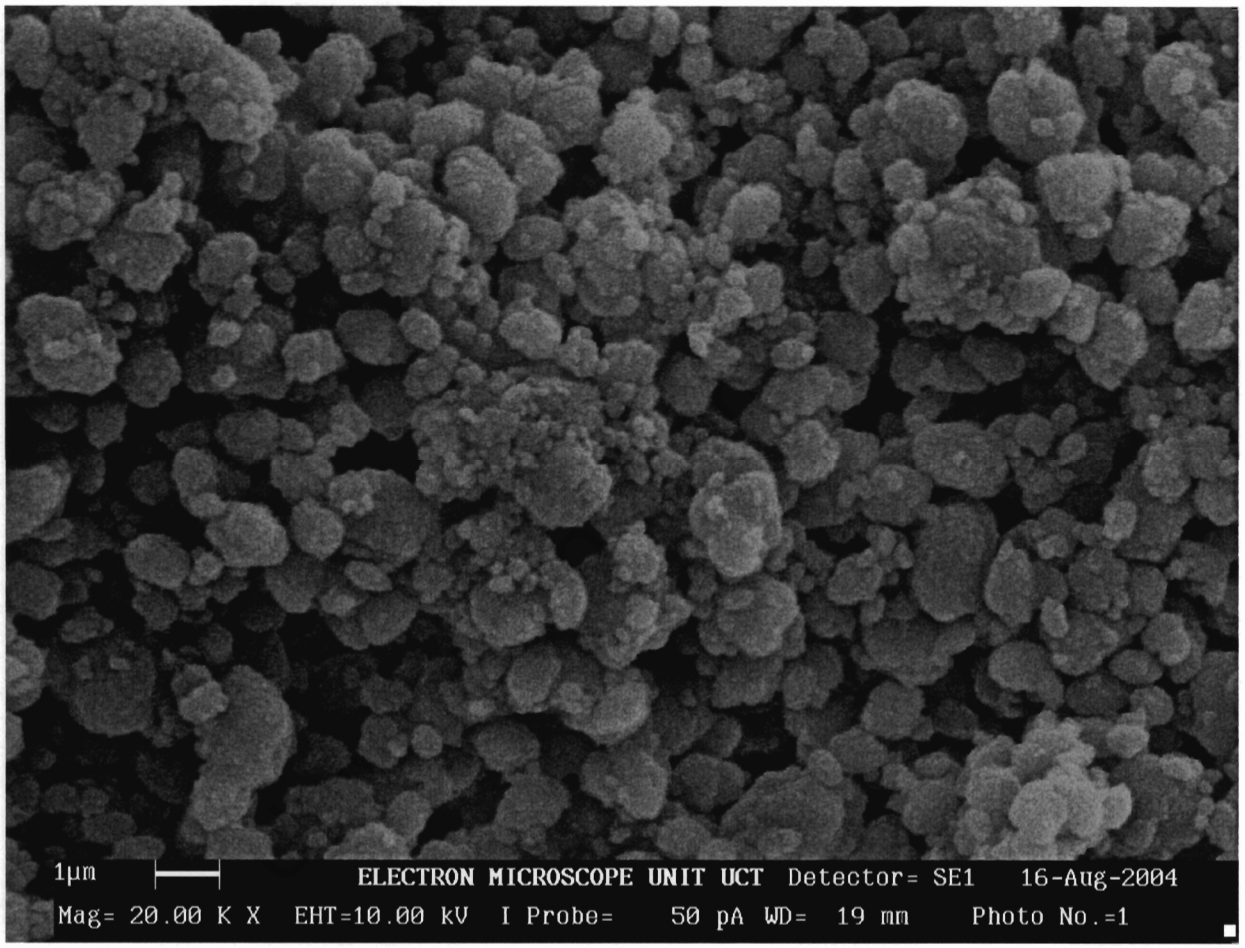

Figure B.3: Image for ZS125 with crystal size 0.2-2μm

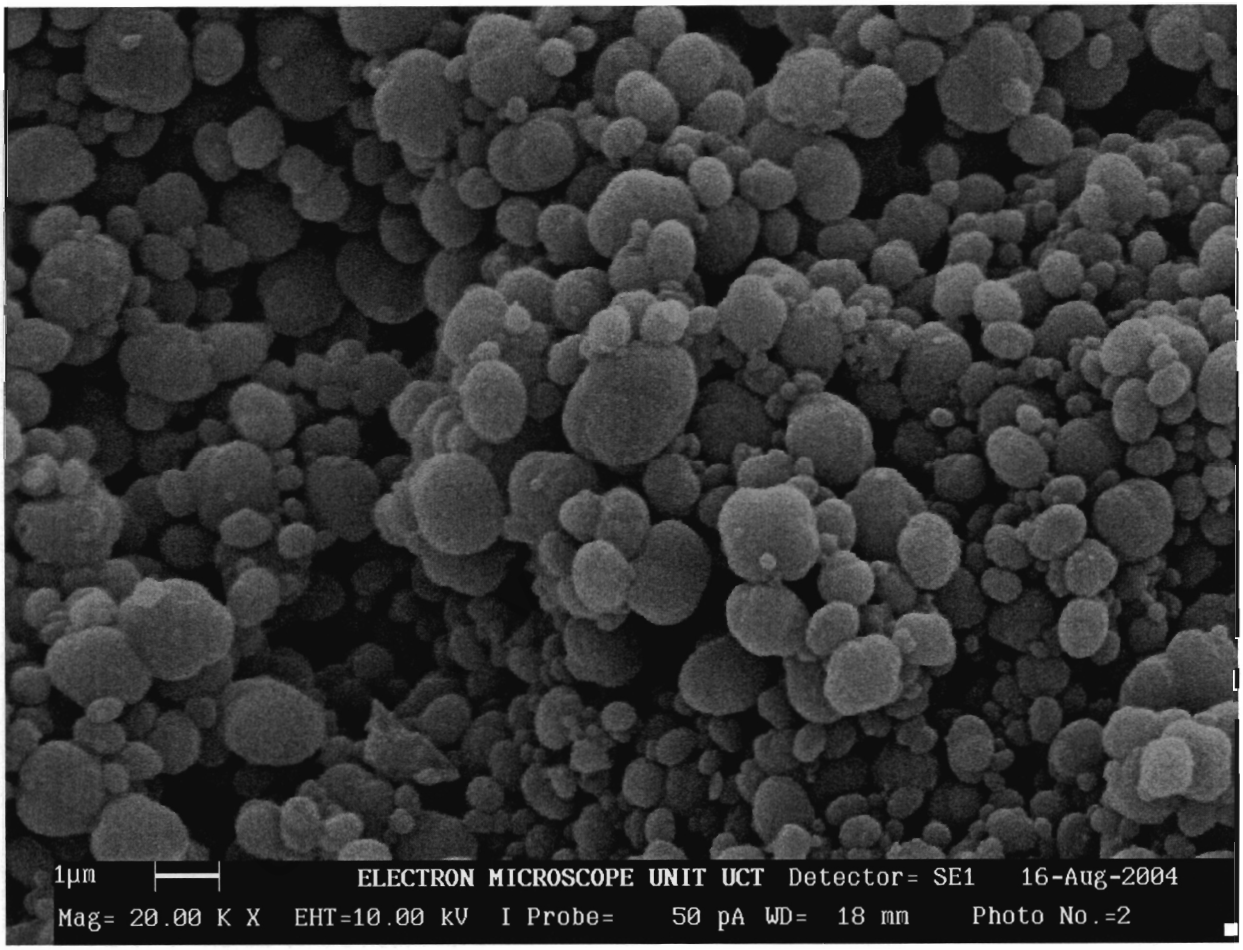

Figure B.4: Image for ZS150 with crystal size 0.2-2μm

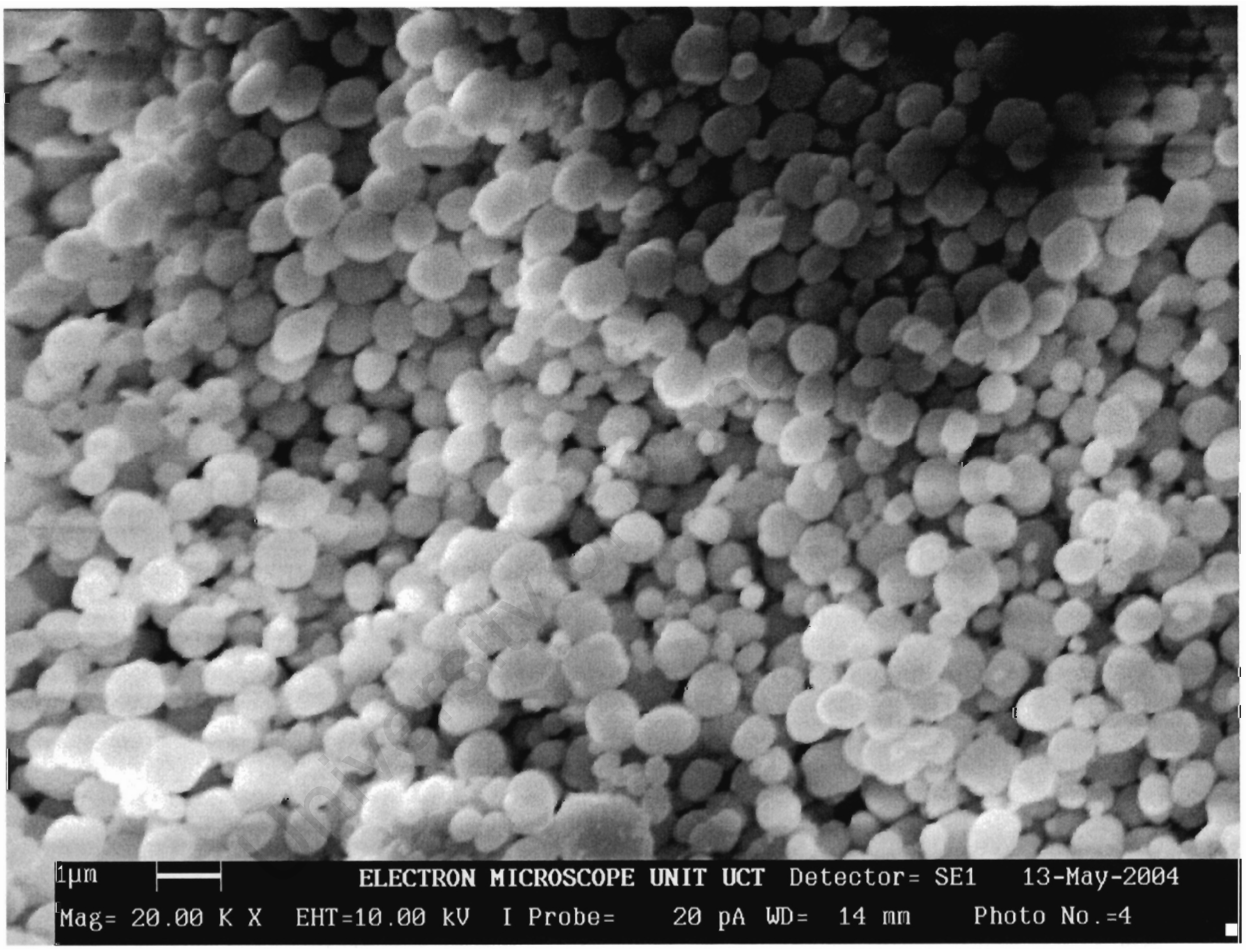

Figure B.5: Image for ZS175 with crystal sizes 0.2-1μm

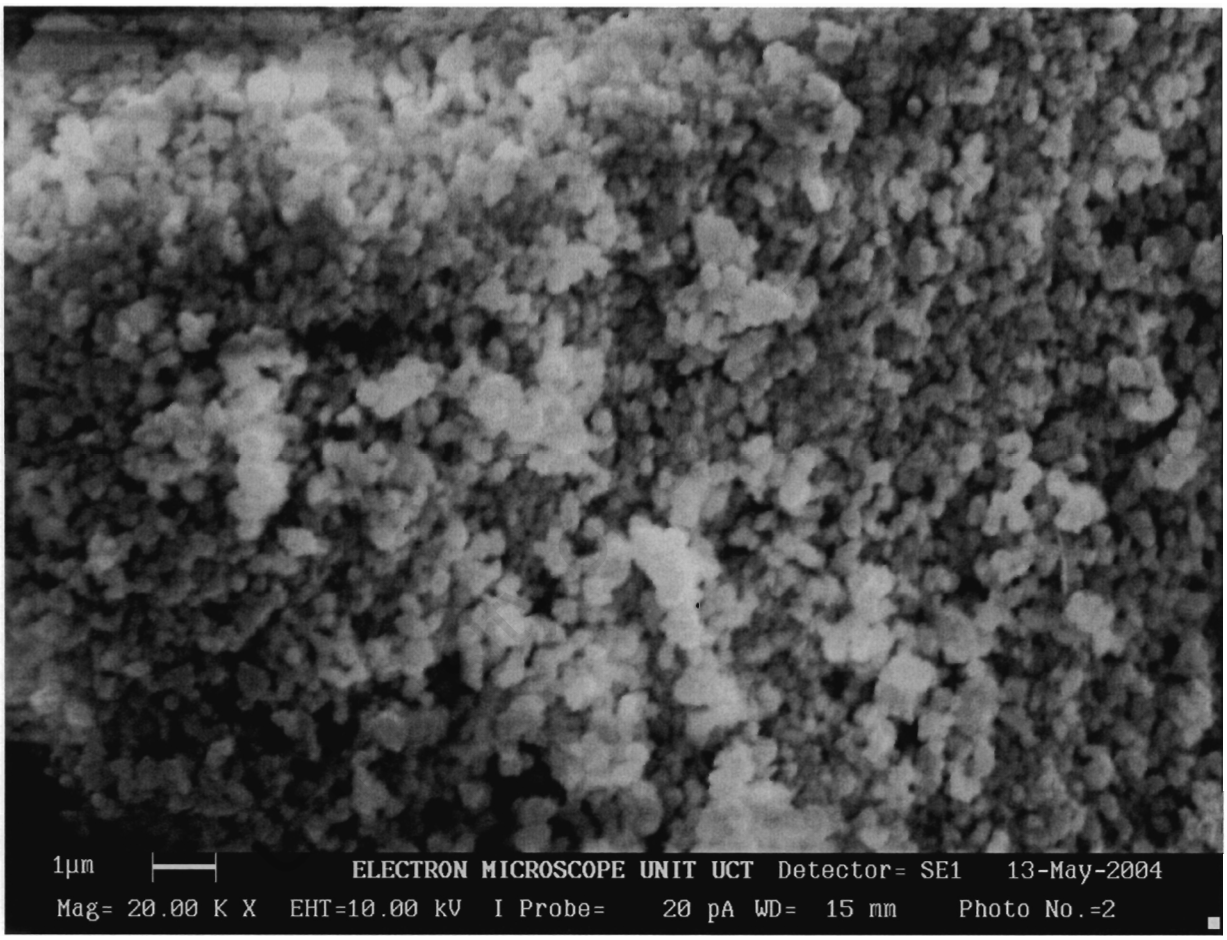

Figure B.6: Image for ZS190 with crystal size 0.2 μm

Appendix C

BET

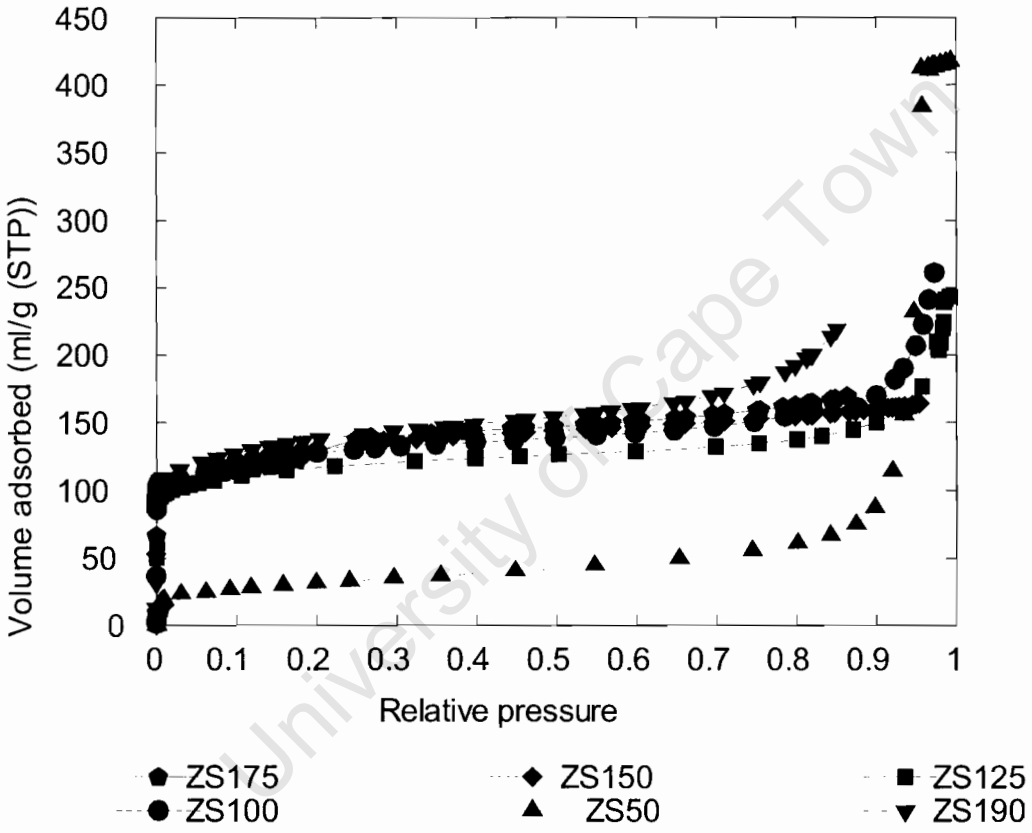

Figure C.1: BET plots for all samples

Appendix D

Model fitted data

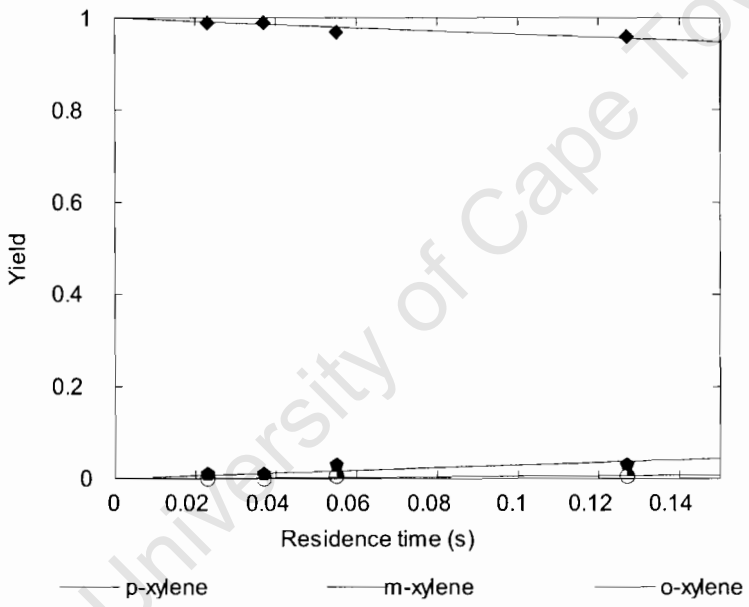

Figure D.1: Yield vs residence time for ZS50 at 300 $^{\circ}C$. Lines represent model fits.

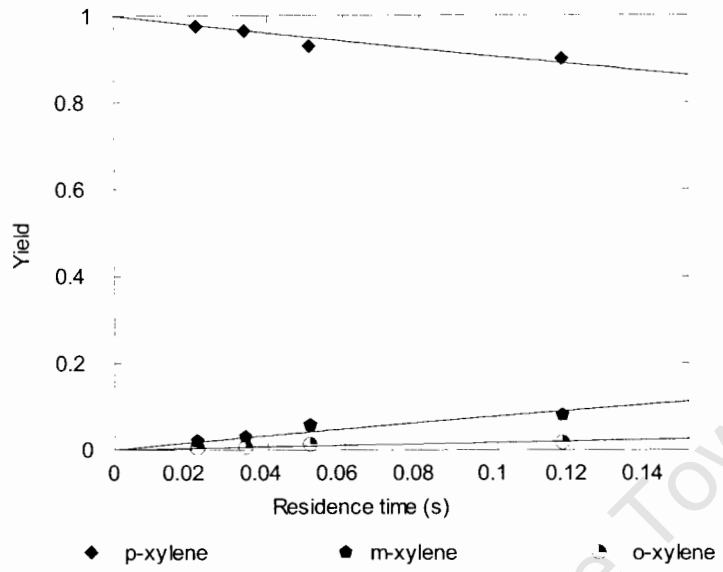

Figure D.2: Yield vs residence time for ZS50 at 350 $°C$. Lines represent model fits.

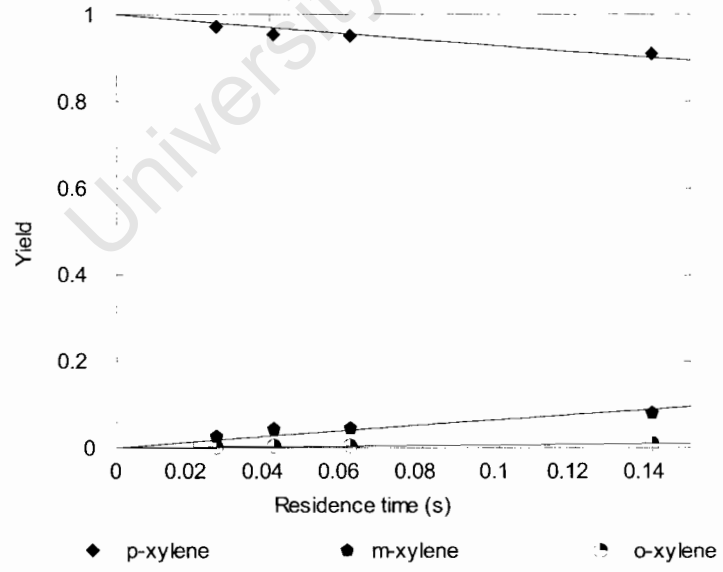

Figure D.3: Yield vs residence time at 250 $°C$ for ZS100. Lines represent model fits.

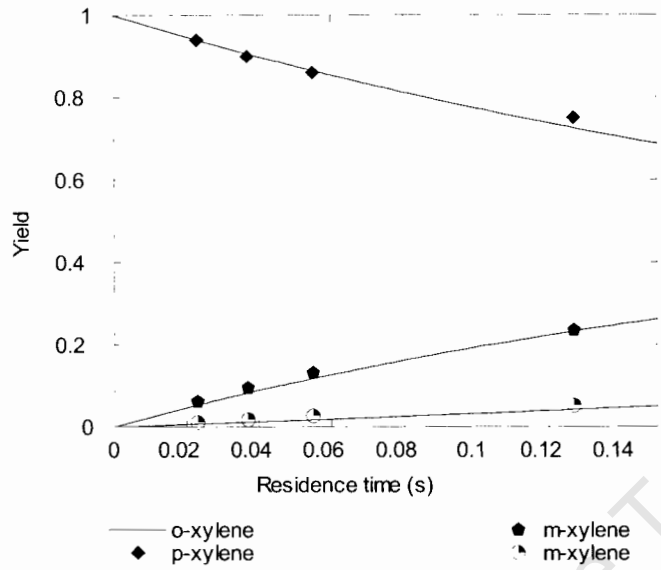

Figure D.4: Yield vs residence time at 300 $°C$ for ZS100. Lines represent model fits.

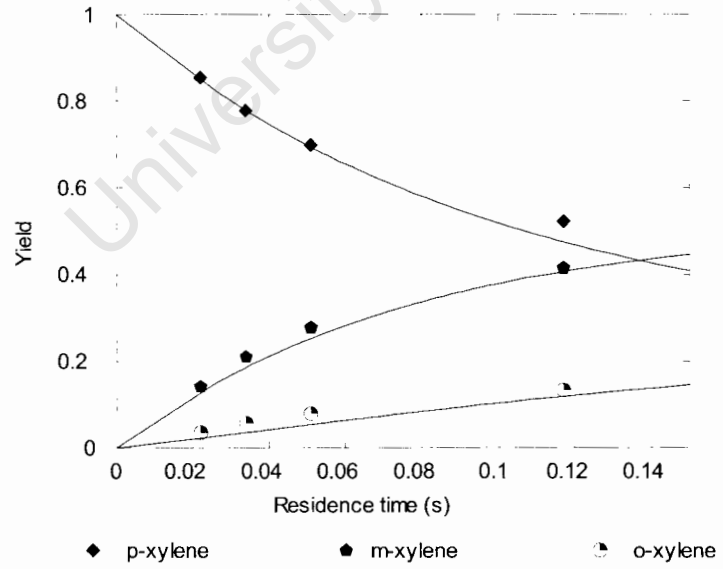

Figure D.5: Yield vs residence time at 350 $°C$ for ZS100. Lines represent model fits.

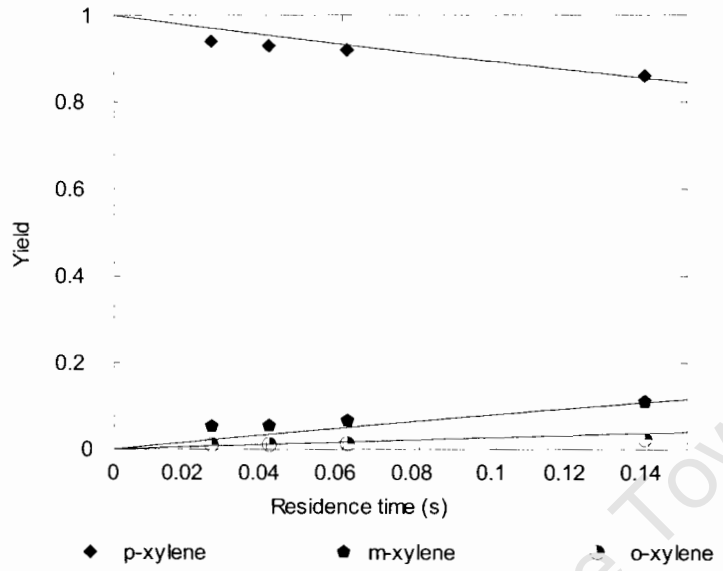

Figure D.6: Yield vs residence time at 250 $°C$ for ZS125. Lines represent model fits.

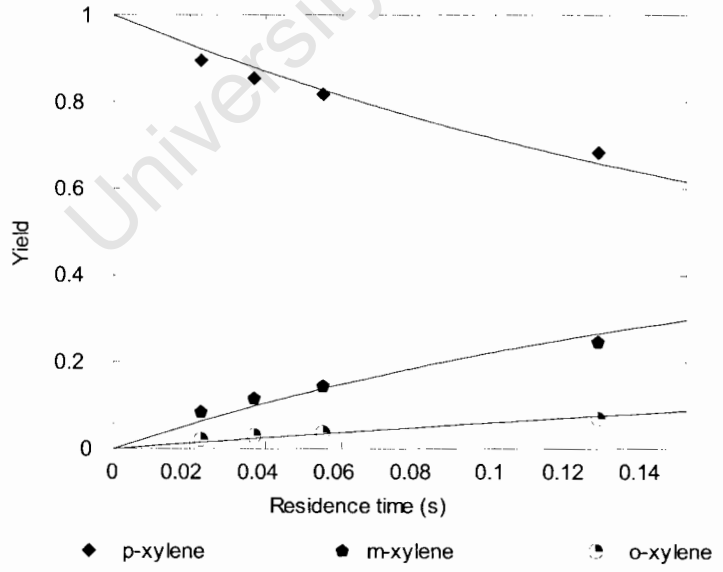

Figure D.7: Yield vs residence time at 300 $°C$ for ZS125. Lines represent model fits.

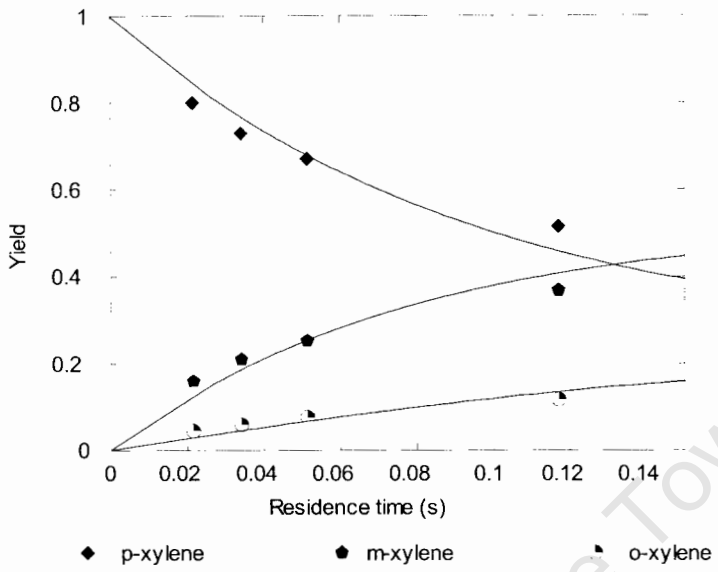

Figure D.8: Yield vs residence time at 350 $°C$ for ZS125. Lines represent model fits.

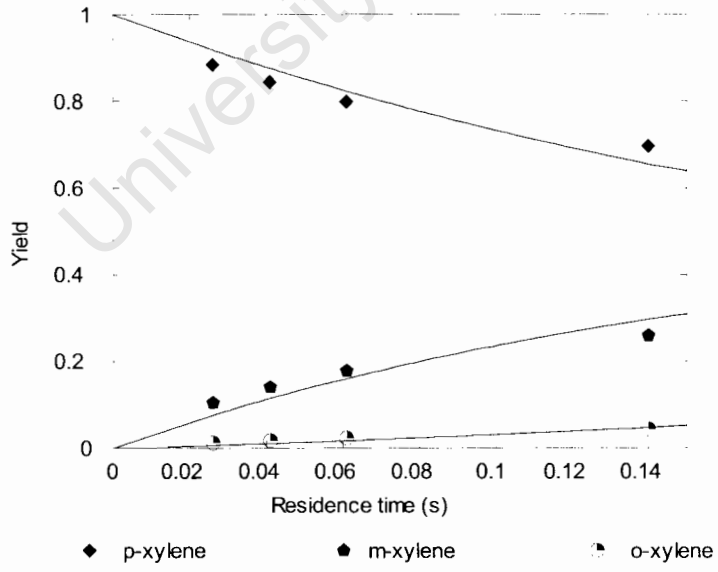

Figure D.9: Yield vs residence time at 250 $°C$ for ZS150. Lines represent model fits.

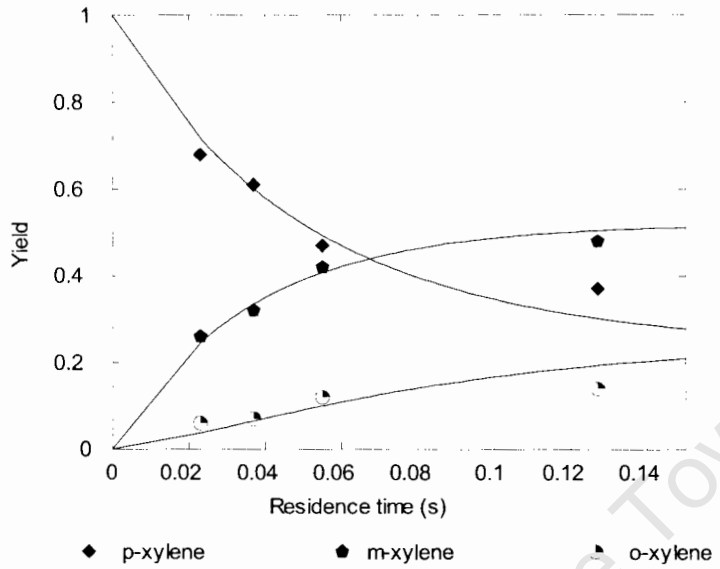

Figure D.10: Yield vs residence time at 300 $°C$ for ZS150. Lines represent model fits.

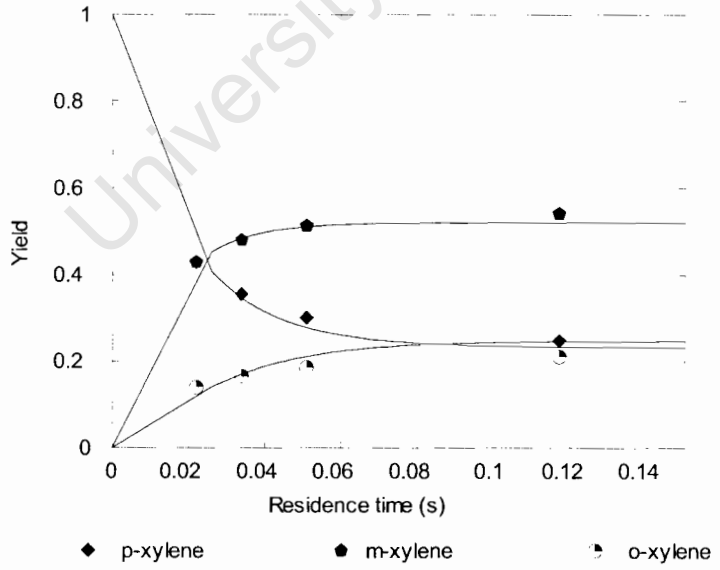

Figure D.11: Yield vs residence time at 350 $°C$ for ZS150. Lines represent model fits.

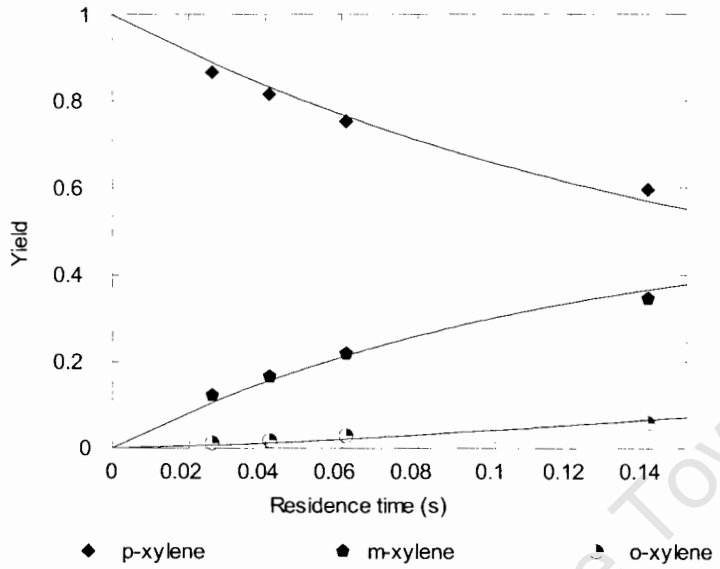

Figure D.12: Yield vs residence time at 250 $°C$ for ZS175. Lines represent model fits.

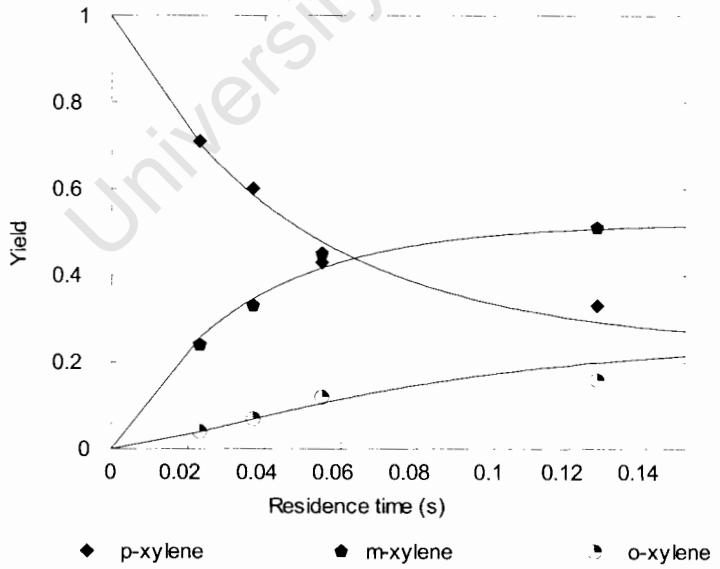

Figure D.13: Yield vs residence time at 300 $°C$ for ZS175. Lines represent model fits.

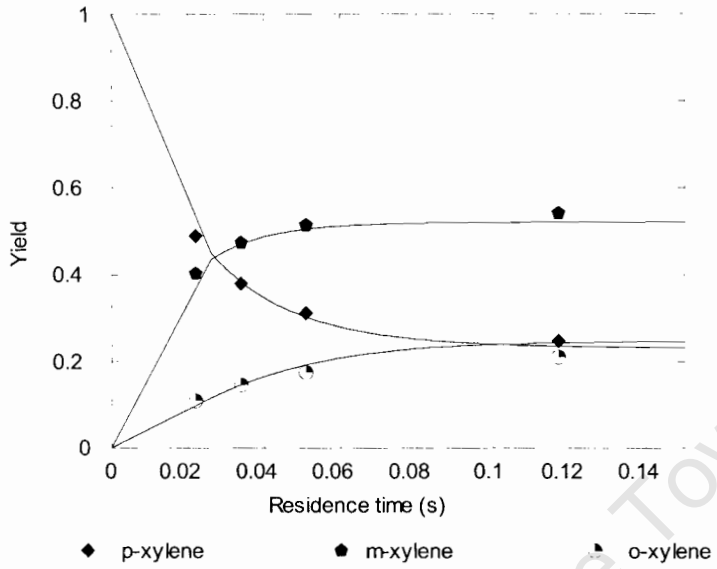

Figure D.14: Yield vs residence time at 350 $°C$ for ZS175. Lines represent model fits.

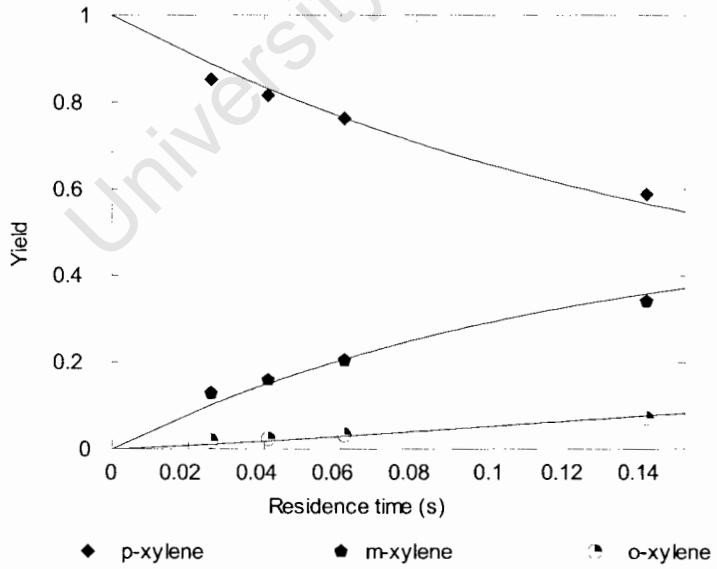

Figure D.15: Yield vs residence time at 250 $°C$ for ZS190. Lines represent model fits.

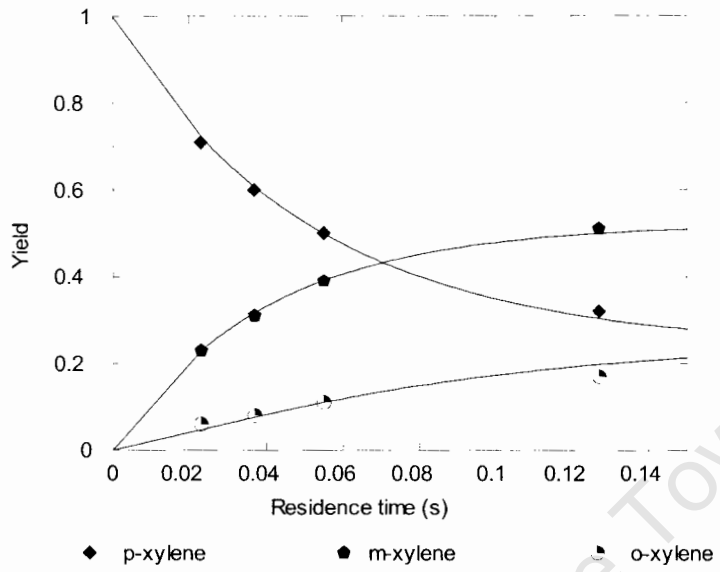

Figure D.16: Yield vs residence time at 300 $°C$ for ZS190. Lines represent model fits.

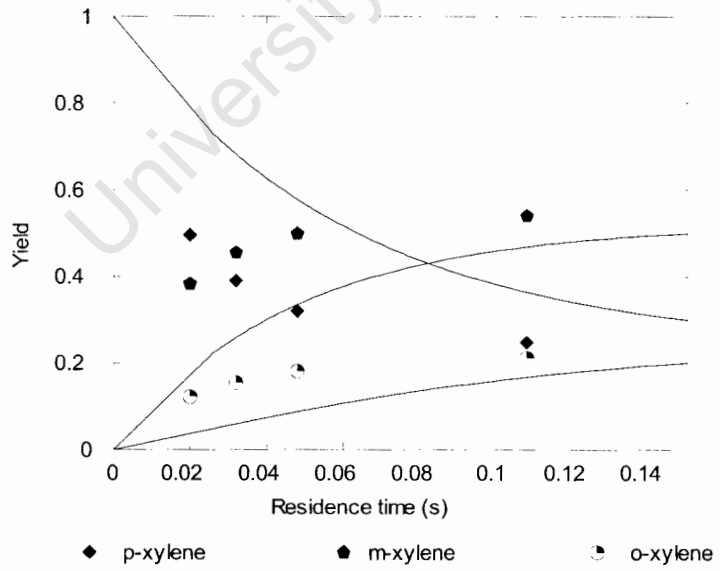

Figure D.17: Yield vs residence time at 350 $°C$ for ZS190. Lines represent model fits.

Appendix E

Film diffusion

Gas film diffusion may be the rate controlling step in the reaction mechanism. Film diffusion is not the rate limiting step if the difference between the surface and bulk concentrations are shown to be negligible. Conventionally this is done using the Sherwood mass transfer correlation:

$$sh = 2 + 0.99(\mathrm{Re}\,Sc)^{1/3} \tag{E.1}$$

In order to calculate the Schmidt number the diffusivity needs to be calculated. This is done using equation E2 developed by Fuller et al. (1996).

$$D_{AB} = \frac{100^{-3} T^{1.75} \left(\frac{1}{M_A} + \frac{1}{M_B} \right)^{0.5}}{P[\Sigma v_A{}^{1/3} + \Sigma v_B{}^{1/3}]^{0.5}} \tag{E.2}$$

The mass transfer coefficient k_f can now be calculated using the Sherwood number:

$$sh = \frac{d_p k}{D_{AB}} \tag{E.3}$$

Common reaction kinetics for mass transfer reactions yield the following equation:

$$V_{crystal} R_{px,\max} = k_f (C_{px,b} - C_{px,s}) A \tag{E.4}$$

where V is the volume of crystal

A is the surface area of catalyst

If it is assumed that it is a first order irreversible reaction i.e. low conversion and high flow rate may be written as

$$V_{crystal} k C_{px,s} = k_f \left(C_{px,b} - C_{px,s}\right) A \tag{E.5}$$

Rearranging of the equations gives the following:

$$C_{px,s} = \frac{k_f \left(C_{px,b} A\right)}{V_k + k_f A} = \frac{C_{px,b}}{1 + \frac{kV}{k_f A}} \tag{E.6}$$

Substitution of the approximate Sherwood number of 2, V and A into this equation simplifying yields:

$$C_{px} = \frac{\left(C_{px,b}\right)}{1 + \frac{1/3k}{\left(\frac{D}{R^2}\right)}} = \frac{C_{px,b}}{1 + C_o} \tag{E.7}$$

Since the radius of sand is approximatedly 200 μm and at high temperatures the diffusivity is approximately 1 cm^2/s the value of Co is insignificant. Thus the equation can be reduced to $C_{px,s} = C_{px,b}$. Thus film diffusion has been shown not to exist.

Appendix F

Plug flow conditions

In order to ensure plug flow conditions within the reactor as to avoid by-passing the following criteria was followed:

$$\frac{ID_{reactor}}{d_p} > 15 \tag{F.1}$$

and for axial dispersion:

$$\frac{L}{d_p} > \frac{20n}{Pe_p} \ln \frac{1}{1-X} \tag{F.2}$$

where $D_{reactor}$ is the diameter of the reactor

d_p is the diameter of the particle

L is the length of the bed

X is the conversion

To illustate plug flow term on the left should always be above the term on the right. These concepts are applied in Appendix 1.

dp was calculated from Scherrer formula and used in Appendix J:

$$d_p = \frac{k\lambda}{\beta \cos\theta} \tag{F.3}$$

where k is a constant

λ is the wavelenth

θ is the scanning angle

β is the width at peak half height

Appendix G

Raw data from experiments

Table G.1: Conversion and yield calculations

Selectivity- composition

Temperature	**Flow rate**	**Residence Time**	**Sample**									
			ZS50					**ZS100**				
$\circ C$	g/hr	ms	*para*	X	*meta*	*ortho*	*m/o*	*para*	X	*meta*	*ortho*	*m/o*
250	5	139.59						91.0	9.0	8.0	1.0	8.2
	10	61.14						95.1	4.9	4.5	0.4	10.7
	15	40.68						95.4	4.6	4.3	0.4	12.0
	25	25.62						97.2	2.8	2.6	0.2	10.5
300	5	127.42	96.3	3.7	3.2	0.5	7.0	71.3	28.7	23.5	5.2	4.5
	10	55.81	96.5	3.5	3.0	0.5	6.4	84.1	15.9	13.2	2.7	4.9
	15	37.13	98.6	1.4	1.4	0.0		88.7	11.3	9.5	1.8	5.2
	25	23.38	99.5	0.5	0.5	0.0		92.8	7.2	6.1	1.1	5.7
350	5	117.19	90.1	9.9	8.1	1.8	4.4	45.2	54.8	41.5	13.3	3.1
	10	51.33	93.0	7.0	5.7	1.3	4.3	64.4	35.6	27.7	7.9	3.5
	15	34.15	96.5	3.5	3.0	0.6	5.0	73.3	26.7	21.0	5.7	3.7
	25	21.51	97.6	2.4	2.0	0.4	4.4	82.4	17.6	14.1	3.5	4.0
400	5	108.49	79.4	20.6	15.9	4.7	3.4					
	10	47.52	89.2	10.8	8.4	2.3	3.6					
	15	31.61	92.5	7.5	5.9	1.6	3.7					
	25	19.91	95.4	4.6	3.7	0.9	4.0					

Sample																			
ZS125					**ZS150**					**ZS175**					**ZS190**				
para	X	*meta*	*ortho*	*m/o*	*para*	X	*meta*	*ortho*	*m/o*	*para*	X	*meta*	*ortho*	*m/o*	*para*	X	*meta*	*ortho*	*m/o*
86.3	13.7	11.3	2.4	4.7	69.7	30.3	25.9	4.4	5.9	59.6	40.4	34.6	5.9	5.9	58.8	41.2	34.0	7.1	4.8
92.0	8.0	6.6	1.3	4.9	79.9	20.1	17.8	2.3	7.8	75.3	24.7	21.9	2.9	7.7	76.3	23.7	20.4	3.3	6.1
93.5	6.5	5.4	1.1	4.9	84.4	15.6	14.0	1.7	8.4	81.6	18.4	16.6	1.8	9.1	81.6	18.4	15.9	2.4	6.6
93.7	6.3	5.3	1.0	5.5	88.4	11.6	10.4	1.2	9.0	86.6	13.4	12.2	1.2	10.3	85.2	14.8	12.8	1.9	6.6
68.4	31.6	24.6	7.0	3.5	37.5	62.5	48.2	14.3	3.4	33.3	66.7	51.1	15.7	3.3	32.1	67.9	50.9	17.1	3.0
81.8	18.2	14.4	3.8	3.8	46.6	53.4	41.8	11.5	3.6	43.2	56.8	44.8	12.0	3.7	50.1	49.9	38.9	11.0	3.5
85.4	14.6	11.5	3.0	3.8	60.5	39.5	32.0	7.5	4.3	60.2	39.8	33.1	6.7	5.0	60.4	39.6	31.4	8.2	3.8
89.5	10.5	8.4	2.1	3.9	67.9	32.1	26.2	5.8	4.5	71.3	28.7	24.5	4.2	5.8	71.4	28.6	23.1	5.5	4.2
51.5	48.5	36.8	11.7	3.1	24.8	75.2	54.1	21.1	2.6	24.8	75.2	54.1	21.1	2.6	24.8	75.2	54.0	21.2	2.5
67.1	32.9	25.3	7.6	3.3	30.1	69.9	51.3	18.6	2.8	31.1	68.9	51.4	17.5	2.9	32.0	68.0	49.9	18.1	2.8
73.5	26.5	20.6	5.9	3.5	35.5	64.5	48.0	16.5	2.9	37.9	62.1	47.4	14.6	3.2	39.0	61.0	45.5	15.5	2.9
79.6	20.4	15.9	4.5	3.5	43.0	57.0	43.0	14.0	3.1	48.9	51.1	40.3	10.9	3.7	49.6	50.4	38.2	12.2	3.1
35.9	64.1	47.4	16.7	2.8															
51.4	48.6	36.8	11.8	3.1															
59.7	40.3	30.8	9.5	3.3															
68.1	31.9	24.5	7.4	3.3															

Appendix H

Error analysis

Table H.1: Error analysis on yield

Sample	Run 1				Run 2				Run 3			
	Para	*Meta*	*Ortho*	**Total**	*Para*	*Meta*	*Ortho*	**Total**	*Para*	*Meta*	*Ortho*	**Total**
ZS50	257960	7251	0	265870	259210	6868	656	267350	257320	8217	873	267460
ZS100	211510	20375	5167	238090	214750	20091	5145	240660	225680	19105	4655	249440
ZS125	213880	23232	2667	240790	213690	25177	2797	242640	222280	26989	3401	253250
ZS150	218680	28479	2620	250270	214910	30275	2953	250870	208640	34684	3845	248030
ZS175	209850	31546	4784	246180	215310	30242	4467	250019	224710	33868	5169	264500

Table H.2: Average, standard deviation

Sample	*Para*	**Dev**	**% error**	*Meta*	**Dev**	**% error**	*Ortho*	**Dev**	**% error**	**Total**	**Dev**	**% error**
ZS50	258163	961.27	0.4	7445	695	9.3	510	455	89.2	266893	888	0.3
ZS100	217313	7424.6	3.4	19857	667	3.4	4989	289	5.8	242730	5951	2.5
ZS125	216617	4905.5	2.3	25133	1879	7.5	2955	392	13.3	245560	6724	2.7
ZS175	214077	5071.6	2.4	31146	3193	10.3	3139	633	20.2	249723	1497	0.6
ZS190	216623	7516.6	3.5	31885	1837	5.8	4807	352	7.3	253566	9661	3.8

Error in mass calculation	2.0	%
Error in flowrate calculation	2.7	%
Error in temperature reading	0.2	%
Error in pressure reading	0.7	%
Total error in Residence Time Calculation	5.6	%

Table H.3: Error on bubble meter

volume in bubble meter	**cm3**	15	15	15	15
time	**s**	9.34	4.06	2.72	1.72
	s	9.28	4.00	2.78	1.68
	s	9.28	4.16	2.63	1.72
Mean		9.3	4.1	2.7	1.7
Standard Error		0.0	0.0	0.0	0.0
Median		9.3	4.1	2.7	1.7
Standard Deviation		0.0	0.1	0.1	0.0
% Error		0.4	2.0	2.8	1.4
Sample Variance		0.0	0.0	0.0	0.0
Skewness		1.7	0.7	-0.6	-1.7
Range		0.06	0.16	0.15	0.04
Minimum		9.28	4	2.63	1.68
Maximum		9.34	4.16	2.78	1.72
Sum		27.9	12.22	8.13	5.12
Count		3	3	3	3

Appendix I

Temperature and Pressure corrections

Table I.1: Temperature and pressure corrections

		Reactor				Reactor				Reactor		
		5	10	15	25	5	10	15	25	5	10	15
time	s	9.34	4.06	2.72	1.72	9.34	4.06	2.72	1.72	9.34	4.06	2.72
	s	9.28	4.00	2.78	1.68	9.28	4.00	2.78	1.68	9.28	4.00	2.78
	s	9.28	4.16	2.63	1.72	9.28	4.16	2.63	1.72	9.28	4.16	2.63
distance	cm3	15	15	15	15	15	15	15	15	15	15	15
flow rate	cm3/sec	1.61	3.68	5.54	8.79	1.61	3.68	5.54	8.79	1.61	3.68	5.54
Temperature	oC	250.00	250.00	250.00	250.00	300.00	300.00	300.00	300.00	350.00	350.00	350.00
Temperature and pressure corrections	cm3/sec	2.05	4.67	7.02	11.15	2.24	5.12	7.70	12.22	2.44	5.57	8.37
Volume of cat	cm3	0.29	0.29	0.29	0.29	0.29	0.29	0.29	0.29	0.29	0.29	0.29
Residence time	s	139.59	61.14	40.68	25.62	127.42	55.81	37.13	23.38	117.19	51.33	34.15

	Reactor			
25	5	10	15	25
1.72	9.34	4.06	2.72	1.72
1.68	9.28	4.00	2.78	1.68
1.72	9.28	4.16	2.63	1.72
15	15	15	15	15
8.79	1.61	3.68	5.54	8.79
350.00	400.00	400.00	400.00	400.00
13.29	2.63	6.01	9.04	14.35
0.29	0.29	0.29	0.29	0.29
21.51	108.49	47.52	31.61	19.91

Appendix J

Plug flow

Table J.1: Plug flow conditions

Check for plug flow conditions								
L	0.04	m		k	0.9			
Pep	0.5			lumda	1.542	amstrongs		
				n	1			
				radians				
Beta	0.43	0.01	Beta	0.23	0.00	Beta	0.13	0.01
theta	15.03	0.26	theta	14.99	0.26	theta	14.52	0.27
d		193.72	d		365.85	d		172.00
ZS50			**ZS100**			**ZS125**		
	term 1	term 2		term 1	term 2		term 1	term 2
X			X			X		
0.2	109.33472	8.925742	0.2	133.5809196	8.9257421	0.2	206.4626302	8.925742
0.3	109.33472	14.267	0.3	133.5809196	14.266998	0.3	206.4626302	14.267
0.4	109.33472	20.43302	0.4	133.5809196	20.433025	0.4	206.4626302	20.43302
0.5	109.33472	27.72589	0.5	133.5809196	27.725887	0.5	206.4626302	27.72589
0.6	109.33472	36.65163	0.6	133.5809196	36.651629	0.6	206.4626302	36.65163
0.7	109.33472	48.15891	0.7	133.5809196	48.158912	0.7	206.4626302	48.15891
0.8	109.33472	64.37752	0.8	133.5809196	64.377516	0.8	206.4626302	64.37752

Beta	0.28	0.00	Beta	0.45	0.007854	Beta	0.425	0.007418
theta	15.07	0.26	theta	15.0375	0.262454	theta	15.05	0.262672
d		299.44	d		182.9656	d		193.7397

ZS150			**ZS175**			ZS190		
	term 1	term 2		term 1	term 2		term 1	term 2
X			X			X		
0.2	206.4868	8.925742	0.2	218.6203	8.925742	0.2	232.2557	8.925742
0.3	206.4868	14.267	0.3	218.6203	14.267	0.3	232.2557	14.267
0.4	206.4868	20.43302	0.4	218.6203	20.43302	0.4	232.2557	20.43302
0.5	206.4868	27.72589	0.5	218.6203	27.72589	0.5	232.2557	27.72589
0.6	206.4868	36.65163	0.6	218.6203	36.65163	0.6	232.2557	36.65163
0.7	206.4868	48.15891	0.7	218.6203	48.15891	0.7	232.2557	48.15891
0.8	206.4868	64.37752	0.8	218.6203	64.37752	0.8	232.2557	64.37752

Appendix K

Kinetic data from FORTRAN models

Table K.1: Kinetic constants

	ZS50			ZS100			ZS125			ZS150			ZS175		
Temperature $[\circ C]$	**k1**	**k2**	**D/R2**	**k1**	**k2**	**D/R2**	**k1**	**k2**	**D/R2**	**k1**	**k2**	**D/R2**	**k1**	**k2**	**D/R2**
250				0.82	0.41	1412.00	1.45	0.72	2708.00	3.49	1.75	9438.00	4.80	2.40	24820.00
300	1.74	0.87	1250	2.96	1.48	4017.00	4.18	2.09	574.00	16.55	8.28	35680.00	17.51	8.76	38940.00
350	2.749	1.3745	840	8.61	4.30	9338.00	9.42	4.71	6881.00	49.08	24.54	74130.00	40.92	20.46	98990.00
400	14.23	7.115	1460				19.80	9.90	16330.00						

ZS190		
k1	**k2**	**D/R2**
5.00	2.50	9677.00
16.77	8.39	17940.00
14.57	7.29	13940.00